Received: 21 March 2022 | Revised: 23 June 2022 | Accepted: 24 June 2022

DOI: 10.1002/nme.7080

RESEARCH ARTICLE

WILEY

# An isogeometric finite element formulation for boundary and shell viscoelasticity based on a multiplicative surface deformation split

**Karsten Paul**[1] | **Roger A. Sauer**[1,2,3]

[1]Aachen Institute for Advanced Study in Computational Engineering Science (AICES), RWTH Aachen University, Aachen, Germany

[2]Faculty of Civil and Environmental Engineering, Gdańsk University of Technology, Gdańsk,

[3]Department of Mechanical Engineering, Indian Institute of Technology Guwahati, Guwahati, Assam,

**Correspondence**
Roger A. Sauer, Aachen Institute for Advanced Study in Computational Engineering Science (AICES), RWTH Aachen University, Templergraben 55, 52062 Aachen, Germany.
Email: sauer@aices.rwth-aachen.de
roger.sauer@pg.edu.pl

**Funding information**
Deutsche Forschungsgemeinschaft, Grant/Award Number: 333849990/GRK2379; RWTH Aachen University, Grant/Award Number: rwth0917

**Abstract**

This work presents a numerical formulation to model isotropic viscoelastic material behavior for membranes and thin shells. The surface and the shell theory are formulated within a curvilinear coordinate system, which allows the representation of general surfaces and deformations. The kinematics follow from Kirchhoff–Love theory and the discretization makes use of isogeometric shape functions. A multiplicative split of the surface deformation gradient is employed, such that an intermediate surface configuration is introduced. The surface metric and curvature of this intermediate configuration follow from the solution of nonlinear evolution laws—ordinary differential equations—that stem from a generalized viscoelastic solid model. The evolution laws are integrated numerically with the implicit Euler scheme and linearized within the Newton–Raphson scheme of the nonlinear finite element framework. The implementation of membrane and bending viscosity is verified with the help of analytical solutions and shows ideal convergence behavior. The chosen numerical examples capture large deformations and typical viscoelasticity behavior, such as creep, relaxation, and strain rate dependence. It is also shown that the proposed formulation can be straightforwardly applied to model boundary viscoelasticity of 3D bodies.

**KEYWORDS**

isogeometric analysis, Kirchhoff–Love shells, multiplicative split, nonlinear finite element methods, surface elasticity, viscoelasticity

## 1 | INTRODUCTION

Thin-walled structures are common to many engineering branches, as they have low weight combined with high strength. A suitable approach to model these structures is Kirchhoff–Love theory, especially for very slender structures. Many materials, such as polymers, bitumens, biological materials, and several metals or plastics at elevated temperatures, exhibit viscoelastic behavior, that is, they show both elastic and viscous material properties. Elastic materials return to their original shape instantaneously once the applied loads are removed, whereas viscoelastic materials return to their original shape gradually. For large deformations, the elastic and viscous deformations are in general modeled by a multiplicative split of the deformation gradient, which leads to an additive split of certain strains.

This is an open access article under the terms of the Creative Commons Attribution-NonCommercial-NoDerivs License, which permits use and distribution in any medium, provided the original work is properly cited, the use is non-commercial and no modifications or adaptations are made.
© 2022 The Authors. *International Journal for Numerical Methods in Engineering* published by John Wiley & Sons Ltd.

Kirchhoff–Love theory considers thin shells, such that out-of-plane shear strains can be neglected. Therefore, the cross-section always remains orthogonal to the shell's mid-plane during deformation. The governing equation of Kirchhoff–Love shells contains higher-order derivatives, as it describes bending in terms of deformation and not in terms of rotation. The weak form thus requires $C^1$-continuity, which poses a requirement on the numerical discretization. Isogeometric analysis (IGA), introduced by Hughes et al.,[1] offers the possibility of discretizations with higher continuity by making use of splines for the description of the geometry and the solution, as is discussed in detail in Cottrell et al..[2] IGA has interesting mathematical properties[3] and can be integrated into standard finite element codes by performing the numerical integration of smooth basis functions on Bézier elements[4] or Lagrange elements.[5] Nguyen et al.[6] provide an overview on isogeometric analysis and discuss implementation aspects. Isogeometric Kirchhoff–Love shells have been intensively studied in the literature, starting with Kiendl et al.[7] Further works on isogeometric shells followed, such as blended shells,[8] hierarchical shells,[9] and large-strain Kirchhoff–Love shells.[10,11] For complex engineering problems, single patches are often not sufficient to represent shell geometries, such that multi-patch descriptions are required. The continuity of such discretizations is not preserved at patch interfaces and needs to be restored, see Paul et al.[12] for a recent review on patch enforcement techniques in isogeometric analysis. Isogeometric analysis has been used within several shell and membrane applications, such as laminated composite shells,[13,14] anisotropic shells,[15,16] shape optimization of shells,[17,18] liquid membranes,[19,20] biological tissues,[21,22] topology optimization of shells,[23,24] shell fracture,[25,26] lipid bilayers,[27,28] 2D materials,[29,30] shell elastoplasticity,[31,32] inverse analysis of shells,[33,34] Cahn–Hilliard phase separations on deforming surfaces,[35,36] adaptive surface refinement,[37,38] and fiber-reinforced shells.[39,40]

The rigorous treatment of linear viscoelasticity dates back to the works by Coleman and Noll[41] and Crochet and Naghdi.[42] Extensions to finite viscoelasticity have been provided by Koh and Eringen[43] and Sidoroff.[44] Finite element implementations of viscoelasticity followed.[45,46] Reese and Govindjee[47] present a theory for finite viscoelasticity based on a multiplicative split of the deformation gradient. Recent discussions on the origin, mathematics, and application of the multiplicative split are provided.[48-50] Shaw et al.[51] describe viscoelastic material models and discuss their numerical treatment including spatial adaptivity of the discretization. Miehe and Keck[52] present a model for filled rubbery polymers considering a superimposed finite elastic-viscoelastic-plastoelastic stress response with damage and they discuss its numerical implementation. Holzapfel and Gasser[53] provide a model for viscoelastic fiber-reinforced composites at finite strains and compare its finite element results with experimental data. Bonet[54] proposes a continuum formulation for viscoelastic materials and corresponding constitutive models considering finite deformations. Adolfsson and Enelund[55] make use of fractional derivatives to model large strain viscoelasticity. Fancello et al.[56] propose a general variational framework for finite viscoelastic models and compare several models with each other. Amin et al.[57] consider finite strain viscoelasticity of rubbers and investigate the effects of internal variables on viscous phenomena based on experiments and numerical models. Hossain et al.[58] focus on the modeling of polymer curing by considering viscoelasticity and shrinking at finite strains. Kästner et al.[59] propose an experimental procedure to classify the nonlinear, inelastic mechanical behavior of polymers and derive a corresponding material model. Marques and Creus[60] provide a summary on computational viscoelasticity. Shutov et al.[61] suggest an explicit solution for an implicit time stepping scheme used in finite strain viscoelasticity based on a multiplicative split of the deformation gradient. James and Waisman[62] demonstrate the importance of the viscoelastic response in structural design optimization.

The extension of viscoelasticity to shells has been addressed in fewer works. Evans and Hochmuth[63] propose a theory for viscoelastic membranes under large deformations and apply it to red cell discocytes. Neff[64] provide the first model for viscoelastic membranes and shells based on the classical multiplicative split of the deformation gradient. Such a split can also be formulated directly on the surface, as was shown in the recent work of Sauer et al.[65] Additive decompositions are used for erythrocyte membranes,[66] for shell formulations based on three-dimensional viscoelasticity,[67] for micropolar plates and shells,[68] and for fiber reinforced composite shells.[69] Liu et al.[70] consider surface viscoelasticity coupled with three-dimensional viscoelastic bulks to model cells and cell aggregates. Hernandez et al.[71] study viscoelastic behavior of Reissner–Mindlin shells. Dadgar-Rad and Firouzi[72] consider incompressible membranes and quasi-linear viscoelasticity. Following the work on surface elasticity,[73,74] Dortdivanlioglu and Javili[75] develop a theory for nonlinear surface viscoelasticity at finite strains by accounting for strain-dependent boundary stresses.

Recently, viscoelasticity has also been considered in isogeometric analysis. The work of Dortdivanlioglu and Javili[75] uses IGA, while Shafei et al.[76] make use of isogeometric analysis for the analysis of nonlinear vibration of viscoelastic plates. Further, Sun et al.[77] employ the isogeometric boundary element method to investigate viscoelastic materials.

The present work makes use of the new multiplicative surface deformation split of Sauer et al.[65] in order to model isotropic viscoelastic material behavior of thin shell structures. Here, the flexibility and consistency of this split are demonstrated and the corresponding computational formulation is described. The nonlinear isogeometric thin shell formulation

MOST WIEDZY Downloaded from mostwiedzy.pl

follows the work of Duong et al.,[11] see also Remark 1. The proposed formulation thus benefits from efficiency and accuracy gains provided by rotation-free isogeometric finite element formulations. A generalized viscoelastic solid is considered to model both membrane and bending viscosity, see also Remark 2. Several material models are outlined and a time integration scheme is presented to solve the evolution laws. For several special cases, analytical solutions are derived. It is further shown that the proposed formulation can be applied to model boundary viscoelasticity of 3D bodies without any further modifications. In summary, the formulation in the present work

- employs a multiplicative split of the surface deformation gradient for large strains,
- allows to flexibly describe in-plane and out-of-plane viscoelasticity,
- captures typical viscoelastic effects, such as creep, relaxation, and strain rate dependency,
- uses an isogeometric finite element implementation,
- uses numerical time integration to solve the evolution laws,
- is verified by several analytical solutions,
- exhibits ideal convergence rates, and
- can model boundary viscoelasticity of 3D bodies without any further modifications.

*Remark* 1. The employed shell formulation is based on a direct surface approach, which directly formulates the kinematical quantities, balance laws, and constitutive relations (in particular) for the surface, without resorting to 3D counterparts. The approach is consistent with 3D continuum mechanics, because the underlying kinematical assumptions, balance laws, and constitutive principles are the same. It is therefore possible to show their equivalency for certain constitutive models,[11] see also Remark 3. The direct surface approach enables a straightforward decomposition of the elastic energy density into membrane and bending contributions, which makes the constitutive modeling more flexible. Thus, the proposed approach admits any hyperelastic and viscous material that is consistent with the principles of material modeling such as the second law of thermodynamics.

*Remark* 2. The proposed formulation captures two separate cases in a unified manner: shell viscoelasticity (that includes membrane viscoelasticity as a special case) and boundary viscoelasticity of 3D bodies—a case which is sometimes referred to as *surface viscoelasticity* in the literature.[70,75] In the two cases, the term *surface* therefore either refers to the mid-plane of the shell or the boundary of the 3D solid. The separation into the two cases is only conceptual. Mathematically and computationally the two cases become identical in the proposed formulation. For brevity, terms like *surface viscoelasticity* are therefore simply used to subsume both cases.

The remainder of this article is structured as follows: Section 2 summarizes the surface description and kinematics considering the multiplicative split of the surface deformation gradient. Section 3 describes constitutive relations and the extension of hyperelasticity to account for membrane and bending viscosity. In Section 4, the computational formulation including the time integration scheme and the linearization is outlined. Section 5 presents several numerical examples that highlight viscoelastic material behavior and ideal convergence rates. Section 6 concludes this article with a summary and an outlook.

## 2 | THE MULTIPLICATIVE SURFACE DEFORMATION SPLIT

This section summarizes the continuum formulation of viscoelastic shells based on a curvilinear surface description and the multiplicative surface deformation split of Sauer et al.[65] A concise summary of the mathematical background of the thin shell theory can be found in Sauer.[78]

### 2.1 | Surface description

The surface description is based on the four different domains shown in Figure 1. The parameter domain is denoted by $\mathcal{P}$, while the reference, intermediate, and current surface are denoted by $\mathcal{S}_0$, $\hat{\mathcal{S}}$, and $\mathcal{S}$, respectively. The introduction of the intermediate configuration is required to account for deformations composed of two separate components, that is, elastic and inelastic components. The mapping $\boldsymbol{X}(\xi^\alpha)$ describes the reference surface and it associates the covariant basis

MOST WIEDZY Downloaded from mostwiedzy.pl

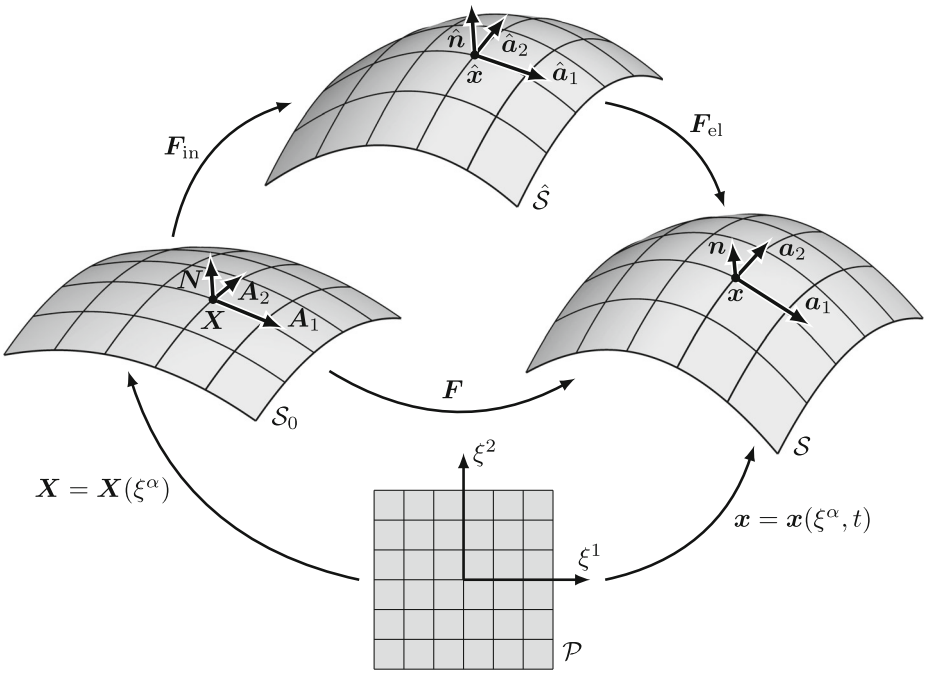


**FIGURE 1** Surface mappings with the multiplicative surface deformation split into inelastic and elastic components[65]

$\{\boldsymbol{A}_\alpha, \boldsymbol{N}\}$ to each surface point. Here, $\xi^\alpha$ ($\alpha = 1, 2$) denote the convective coordinates, $\boldsymbol{A}_\alpha$ are the tangent vectors and $\boldsymbol{N}$ is the surface normal. In analogy, the current surface $\mathcal{S}$ follows from $\boldsymbol{x}(\xi^\alpha, t)$ with covariant basis $\{\boldsymbol{a}_\alpha, \boldsymbol{n}\}$. Time is denoted $t$. In the intermediate configuration, the covariant basis is denoted $\{\hat{\boldsymbol{a}}_\alpha, \hat{\boldsymbol{n}}\}$. The deformation $\mathcal{S}_0 \rightarrow \hat{\mathcal{S}}$ is taken as the inelastic part ("in"), and $\hat{\mathcal{S}} \rightarrow \mathcal{S}$ as the elastic part ("el").

Given the mapping $\boldsymbol{x}(\xi^\alpha, t)$, the tangent vectors and surface normal follow as

$$\boldsymbol{a}_\alpha = \frac{\partial \boldsymbol{x}}{\partial \xi^\alpha}\,, \quad \text{and} \quad \boldsymbol{n} = \frac{\boldsymbol{a}_1 \times \boldsymbol{a}_2}{||\boldsymbol{a}_1 \times \boldsymbol{a}_2||}, \tag{1}$$

such that in-plane and out-of-plane surface objects can be characterized. The tangent vectors define the covariant surface metric with components

$$a_{\alpha\beta} = \boldsymbol{a}_\alpha \cdot \boldsymbol{a}_\beta, \tag{2}$$

which describe length and angle changes. In general, the basis $\{\boldsymbol{a}_\alpha, \boldsymbol{n}\}$ is not orthonormal. Orthonormality is restored by introducing a contravariant basis $\{\boldsymbol{a}^\alpha, \boldsymbol{n}\}$ through

$$\boldsymbol{a}^\alpha = a^{\alpha\beta}\, \boldsymbol{a}_\beta\,, \quad \text{with} \quad \left[a^{\alpha\beta}\right] = \left[a_{\alpha\beta}\right]^{-1}, \tag{3}$$

where $a^{\alpha\beta}$ refers to the contravariant surface metric. Note that index notation is used here, such that summation from 1 to 2 is implied on all terms with repeated Greek indices. Now, $\boldsymbol{a}^\alpha \cdot \boldsymbol{a}_\beta = \delta^\alpha_\beta$ with Kronecker delta $\delta^\alpha_\beta$.

The second parametric derivative $\boldsymbol{x}_{,\alpha\beta} = \boldsymbol{a}_{\alpha,\beta} = \partial \boldsymbol{a}_\alpha / \partial \xi^\beta$ is introduced to define the surface curvature

$$b_{\alpha\beta} = \boldsymbol{a}_{\alpha,\beta} \cdot \boldsymbol{n}\,. \tag{4}$$

It can be used to determine the mean and Gaussian curvature

$$H = 1/2\; a^{\alpha\beta}\; b_{\alpha\beta}\,, \quad \text{and} \quad \kappa = \det\left[b^\alpha{}_\beta\right]\,, \tag{5}$$

respectively, where $[b^\alpha{}_\beta] = [a^{\alpha\gamma} b_{\gamma\beta}]$. In contrast to the parametric derivative $\boldsymbol{a}_{\alpha,\beta}$, the covariant derivative of $\boldsymbol{a}_\alpha$ can be defined as $\boldsymbol{a}_{\alpha;\beta} := (\boldsymbol{n} \otimes \boldsymbol{n})\, \boldsymbol{a}_{\alpha,\beta}$.

MOST WIEDZY Downloaded from mostwiedzy.pl

The description of the reference surface $\mathcal{S}_0$ follows in analogy to the surface description of $\mathcal{S}$ presented above. The intermediate configuration $\hat{\mathcal{S}}$ is described by the unknown tangent vectors $\hat{\boldsymbol{a}}_\alpha$. Given these tangent vectors, the intermediate surface quantities can be characterized analogously to $\mathcal{S}_0$ and $\mathcal{S}$. For the reference surface, capital letters or the index "0" are used, whereas quantities on the intermediate configuration are denoted with a hat, "$\hat{\bullet}$." The intermediate surface metric $\hat{a}_{\alpha\beta}$ and curvature $\hat{b}_{\alpha\beta}$ are particularly important to describe viscoelasticity. These quantities follow in analogy to Equations (2) and (4).

## 2.2 | Surface kinematics

Figure 1 shows that the mappings between the different surface configurations are characterized by the surface deformation gradient $\boldsymbol{F}$, or its elastic or inelastic part, $\boldsymbol{F}_{\text{el}}$ and $\boldsymbol{F}_{\text{in}}$, respectively. They are given by

$$\boldsymbol{F} = \boldsymbol{a}_\alpha \otimes \boldsymbol{A}^\alpha \,, \quad \boldsymbol{F}_{\text{el}} = \boldsymbol{a}_\alpha \otimes \hat{\boldsymbol{a}}^\alpha \,, \quad \text{and} \quad \boldsymbol{F}_{\text{in}} = \hat{\boldsymbol{a}}_\alpha \otimes \boldsymbol{A}^\alpha, \tag{6}$$

such that the deformation gradient is multiplicatively split into its elastic and inelastic part, that is, $\boldsymbol{F} = \boldsymbol{F}_{\text{el}}\, \boldsymbol{F}_{\text{in}}$. Based on this split, the tangent vectors can be expressed as

$$\begin{aligned} &\boldsymbol{A}_\alpha = \boldsymbol{F}_{\text{in}}^{-1}\hat{\boldsymbol{a}}_\alpha = \boldsymbol{F}^{-1}\boldsymbol{a}_\alpha \,, \quad \hat{\boldsymbol{a}}_\alpha = \boldsymbol{F}_{\text{in}}\, \boldsymbol{A}_\alpha = \boldsymbol{F}_{\text{el}}^{-1}\boldsymbol{a}_\alpha \,, \quad \boldsymbol{a}_\alpha = \boldsymbol{F}_{\text{el}}\, \hat{\boldsymbol{a}}_\alpha = \boldsymbol{F}\boldsymbol{A}_\alpha \,, \\ &\boldsymbol{A}^\alpha = \boldsymbol{F}_{\text{in}}^{\text{T}}\, \hat{\boldsymbol{a}}^\alpha = \boldsymbol{F}^{\text{T}}\boldsymbol{a}^\alpha \,, \quad \hat{\boldsymbol{a}}^\alpha = \boldsymbol{F}_{\text{in}}^{-\text{T}}\boldsymbol{A}^\alpha = \boldsymbol{F}_{\text{el}}^{\text{T}}\, \boldsymbol{a}^\alpha \,, \quad \boldsymbol{a}^\alpha = \boldsymbol{F}_{\text{el}}^{-\text{T}}\hat{\boldsymbol{a}}^\alpha = \boldsymbol{F}^{-\text{T}}\boldsymbol{A}^\alpha \,. \end{aligned} \tag{7}$$

Based on the surface deformation gradient $\boldsymbol{F}$ in Equation (6), the surface Cauchy–Green tensors can be determined, that is,

$$\boldsymbol{C} = \boldsymbol{F}^{\text{T}}\boldsymbol{F} = a_{\alpha\beta}\, \boldsymbol{A}^\alpha \otimes \boldsymbol{A}^\beta \,, \quad \text{and} \quad \boldsymbol{B} = \boldsymbol{F}\boldsymbol{F}^{\text{T}} = A^{\alpha\beta}\, \boldsymbol{a}_\alpha \otimes \boldsymbol{a}_\beta. \tag{8}$$

They have the two invariants

$$I_1 = \boldsymbol{I} : \boldsymbol{C} = \boldsymbol{i} : \boldsymbol{B} = A^{\alpha\beta}\, a_{\alpha\beta} \,, \quad \text{and} \quad J = \frac{\sqrt{\det[a_{\alpha\beta}]}}{\sqrt{\det[A_{\alpha\beta}]}}. \tag{9}$$

The second invariant in Equation (9) characterizes the surface stretch between $\mathcal{S}_0$ and $\mathcal{S}$. Based on the surface identities $\boldsymbol{I} = \boldsymbol{A}_\alpha \otimes \boldsymbol{A}^\alpha$ on $\mathcal{S}_0$ and $\boldsymbol{i} = \boldsymbol{a}_\alpha \otimes \boldsymbol{a}^\alpha$ on $\mathcal{S}$ and Equation (8), the surface Green–Lagrange and surface Almansi strain tensors follow as

$$\boldsymbol{E} = \frac{1}{2}\, (\boldsymbol{C} - \boldsymbol{I}) = \varepsilon_{\alpha\beta}\, \boldsymbol{A}^\alpha \otimes \boldsymbol{A}^\beta \,, \quad \text{and} \quad \boldsymbol{e} = \frac{1}{2}\, \left(\boldsymbol{i} - \boldsymbol{B}^{-1}\right) = \varepsilon_{\alpha\beta}\, \boldsymbol{a}^\alpha \otimes \boldsymbol{a}^\beta, \tag{10}$$

respectively. In Equation (10), the strain components are given by

$$\varepsilon_{\alpha\beta} = \frac{1}{2}\, \left(a_{\alpha\beta} - A_{\alpha\beta}\right). \tag{11}$$

Now, the right surface Cauchy–Green tensor can be pushed forward to the intermediate configuration, and the inverse of the left surface Cauchy–Green tensor can be pulled back to the intermediate configuration, that is,

$$\begin{aligned} \boldsymbol{C}_{\text{el}} &:= \boldsymbol{F}_{\text{in}}^{-\text{T}}\, \boldsymbol{C}\, \boldsymbol{F}_{\text{in}}^{-1} = \boldsymbol{F}_{\text{el}}^{\text{T}}\, \boldsymbol{F}_{\text{el}} = a_{\alpha\beta}\, \hat{\boldsymbol{a}}^\alpha \otimes \hat{\boldsymbol{a}}^\beta \,, \quad \text{and} \\ \boldsymbol{B}_{\text{in}}^{-1} &:= \boldsymbol{F}_{\text{el}}^{\text{T}}\, \boldsymbol{B}^{-1}\, \boldsymbol{F}_{\text{el}} = \boldsymbol{F}_{\text{in}}^{-\text{T}}\boldsymbol{F}_{\text{in}}^{-1} = A_{\alpha\beta}\, \hat{\boldsymbol{a}}^\alpha \otimes \hat{\boldsymbol{a}}^\beta \,. \end{aligned} \tag{12}$$

In analogy to the push forward and pull back operations in Equation (12), the surface Green–Lagrange strain tensor $\boldsymbol{E}$ can be pushed forward, or equivalently, the surface Almansi strain tensor $\boldsymbol{e}$ can be pulled back to the intermediate configuration, that is,

$$\hat{\boldsymbol{e}} = \boldsymbol{F}_{\text{in}}^{-\text{T}}\, \boldsymbol{E}\, \boldsymbol{F}_{\text{in}}^{-1} = \boldsymbol{F}_{\text{el}}^{\text{T}}\, \boldsymbol{e}\, \boldsymbol{F}_{\text{el}}, \tag{13}$$

MOST WIEDZY Downloaded from mostwiedzy.pl

which results in

$$\hat{\boldsymbol{e}} = \frac{1}{2}\left(\boldsymbol{C}_{\text{el}} - \boldsymbol{B}_{\text{in}}^{-1}\right) = \varepsilon_{\alpha\beta}\ \hat{\boldsymbol{a}}^{\alpha} \otimes \hat{\boldsymbol{a}}^{\beta}, \tag{14}$$

due to Equations (7), (10), and (12). Equation (14) shows that the multiplicative split of the deformation tensor, see Equation (6), leads to the additive split of the strains

$$\hat{\boldsymbol{e}} = \hat{\boldsymbol{e}}_{\text{el}} + \hat{\boldsymbol{e}}_{\text{in}}, \tag{15}$$

where

$$\hat{\boldsymbol{e}}_{\text{el}} = \frac{1}{2}\left(\boldsymbol{C}_{\text{el}} - \hat{\boldsymbol{i}}\right) = \varepsilon_{\alpha\beta}^{\text{el}}\ \hat{\boldsymbol{a}}^{\alpha} \otimes \hat{\boldsymbol{a}}^{\beta}\ , \quad \text{and} \quad \hat{\boldsymbol{e}}_{\text{in}} = \frac{1}{2}\left(\hat{\boldsymbol{i}} - \boldsymbol{B}_{\text{in}}^{-1}\right) = \varepsilon_{\alpha\beta}^{\text{in}}\ \hat{\boldsymbol{a}}^{\alpha} \otimes \hat{\boldsymbol{a}}^{\beta}, \tag{16}$$

with the surface identity $\hat{\boldsymbol{i}} = \hat{\boldsymbol{a}}_{\alpha} \otimes \hat{\boldsymbol{a}}^{\alpha}$ on $\hat{\mathcal{S}}$. The strain components in Equation (11) are then also additively split, that is,

$$\varepsilon_{\alpha\beta} = \varepsilon_{\alpha\beta}^{\text{el}} + \varepsilon_{\alpha\beta}^{\text{in}}, \tag{17}$$

with

$$\varepsilon_{\alpha\beta}^{\text{el}} = \frac{1}{2}\ \left(a_{\alpha\beta} - \hat{a}_{\alpha\beta}\right)\ , \quad \text{and} \quad \varepsilon_{\alpha\beta}^{\text{in}} = \frac{1}{2}\left(\hat{a}_{\alpha\beta} - A_{\alpha\beta}\right). \tag{18}$$

Based on the multiplicative split of $\boldsymbol{F}$, the surface stretch in Equation (9.2) becomes

$$J = J_{\text{el}}\ J_{\text{in}}, \tag{19}$$

with

$$J_{\text{el}} = \frac{\sqrt{\det[a_{\alpha\beta}]}}{\sqrt{\det[\hat{a}_{\alpha\beta}]}}\ , \quad \text{and} \quad J_{\text{in}} = \frac{\sqrt{\det[\hat{a}_{\alpha\beta}]}}{\sqrt{\det[A_{\alpha\beta}]}}. \tag{20}$$

Further, the first invariant of $\boldsymbol{C}_{\text{el}}$ is given by

$$I_1^{\text{el}} = \hat{a}^{\alpha\beta} a_{\alpha\beta}. \tag{21}$$

In analogy to Equation (17), the additive curvature decomposition

$$\kappa_{\alpha\beta} = \kappa_{\alpha\beta}^{\text{el}} + \kappa_{\alpha\beta}^{\text{in}}, \tag{22}$$

with

$$\kappa_{\alpha\beta}^{\text{el}} = b_{\alpha\beta} - \hat{b}_{\alpha\beta}\ , \quad \text{and} \quad \kappa_{\alpha\beta}^{\text{in}} = \hat{b}_{\alpha\beta} - B_{\alpha\beta}, \tag{23}$$

is introduced. In analogy to Equation (5), the mean and Gaussian curvature of the intermediate surface are given by

$$\hat{H} = \frac{1}{2}\ \hat{a}^{\alpha\beta}\ \hat{b}_{\alpha\beta}\ , \quad \text{and} \quad \hat{\kappa} = \det\left[\hat{b}^{\alpha}{}_{\beta}\right]. \tag{24}$$

The influences of the split of the surface deformation gradient on the surface motion, stresses, moments, and balance laws are further discussed in Sauer et al.[65]

## 2.3 | Weak form

The quasi-static weak form for deforming shells is given by[79]

$$G_{\text{int}} - G_{\text{ext}} = 0\ , \quad \forall\ \delta\boldsymbol{x} \in \mathcal{U}, \tag{25}$$

MOST WIEDZY Downloaded from mostwiedzy.pl

with variation $\delta \boldsymbol{x}$ taken from some suitable space $\mathcal{U}$. The internal and external virtual work in Equation (25) are given by

$$\begin{aligned} G_{\text{int}} &:= \int_{S_0} \frac{1}{2} \delta a_{\alpha\beta}\, \tau^{\alpha\beta}\, \mathrm{d}A + \int_{S_0} \delta b_{\alpha\beta}\, M_0^{\alpha\beta}\, \mathrm{d}A\,, \quad \text{and} \\ G_{\text{ext}} &:= \int_S \delta \boldsymbol{x} \cdot \boldsymbol{f}\, \mathrm{d}A + \int_{\partial S} \delta \boldsymbol{x} \cdot \boldsymbol{T}\, \mathrm{d}s + \int_{\partial S} \delta \boldsymbol{n} \cdot \boldsymbol{M}\, \mathrm{d}s\,, \end{aligned} \tag{26}$$

where $\delta a_{\alpha\beta}$ and $\delta b_{\alpha\beta}$ refer to the variation of the surface metric and curvature, respectively. The external forces $\boldsymbol{f}$, $\boldsymbol{T}$, and $\boldsymbol{M}$ describe prescribed body forces, boundary tractions and boundary moments, respectively. The stress components $\tau^{\alpha\beta}$ and moment components $M_0^{\alpha\beta}$ in Equation (26.1) follow from constitution, which is discussed in the subsequent section.

## 3 | SURFACE CONSTITUTION

This section is concerned with the constitutive relations for viscoelastic shells. Section 3.1 focuses on elastic materials, which is then extended to viscoelastic materials in Section 3.2.

### 3.1 | Surface elasticity

For hyperelastic shells, it is advantageous to consider a decomposition of the elastic energy density into in-plane and out-of-plane contributions, that is,

$$\Psi_{\text{el}}(a_{\alpha\beta}, b_{\alpha\beta}) = \Psi_{\text{mem}}(a_{\alpha\beta}) + \Psi_{\text{bend}}(a_{\alpha\beta}, b_{\alpha\beta}), \tag{27}$$

where $\Psi_{\text{mem}}$ refers to the elastic energy density associated with in-plane membrane deformations, while $\Psi_{\text{bend}}$ refers to the elastic energy density associated with out-of-plane bending. Given the elastic energy density, the membrane stress and moment components can be computed via

$$\sigma^{\alpha\beta} = \frac{2}{J} \frac{\partial \Psi_{\text{el}}}{\partial a_{\alpha\beta}}\,, \quad \text{and} \quad M^{\alpha\beta} = \frac{1}{J} \frac{\partial \Psi_{\text{el}}}{\partial b_{\alpha\beta}}. \tag{28}$$

The corresponding Kirchhoff stress and moment components (w.r.t. the reference configuration) follow as $\tau^{\alpha\beta} = J\, \sigma^{\alpha\beta}$ and $M_0^{\alpha\beta} = J\, M^{\alpha\beta}$. The symmetric stress $\sigma^{\alpha\beta}$ appearing in Equations (26.1) and (28.1) is denoted *effective stress* by Simo and Fox.[80] It is generally not the same as the physical (Cauchy) stress

$$N^{\alpha\beta} = \sigma^{\alpha\beta} + b_\gamma^\beta\, M^{\gamma\alpha}, \tag{29}$$

that appears in the equilibrium equation. Only for pure membranes or flat shells $\sigma^{\alpha\beta} = N^{\alpha\beta}$. Given $N^{\alpha\beta}$, the surface tension and the deviatoric membrane stresses are given by

$$\gamma = \frac{1}{2}\, N^{\alpha\beta}\, a_{\alpha\beta}\,, \quad \text{and} \quad N_{\text{dev}}^{\alpha\beta} = N^{\alpha\beta} - \gamma\, a^{\alpha\beta}. \tag{30}$$

In Sections 3.1.1–3.1.7, several choices for $\Psi_{\text{mem}}$ and $\Psi_{\text{bend}}$ and their resulting stresses and moments are presented.

*Remark* 3. As pointed out in Remark 1, the employed shell formulation is based on a direct surface approach, for which the elastic energy density in Equation (27) is an energy per surface area. Instead of providing this energy function directly, it can also be extracted from classical three-dimensional constitutive models. In that case, the 3D constitutive model is projected onto the surface via thickness integration, as is briefly described subsequently.[11] The in-plane components of the three-dimensional second Piola-Kirchhoff stress tensor $\tilde{\boldsymbol{S}}$ are

$$\tilde{\tau}^{\alpha\beta} = \boldsymbol{G}^\alpha \cdot \tilde{\boldsymbol{S}}\, \boldsymbol{G}^\beta, \tag{31}$$

where $\boldsymbol{G}^\alpha$ denotes the tangent vector of the shell layer at position $\boldsymbol{X} + \xi_0\, \boldsymbol{N}$,[11] with thickness coordinate $\xi_0 \in [-T/2, T/2]$ and initial shell thickness $T$. The tensor $\tilde{\boldsymbol{S}}$ can then be taken from classical three-dimensional hyperelasticity and

MOST WIEDZY Downloaded from mostwiedzy.pl

viscoelasticity models. The resulting stress and moment components of the shell then follow from the thickness integration[11]

$$\tau^{\alpha\beta} \approx \int_{-\frac{T}{2}}^{\frac{T}{2}} \tilde{\tau}^{\alpha\beta}\, \mathrm{d}\xi_0\,, \quad \text{and} \quad M_0^{\alpha\beta} \approx -\int_{-\frac{T}{2}}^{\frac{T}{2}} \xi_0\, \tilde{\tau}^{\alpha\beta}\, \mathrm{d}\xi_0. \tag{32}$$

The numerical integration that is generally required here makes the projection approach less efficient than the direct surface approach.

### 3.1.1 | Koiter membrane model

Given the membrane energy density of the Koiter model[79,81]

$$\Psi_{\mathrm{mem}}(a_{\alpha\beta}) = \frac{1}{8}\left(a_{\alpha\beta} - A_{\alpha\beta}\right)\; c^{\alpha\beta\gamma\delta}\; \left(a_{\gamma\delta} - A_{\gamma\delta}\right), \tag{33}$$

with

$$c^{\alpha\beta\gamma\delta} = \Lambda\, A^{\alpha\beta}\, A^{\gamma\delta} + \mu\, (A^{\alpha\gamma} A^{\beta\delta} + A^{\alpha\delta} A^{\beta\gamma}), \tag{34}$$

the stresses follow from Equation (28.1) as

$$\sigma^{\alpha\beta}\left(a_{\gamma\delta}\right) = \frac{1}{2\,J}\, c^{\alpha\beta\gamma\delta}\, (a_{\gamma\delta} - A_{\gamma\delta}) = \frac{1}{J}\, \left[\frac{\Lambda}{2}\, (I_1 - 2)\; a^{\alpha\beta} + \mu\; \left(A^{\alpha\gamma}\, a_{\gamma\delta}\, A^{\beta\delta} - a^{\alpha\beta}\right)\right]. \tag{35}$$

### 3.1.2 | Neo-Hookean membrane model

Analogous to the classical three-dimensional Neo-Hookean material model, the Neo-Hookean membrane energy density is given by[79]

$$\Psi_{\mathrm{mem}}\left(a_{\alpha\beta}\right) = \frac{\Lambda}{4}\; \left(J^2 - 1 - 2\; \ln J\right) + \frac{\mu}{2}\, (I_1 - 2 - 2\; \ln J)\,. \tag{36}$$

Its resulting stresses are

$$\sigma^{\alpha\beta}\left(a_{\gamma\delta}\right) = \frac{1}{J}\, \left[\frac{\Lambda}{2}\; \left(J^2 - 1\right)\; a^{\alpha\beta} + \mu\; \left(A^{\alpha\beta} - a^{\alpha\beta}\right)\right]. \tag{37}$$

Note that in this work, $\Lambda$ may be taken as zero in Equation (37), as it allows for an analytical solution of the evolution laws, see also Section 3.2.

### 3.1.3 | Neo-Hookean membrane model with dilatational/deviatoric split

The membrane energy density in Equation (36) does not properly split the energy into pure dilatational and deviatoric components. A proper split is achieved by the following membrane energy density[27]

$$\Psi_{\mathrm{mem}}(a_{\alpha\beta}) = \frac{K}{4}\; \left(J^2 - 1 - 2\; \ln J\right) + \frac{\mu}{2}\; \left(\frac{I_1}{J} - 2\right), \tag{38}$$

which yields the stresses

$$\sigma^{\alpha\beta}\left(a_{\gamma\delta}\right) = \frac{1}{J}\; \left[\frac{K}{2}\, (J^2 - 1)\, a^{\alpha\beta} + \frac{\mu}{2\,J}\; \left(2\, A^{\alpha\beta} - I_1\, a^{\alpha\beta}\right)\right]. \tag{39}$$

MOST WIEDZY Downloaded from mostwiedzy.pl

### 3.1.4 | Incompressible Neo-Hookean membrane model

The classical 3D incompressible Neo-Hookean material model is described by the stress[82]

$$\tilde{\boldsymbol{\sigma}} = \tilde{\mu}\ \tilde{\boldsymbol{B}} + q\ \mathbf{1}. \tag{40}$$

Here, $\tilde{\mu}$ denotes the 3D shear modulus and $q$ is the Lagrange multiplier associated with the incompressibility constraint. For membranes and thin shells, $\tilde{\boldsymbol{B}} = \boldsymbol{B} + \lambda_3^2\ (\boldsymbol{n} \otimes \boldsymbol{n})$ and $\tilde{\boldsymbol{\sigma}} = \boldsymbol{\sigma}/\tilde{t} + \sigma_{33}\ (\boldsymbol{n} \otimes \boldsymbol{n})$, where $\lambda_3$ denotes the out-of-plane stretch and $\tilde{t}$ is the shell thickness.* Based on Equation (40), the membrane stresses follow as[83]

$$\sigma^{\alpha\beta}\left(a_{\gamma\delta}\right) = \frac{\mu}{J}\ \left(A^{\alpha\beta} - \frac{a^{\alpha\beta}}{J^2}\right). \tag{41}$$

### 3.1.5 | Membranes with constant surface tension

A constant surface tension $\gamma$, see Equation (30.1), can be imposed with the energy density[84]

$$\Psi_{\text{mem}}(a_{\alpha\beta}) = \gamma\ J, \tag{42}$$

which yields the stresses

$$\sigma^{\alpha\beta}\left(a_{\gamma\delta}\right) = \gamma\ a^{\alpha\beta}. \tag{43}$$

### 3.1.6 | Koiter bending model

Similar to Equation (33), the Koiter model for bending is defined via[79,81]

$$\Psi_{\text{bend}}(b_{\alpha\beta}) = \frac{1}{2}\left(b_{\alpha\beta} - B_{\alpha\beta}\right)\ f^{\alpha\beta\gamma\delta}\ \left(b_{\gamma\delta} - B_{\gamma\delta}\right), \tag{44}$$

with for instance $f^{\alpha\beta\gamma\delta} = c/2\ (A^{\alpha\gamma}A^{\beta\delta} + A^{\alpha\delta}A^{\beta\gamma})$, where $c$ is the bending modulus. The resulting moment components follow from Equation (28.2) as

$$M^{\alpha\beta}(b_{\gamma\delta}) = \frac{1}{J}\, f^{\alpha\beta\gamma\delta}\ \left(b_{\gamma\delta} - B_{\gamma\delta}\right). \tag{45}$$

### 3.1.7 | Helfrich bending model

The Helfrich bending energy density is given by[79,85]

$$\Psi_{\text{bend}}(a_{\alpha\beta}, b_{\alpha\beta}) = J\ \left(k\ (H - H_0)^2 + k^\star\ \kappa\right), \tag{46}$$

which leads to the stresses

$$\sigma^{\alpha\beta}(a_{\gamma\delta}, b_{\gamma\delta}) = \left(k\ (H - H_0)^2 - \kappa^\star\ \kappa\right)\ a^{\alpha\beta} - 2\ k\ (H - H_0)\ b^{\alpha\beta}, \tag{47}$$

and moment components

$$M^{\alpha\beta}(a_{\gamma\delta}, b_{\gamma\delta}) = \left(k\ (H - H_0) + 2\ k^\star\ H\right)\ a^{\alpha\beta} - k^\star\ b^{\alpha\beta}, \tag{48}$$

with material parameters $k$ and $k^\star$, and the so-called spontaneous curvature $H_0$, which can be used to impose an initial stress-free mean curvature. Note that in this work, $k^\star$ is taken as zero in Equations (46)–(48).

MOST WIEDZY Downloaded from mostwiedzy.pl

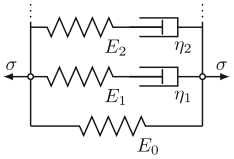


**FIGURE 2** Surface rheology: Generalized viscoelastic solid. Here, $E_\bullet$ denotes the Young's modulus of a spring element, and $\eta_\bullet$ refers to the damping coefficient of a dashpot element

## 3.2 | Surface viscoelasticity

In order to model viscoelastic material behavior, a generalized viscoelastic solid as shown by the rheological model in Figure 2 is considered. It is composed of one branch containing a spring element ("elastic branch"), and several Maxwell branches that contain a spring and dashpot element. For simplicity, here, only one Maxwell branch is considered, such that the total stresses are given by

$$\sigma^{\alpha\beta}\left(a^{\gamma\delta}, \hat{a}^{\gamma\delta}\right) = \sigma_0^{\alpha\beta}\left(a^{\gamma\delta}\right) + \sigma_1^{\alpha\beta}\left(\hat{a}^{\gamma\delta}\right), \tag{49}$$

where $\sigma_0^{\alpha\beta}$ are the stresses in the elastic branch, and $\sigma_1^{\alpha\beta}$ are the stresses in the Maxwell branch. Due to the multiplicative split of the surface deformation gradient and the resulting additive split of the strains, the strains in the spring and dashpot element of a Maxwell branch are not equal. But the stresses are equal, that is,

$$\sigma_{1(\mathrm{el})}^{\alpha\beta}\left(\hat{a}^{\gamma\delta}\right) = \sigma_{1(\mathrm{in})}^{\alpha\beta}\left(\hat{a}^{\gamma\delta}, \dot{\hat{a}}^{\gamma\delta}\right). \tag{50}$$

Equation (50) resembles three generally nonlinear ordinary differential equations (ODEs) for the components $\hat{a}^{\gamma\delta}$. The indices "(el)" and "(in)" refer to the spring and dashpot element of a Maxwell branch, respectively.[†] Once $\hat{a}^{\gamma\delta}$ is determined, the stresses $\sigma_1^{\alpha\beta}(\hat{a}^{\gamma\delta})$ in Equation (49) can be computed, and the total stresses $\sigma^{\alpha\beta}\left(a^{\gamma\delta}, \hat{a}^{\gamma\delta}\right)$ are then used in the weak form, see Equation (26.1).

A simple shear viscosity model for the inelastic stresses is given by[65]

$$\sigma_{1(\mathrm{in})}^{\alpha\beta}\left(\dot{\hat{a}}^{\gamma\delta}\right) = -\frac{1}{J_{\mathrm{el}}}\,\eta_{\mathrm{s}}\,\dot{\hat{a}}^{\alpha\beta}, \tag{51}$$

where $\eta_{\mathrm{s}} \geq 0$ denotes the in-plane shear viscosity. Note that the model in Equation (51) causes both shear and dilatation as the example in Section 5.1.1 shows. This is due to the fact that it leads to nonzero surface tension $\gamma$, see Equation (30.1). Another simple viscosity model is given by[65]

$$\sigma_{1(\mathrm{in})}^{\alpha\beta}\left(\dot{\hat{a}}^{\gamma\delta}\right) = \frac{1}{J_{\mathrm{el}}}\,\eta_{\mathrm{s}}\,\dot{J}_{\mathrm{in}}\,\hat{a}^{\alpha\beta}, \tag{52}$$

with $\eta_{\mathrm{s}} \geq 0$. In general, Equation (52) leads to nonzero shear stresses, such that the model is not purely dilatational.

In all cases, the dissipated energy can be computed via

$$\mathcal{D} = \int_0^t \int_S \sigma_1^{\alpha\beta}\,\dot{\varepsilon}_{\alpha\beta}^{\mathrm{in}}\,\mathrm{d}a\,\mathrm{d}t. \tag{53}$$

Given Equation (51) and Maxwell stresses $\sigma_{1(\mathrm{el})}^{\alpha\beta}$, Equation (50) can be rewritten in the form

$$\dot{\hat{a}}^{\alpha\beta} = -\frac{J_{\mathrm{el}}}{\eta_{\mathrm{s}}}\,\sigma_{1(\mathrm{el})}^{\alpha\beta}\left(\hat{a}^{\gamma\delta}\right), \tag{54}$$

with the initial condition $\hat{a}^{\alpha\beta}\big|_{t=0} = A^{\alpha\beta}$. In analogy to Equation (28.1), the Maxwell stresses $\hat{\sigma}_{1(\mathrm{el})}^{\alpha\beta}$ follow from an energy density $\hat{\Psi}_{\mathrm{mem}}(\hat{a}_{\alpha\beta}, a_{\alpha\beta})$, that is,

$$\hat{\sigma}_{1(\mathrm{el})}^{\alpha\beta} = \frac{\partial\hat{\Psi}_{\mathrm{mem}}}{\partial\varepsilon_{\alpha\beta}^{\mathrm{el}}} = \frac{\partial\hat{\Psi}_{\mathrm{mem}}}{\partial\epsilon_{\alpha\beta}}, \tag{55}$$

MOST WIEDZY Downloaded from mostwiedzy.pl

where the elastic energy density $\hat{\Psi}_{\text{mem}}(\hat{a}_{\alpha\beta}, a_{\alpha\beta})$ follows analogously to the membrane energy densities presented in Section 3.1, see also Sauer et al.[65] The stresses $\hat{\sigma}^{\alpha\beta}_{1(\text{el})}$ can then be referred to the current surface via $\sigma^{\alpha\beta}_{1(\text{el})} = 1/J_{\text{el}}\ \hat{\sigma}^{\alpha\beta}_{1(\text{el})}$.

*Remark* 4. To obtain the elastic energy density $\hat{\Psi}_{\text{el}}$ from one of the energy densities $\Psi_{\text{el}}$ presented in Section 3.1, the variables $A_{\alpha\beta}$ and $B_{\alpha\beta}$ need to be replaced by $\hat{a}_{\alpha\beta}$ and $\hat{b}_{\alpha\beta}$. Thus, $\hat{\Psi}_{\text{el}}$ will be dependent on $\hat{a}_{\alpha\beta}$, $\hat{b}_{\alpha\beta}$, $a_{\alpha\beta}$, and $b_{\alpha\beta}$. In contrast, $\Psi_{\text{el}}$ is expressed in terms of $A_{\alpha\beta}$, $B_{\alpha\beta}$, $a_{\alpha\beta}$, and $b_{\alpha\beta}$.

In general, time integration schemes are needed to solve the evolution laws in Equation (54), which are discussed in Section 4.4. In some special cases, however, the ODEs in Equation (54) can be solved analytically. For instance, using the Neo-Hookean material model from Equation (37) with $\Lambda = 0$ for the Maxwell branch, the ODEs simplify to

$$\dot{\hat{a}}^{\alpha\beta} = \frac{\mu_1}{\eta_{\text{s}}} \left( a^{\alpha\beta} - \hat{a}^{\alpha\beta} \right), \tag{56}$$

where the contravariant surface metric generally depends on time, that is, $a^{\alpha\beta} = a^{\alpha\beta}(t)$. Equation (56) resembles three independent, linear, first-order, inhomogeneous ODEs, which can be solved analytically for specific choices of $a^{\alpha\beta}(t)$, for example, see the numerical examples in Sections 5.2 and 5.4.

In analogy to Equation (49), the total moment components for the generalized viscoelastic solid with one Maxwell branch are[‡]

$$M^{\alpha\beta}\left(b_{\gamma\delta}, \hat{b}_{\gamma\delta}\right) = M^{\alpha\beta}_{(0)}\left(b_{\gamma\delta}\right) + M^{\alpha\beta}_{(1)}\left(\hat{b}_{\gamma\delta}\right) . \tag{57}$$

Similar to the stress equality condition for membrane viscosity in Equation (50), bending viscosity requires that the moments in the spring and dashpot element of the Maxwell branch, see Figure 2, are equal, that is,

$$M^{\alpha\beta}_{(1)(\text{el})}\left(\hat{b}_{\gamma\delta}\right) = M^{\alpha\beta}_{(1)(\text{in})}\left(\hat{b}_{\gamma\delta}, \dot{\hat{b}}_{\gamma\delta}\right) , \tag{58}$$

where "(1)" refers to the *first* Maxwell branch. In analogy to Equation (51), a simple model for the moment components in the dashpot element is[65]

$$M^{(1),(\text{in})}_{\alpha\beta}\left(\dot{\hat{b}}_{\gamma\delta}\right) = \frac{\eta_{\text{b}}}{J_{\text{el}}}\ \dot{\hat{b}}_{\alpha\beta}, \tag{59}$$

with $\eta_{\text{b}} \geq 0$. Combining Equations (58) and (59), the evolution laws can be written as

$$\dot{\hat{b}}_{\alpha\beta} = \frac{J_{\text{el}}}{\eta_{\text{b}}}\ M^{(1)(\text{el})}_{\alpha\beta}\left(\hat{b}_{\gamma\delta}\right), \tag{60}$$

with initial condition $\hat{b}_{\alpha\beta}\big|_{t=0} = B_{\alpha\beta}$. In analogy to Equation (28.2), the Maxwell moments $\hat{M}^{\alpha\beta}_{1(\text{el})}$ follow from a bending energy density $\hat{\Psi}_{\text{bend}}(\hat{a}_{\alpha\beta}, \hat{b}_{\alpha\beta}, a_{\alpha\beta}, b_{\alpha\beta})$, that is,

$$\hat{M}^{\alpha\beta}_{(1)(\text{el})} = \frac{\partial \hat{\Psi}_{\text{bend}}}{\partial \kappa^{\text{el}}_{\alpha\beta}} = \frac{\partial \hat{\Psi}_{\text{bend}}}{\partial \kappa_{\alpha\beta}}, \tag{61}$$

where a material model from Section 3.1 can be chosen for $\hat{\Psi}_{\text{bend}}(\hat{a}_{\alpha\beta}, \hat{b}_{\alpha\beta}, a_{\alpha\beta}, b_{\alpha\beta})$ (by replacing $A_{\alpha\beta}$ with $\hat{a}_{\alpha\beta}$ and $B_{\alpha\beta}$ with $\hat{b}_{\alpha\beta}$, see also Remark 4). Equation (61) can then be referred to the current surface via $M^{\alpha\beta}_{(1)(\text{el})} = 1/J_{\text{el}}\ \hat{M}^{\alpha\beta}_{(1)(\text{el})}$. Note that in case of the Koiter bending model from Equation (45), Equation (60) leads to the evolution laws

$$\dot{\hat{b}}_{\alpha\beta} = \frac{c_1}{\eta_{\text{b}}} \left( b_{\alpha\beta} - \hat{b}_{\alpha\beta} \right), \tag{62}$$

which resembles three independent linear, first-order, inhomogeneous ODEs, similar to Equation (56). For specific choices of $b_{\alpha\beta}(t)$, these ODEs are analytically solvable, for example, see the numerical examples in Sections 5.3 and 5.4.

MOST WIEDZY Downloaded from mostwiedzy.pl

If no analytical solution is possible, numerical time integration needs to be used to solve the evolution laws, which is discussed in Section 4.4.

## 4 | COMPUTATIONAL FORMULATION

This section briefly summarizes isogeometric surface discretizations in Section 4.1 and a corresponding computational formulation for modeling thin shells in Sections 4.2 and 4.3, following Duong et al.[11] Section 4.4 presents the numerical treatment for viscoelastic shells together with a time integration scheme for the evolution laws. The linearization within the finite element framework is discussed in Section 4.5 and a summary of the governing equations is provided in Section 4.6.

### 4.1 | Isogeometric surface discretization

The solution of the weak form of thin shells in Equations (25) and (26) requires $C^1$-continuous surface discretizations. Isogeometric analysis (IGA), proposed by Hughes et al.,[1] provides such surface discretizations, while offering many additional advantages. The basis functions of IGA are based on splines. Figure 3A visualizes these spline basis functions for cubic order ($p = 3$) and knot vector $\Xi = [0, 0, 0, 0, 0.25, 0.5, 0.75, 1, 1, 1, 1]$. Each basis function spans over $p + 1$ elements, which is different from standard finite element methods based on Lagrangian basis functions.

For two parametric directions, as required for the surface description presented in Section 2.1, the basis functions follow from the tensor product of the basis functions in each parametric dimension. In order to embed isogeometric analysis into a standard finite element code, the Bézier extraction operator of Borden et al.[4] can be used. For a given element $\Omega^e$, there are $n$ spline basis function that have support on $\Omega^e$, that is, that are non-vanishing on this element. The NURBS (Non-Uniform Rational B-Splines) basis functions $\{N_A\}_{A=1}^n$ on $\Omega^e$ at the parametric coordinate $(\xi, \eta)$ are given by

$$N_A(\xi, \eta) = \frac{w_A \, \hat{N}_A(\xi, \eta)}{\sum_{\bar{A}=1}^{n} w_{\bar{A}} \, \hat{N}_{\bar{A}}(\xi, \eta)}, \tag{63}$$

with weights $w_A$ and B-spline basis functions $\{\hat{N}_A\}_{A=1}^n$. This B-spline basis is mapped to a Bézier basis, which does not span over multiple elements. Cubic Bézier polynomials $B_{i,p}$ $(i = 0, \dots, p)$ are illustrated in Figure 3B. Considering the Bézier extraction operators $\mathbf{C}_\xi^e$ and $\mathbf{C}_\eta^e$ for element $\Omega^e$ in $\xi$- and $\eta$-direction, respectively, yields the B-spline basis functions

$$\hat{\mathbf{N}}^e(\xi, \eta) = \mathbf{C}_\xi^e \, \mathbf{B}(\xi) \otimes \mathbf{C}_\eta^e \, \mathbf{B}(\eta). \tag{64}$$

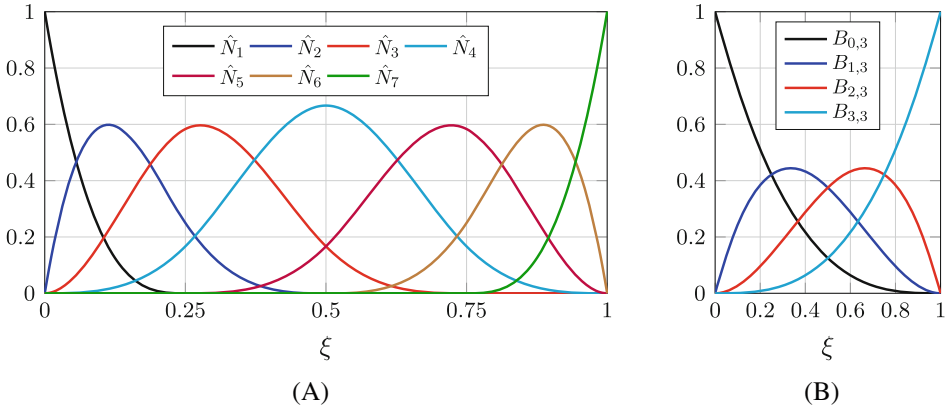


**FIGURE 3** Isogeometric discretization: (A) Cubic spline basis functions $\hat{N}_A$ for the knot vector $\Xi = [0, 0, 0, 0, 0.25, 0.5, 0.75, 1, 1, 1, 1]$ and (B) cubic Bernstein polynomials $B_{i,p}$ $(i = 0, \dots, p)$

MOST WIEDZY Downloaded from mostwiedzy.pl

In Equation (64), $\hat{\mathbf{N}}^e$ is of size $n \times 1$ and contains the basis functions $\hat{N}_A, A = 1, \ldots n$. The Bézier extraction operators are of size $n \times n$, and $\mathbf{B}$ is of size $n \times 1$ and contains the Bernstein polynomials in the corresponding parametric direction. Note that instead of Bézier extraction, also Lagrange extraction can be used.[5]

## 4.2 | Discretization of the primary field

Given are the $n_e$ spline basis functions on parametric element $\Omega^e$ with global indices $i_1, \ldots, i_{n_e}$. The surface representation is then given by

$$\boldsymbol{X} \approx \boldsymbol{X}^h = \mathbf{N}^e \, \mathbf{X}_e \,, \quad \text{and} \quad \boldsymbol{x} \approx \boldsymbol{x}^h = \mathbf{N}^e \, \mathbf{x}_e, \tag{65}$$

for the reference and current surface, respectively. Here, the shape function array is

$$\mathbf{N}^e := [N_{i_1}\mathbf{1}, \; N_{i_2}\mathbf{1}, \; \ldots \, , \; N_{i_{n_e}}\mathbf{1}], \tag{66}$$

with dimension $3 \times 3\, n_e$. The $(3 \times 3)$-identity matrix is denoted $\mathbf{1}$ and the element-level vectors for the nodal displacements are denoted $\mathbf{X}_e$ and $\mathbf{x}_e$. Analogously to Equation (65), the variations of the nodal displacements on element $\Omega^e$ are

$$\delta\boldsymbol{X}^h = \mathbf{N}^e \, \delta\mathbf{X}_e \,, \quad \text{and} \quad \delta\boldsymbol{x}^h = \mathbf{N}^e \, \delta\mathbf{x}_e. \tag{67}$$

The discretized covariant tangent vectors, see also Equation (1.1), follow as

$$\boldsymbol{A}^h_\alpha = \mathbf{N}^e_{,\alpha} \, \mathbf{X}_e \,, \quad \text{and} \quad \boldsymbol{a}^h_\alpha = \mathbf{N}^e_{,\alpha} \, \mathbf{x}_e, \tag{68}$$

with $\mathbf{N}^e{}_{,\alpha} = \partial \mathbf{N}^e / \partial \xi^\alpha$. The discretized surface normals $\boldsymbol{N}^h$ and $\boldsymbol{n}^h$ follow in analogy to Equation (1.2). The metric and curvature tensor components are then given by

$$A^h_{\alpha\beta} = \mathbf{X}_e^{\mathrm{T}} \left(\mathbf{N}^e_{,\alpha}\right)^{\mathrm{T}} \mathbf{N}^e_{,\beta} \, \mathbf{X}_e \,, \quad \text{and} \quad B^h_{\alpha\beta} = \boldsymbol{N}^h \cdot \mathbf{N}^e_{,\alpha\beta} \, \mathbf{X}_e, \tag{69}$$

and

$$a^h_{\alpha\beta} = \mathbf{x}_e^{\mathrm{T}} \left(\mathbf{N}^e_{,\alpha}\right)^{\mathrm{T}} \mathbf{N}^e_{,\beta} \, \mathbf{x}_e \,, \quad \text{and} \quad b^h_{\alpha\beta} = \boldsymbol{n}^h \cdot \mathbf{N}^e_{,\alpha\beta} \, \mathbf{x}_e. \tag{70}$$

Equations (69) and (70) can then be used to compute the discretized contravariant surface metrics, $[A_h^{\alpha\beta}] = [A^h_{\alpha\beta}]^{-1}$ and $[a_h^{\alpha\beta}] = [a^h_{\alpha\beta}]^{-1}$. In analogy, the discretized variations of the surface metric and curvature are given by

$$\delta a^h_{\alpha\beta} = \delta\mathbf{x}_e^{\mathrm{T}} \left( \left(\mathbf{N}^e_{,\alpha}\right)^{\mathrm{T}} \mathbf{N}^e_{,\beta} + \left(\mathbf{N}^e_{,\beta}\right)^{\mathrm{T}} \mathbf{N}^e_{,\alpha} \right) \mathbf{x}_e \,, \quad \text{and} \quad \delta b^h_{\alpha\beta} = \delta\mathbf{x}_e^{\mathrm{T}} \left(\mathbf{N}^e_{;\alpha\beta}\right)^{\mathrm{T}} \boldsymbol{n}^h, \tag{71}$$

with

$$\mathbf{N}^e_{;\alpha\beta} := \mathbf{N}^e_{,\alpha\beta} - \Gamma^\gamma_{\alpha\beta} \, \mathbf{N}^e_{,\gamma}. \tag{72}$$

Here, the discretized Christoffel symbols of the second kind on $\mathcal{S}$ are

$$\Gamma^\gamma_{\alpha\beta} = \mathbf{x}_e^{\mathrm{T}} \left(\mathbf{N}^e_{,\alpha\beta}\right)^{\mathrm{T}} a_h^{\gamma\delta} \, \mathbf{N}^e_{,\delta} \, \mathbf{x}_e. \tag{73}$$

Note that subsequently, the superscript "h" may be omitted for notational simplicity.

Since the evolution laws for membrane and bending viscosity, see Equations (54) and (60), are purely temporal, no spatial discretization is required for $\hat{a}^{\alpha\beta}$ and $\hat{b}_{\alpha\beta}$. Thus, $\hat{a}^{\alpha\beta}$ and $\hat{b}_{\alpha\beta}$ can be treated as history variables that are evolved and stored at each quadrature point. This effectively eliminates them from the set of unknowns leading to a dependency of $\hat{a}^{\alpha\beta}$ and $\hat{b}_{\alpha\beta}$ on the primary unknown $\boldsymbol{x}$ that affects the linearization, see also Section 4.5.

MOST WIEDZY Downloaded from mostwiedzy.pl

### 4.3 | Discretized mechanical weak form

Inserting the discretization from above into Equations (25) and (26) yields the discretized mechanical weak form

$$\delta \mathbf{x}^{\mathrm{T}} \left[\mathbf{f}_{\mathrm{int}} - \mathbf{f}_{\mathrm{ext}}\right] = 0 \,, \quad \forall\, \delta\mathbf{x} \in \mathcal{U}^h, \tag{74}$$

with the finite-dimensional space $\mathcal{U}^h \subset \mathcal{U}$, and the global force vectors $\mathbf{f}_{\mathrm{int}}$ and $\mathbf{f}_{\mathrm{ext}}$. These are assembled from their element-level contributions

$$\begin{aligned}
\mathbf{f}^e_{\mathrm{int}} &:= \int_{\Omega^e} \sigma^{\alpha\beta} \left(\mathbf{N}^e_{,\alpha}\right)^{\mathrm{T}} \boldsymbol{a}^h_\beta \,\mathrm{d}a + \int_{\Omega^e} M^{\alpha\beta} \left(\mathbf{N}^e_{;\alpha\beta}\right)^{\mathrm{T}} \boldsymbol{n}^h \,\mathrm{d}a \,, \quad \text{and} \\
\mathbf{f}^e_{\mathrm{ext}} &:= \int_{\Omega^e} \left(\mathbf{N}^e\right)^{\mathrm{T}} p\, \boldsymbol{n}^h \,\mathrm{d}a + \int_{\Omega^e} \left(\mathbf{N}^e\right)^{\mathrm{T}} f^\alpha\, \boldsymbol{a}^h_\alpha \,\mathrm{d}a \,,
\end{aligned} \tag{75}$$

where $\Omega^e$ denotes the domain of element $e$ in the current configuration. In $\mathbf{f}^e_{\mathrm{ext}}$, the boundary loads $\boldsymbol{T}$ and $\boldsymbol{M}$ acting on $\partial S$ are assumed to be zero. The extension to boundary loads can be found in Duong et al.[11] The computation of the stresses $\sigma^{\alpha\beta}$ and moments $M^{\alpha\beta}$ is outlined in Section 3.

From Equation (74) follows the equation of motion at the free nodes (where no Dirichlet boundary conditions are prescribed)

$$\mathbf{f}(\mathbf{x}) = \mathbf{f}_{\mathrm{int}}(\mathbf{x}) - \mathbf{f}_{\mathrm{ext}}(\mathbf{x}) = \mathbf{0} \,, \tag{76}$$

where $\mathbf{x}$ is the global unknown, similar to the element-level unknowns $\mathbf{x}_e$.

### 4.4 | Solution of the evolution laws

In Section 3, ODEs for $\hat{a}^{\alpha\beta}$ and $\hat{b}_{\alpha\beta}$ are derived, see Equations (54) and (60). In general, they need to be solved numerically as no analytical solution exists. The temporal integration of $\hat{a}^{\alpha\beta}$ based on Equation (54) is described in Section 4.4.1, and the numerical treatment of $\hat{b}_{\alpha\beta}$ is described in Section 4.4.2.

#### 4.4.1 | Membrane material models

Given all quantities at time step $n$ and the time step size $\Delta t_{n+1} := t_{n+1} - t_n$, Equation (54) needs to be solved for $\hat{a}^{\alpha\beta}_{n+1}$. Here, an implicit/backward Euler method is employed, such that the ODEs in Equation (54) reduce to the nonlinear algebraic equations

$$\hat{\mathrm{g}}^{\alpha\beta}_{\mathrm{s}}\left(\hat{a}^{\gamma\delta}_{n+1}\right) := \frac{\hat{a}^{\alpha\beta}_{n+1} - \hat{a}^{\alpha\beta}_{n}}{\Delta t_{n+1}} + \frac{J_{\mathrm{el},n+1}}{\eta_{\mathrm{s}}}\, \sigma^{\alpha\beta}_{1(\mathrm{el})}\left(\hat{a}^{\gamma\delta}_{n+1}\right) = 0, \tag{77}$$

which need to be solved for $\hat{a}^{\alpha\beta}_{n+1}$. The initial condition is $\hat{a}^{\alpha\beta}\big|_{t=0} = A^{\alpha\beta}$. Equation (77) contains four equations, which need to be solved for the four unknowns $\hat{a}^{\alpha\beta}$. As $\hat{a}^{12} = \hat{a}^{21}$, the unknown $\hat{a}^{21}$ and the corresponding equation $\hat{\mathrm{g}}^{21}_{\mathrm{s}} = 0$ can be eliminated. Thus, there remain three equations and unknowns, which are arranged in the vectors

$$\hat{\mathbf{g}}_{\mathrm{s}} := \begin{bmatrix} \hat{\mathrm{g}}^{11}_{\mathrm{s}} \\ \hat{\mathrm{g}}^{12}_{\mathrm{s}} \\ \hat{\mathrm{g}}^{22}_{\mathrm{s}} \end{bmatrix} = \mathbf{0} \,, \quad \text{and} \quad \hat{\mathbf{a}} := \begin{bmatrix} \hat{a}^{11} \\ \hat{a}^{12} \\ \hat{a}^{22} \end{bmatrix}. \tag{78}$$

In general, it is not possible to solve Equation (78.1) analytically, and thus a local Newton–Raphson iteration is used. Using Taylor expansion, Equation (78.1) is approximated around $\hat{\mathbf{a}}_{n+1}\big|_i$ (where $i$ denotes the $i$'th Newton–Raphson step) by

MOST WIEDZY Downloaded from mostwiedzy.pl

$$\hat{\mathbf{g}}_{\mathrm{s}}\Big|_{i+1} \approx \hat{\mathbf{g}}_{\mathrm{s}}\Big|_{i} + \left.\frac{\partial \hat{\mathbf{g}}_{\mathrm{s}}}{\partial \hat{\mathbf{a}}_{n+1}}\right|_{i} \Delta\hat{\mathbf{a}}_{n+1}\Big|_{i+1} = \mathbf{0}, \tag{79}$$

where

$$\frac{\partial \hat{\mathbf{g}}_{\mathrm{s}}}{\partial \hat{\mathbf{a}}_{n+1}} = \begin{bmatrix} \partial \hat{\mathrm{g}}_{\mathrm{s}}^{11}/\partial \hat{a}_{n+1}^{11} & \partial \hat{\mathrm{g}}_{\mathrm{s}}^{11}/\partial \hat{a}_{n+1}^{12} + \partial \hat{\mathrm{g}}_{\mathrm{s}}^{11}/\partial \hat{a}_{n+1}^{21} & \partial \hat{\mathrm{g}}_{\mathrm{s}}^{11}/\partial \hat{a}_{n+1}^{22} \\ \partial \hat{\mathrm{g}}_{\mathrm{s}}^{12}/\partial \hat{a}_{n+1}^{11} & \partial \hat{\mathrm{g}}_{\mathrm{s}}^{12}/\partial \hat{a}_{n+1}^{12} + \partial \hat{\mathrm{g}}_{\mathrm{s}}^{12}/\partial \hat{a}_{n+1}^{21} & \partial \hat{\mathrm{g}}_{\mathrm{s}}^{12}/\partial \hat{a}_{n+1}^{22} \\ \partial \hat{\mathrm{g}}_{\mathrm{s}}^{22}/\partial \hat{a}_{n+1}^{11} & \partial \hat{\mathrm{g}}_{\mathrm{s}}^{22}/\partial \hat{a}_{n+1}^{12} + \partial \hat{\mathrm{g}}_{\mathrm{s}}^{22}/\partial \hat{a}_{n+1}^{21} & \partial \hat{\mathrm{g}}_{\mathrm{s}}^{22}/\partial \hat{a}_{n+1}^{22} \end{bmatrix}. \tag{80}$$

Note that the sum in the second column of Equation (80) occurs because the variable $\hat{a}^{21}$ is eliminated, as mentioned above. Provided the starting guess $\hat{\mathbf{a}}_{n+1}\big|_0 = \hat{\mathbf{a}}_n$, the iteration $(i = 0, 1, 2, \dots)$

$$\text{solve} \quad \left.\frac{\partial \hat{\mathbf{g}}_{\mathrm{s}}(\hat{\mathbf{a}}_{n+1})}{\partial \hat{\mathbf{a}}_{n+1}}\right|_{i} \Delta\hat{\mathbf{a}}_{n+1}\Big|_{i+1} = -\hat{\mathbf{g}}_{\mathrm{s}}(\hat{\mathbf{a}}_{n+1})\Big|_{i} \quad \text{for } \Delta\hat{\mathbf{a}}_{n+1}\Big|_{i+1}, \text{update} \quad \hat{\mathbf{a}}_{n+1}\Big|_{i+1} = \hat{\mathbf{a}}_{n+1}\Big|_{i} + \Delta\hat{\mathbf{a}}_{n+1}\Big|_{i+1}, \tag{81}$$

is repeated until convergence is obtained. Convergence is monitored by checking if

$$\left\|\Delta\hat{\mathbf{a}}_{n+1}\Big|_{i+1}\right\|_2 \leq 10^{-10}. \tag{82}$$

Subsequently, the algebraic equations following from Equation (77) are specified for all the membrane material models of Section 3. The index "$n+1$" is omitted for notational simplicity in the subsequent sections. Every quantity without index "$n$" is evaluated at the current time step.

*Koiter membrane model*

Given the material model from Equation (33),§ Equation (77) becomes

$$\hat{\mathrm{g}}_{\mathrm{s}}^{\alpha\beta}\left(\hat{a}^{\gamma\delta}\right) = \frac{\hat{a}^{\alpha\beta} - \hat{a}_n^{\alpha\beta}}{\Delta t} + \frac{\Lambda_1}{2\,\eta_{\mathrm{s}}}\left(I_1^{\mathrm{el}} - 2\right)\,\hat{a}^{\alpha\beta} + \frac{\mu_1}{\eta_{\mathrm{s}}}\left(\hat{a}^{\alpha\gamma}\,a_{\gamma\delta}\,\hat{a}^{\beta\delta} - \hat{a}^{\alpha\beta}\right) = 0. \tag{83}$$

*Neo-Hookean membrane model*

Considering the material model from Equation (36) with $\Lambda = 0$,§ Equation (77) becomes

$$\hat{\mathrm{g}}_{\mathrm{s}}^{\alpha\beta}\left(\hat{a}^{\gamma\delta}\right) = \frac{\hat{a}^{\alpha\beta} - \hat{a}_n^{\alpha\beta}}{\Delta t} + \frac{\mu_1}{\eta_{\mathrm{s}}}\left(\hat{a}^{\alpha\beta} - a^{\alpha\beta}\right) = 0. \tag{84}$$

This is a linear model that can be solved directly for $\hat{a}^{\alpha\beta}$ (without using Equation (81)) giving

$$\hat{a}^{\alpha\beta} = \frac{\eta_{\mathrm{s}}\,\hat{a}_n^{\alpha\beta} + \mu_1\,\Delta t\,a^{\alpha\beta}}{\eta_{\mathrm{s}} + \mu_1\,\Delta t}. \tag{85}$$

*Neo-Hookean membrane model with dilatational/deviatoric split*

For the material model from Equation (38),§ Equation (77) becomes

$$\hat{\mathrm{g}}_{\mathrm{s}}^{\alpha\beta}\left(\hat{a}^{\gamma\delta}\right) = \frac{\hat{a}^{\alpha\beta} - \hat{a}_n^{\alpha\beta}}{\Delta t} + \frac{K_1}{2\,\eta_{\mathrm{s}}}\left(J_{\mathrm{el}}^2 - 1\right)\,a^{\alpha\beta} + \frac{\mu_1}{2\,\eta_{\mathrm{s}}\,J_{\mathrm{el}}}\left(2\,\hat{a}^{\alpha\beta} - I_1^{\mathrm{el}}a^{\alpha\beta}\right) = 0. \tag{86}$$

*Incompressible Neo-Hookean membrane model*

For the material model from Equation (41),§ Equation (77) becomes

$$\hat{\mathrm{g}}_{\mathrm{s}}^{\alpha\beta}\left(\hat{a}^{\gamma\delta}\right) = \frac{\hat{a}^{\alpha\beta} - \hat{a}_n^{\alpha\beta}}{\Delta t} + \frac{\mu_1}{\eta_{\mathrm{s}}}\left(\hat{a}^{\alpha\beta} - \frac{a^{\alpha\beta}}{J_{\mathrm{el}}^2}\right) = 0. \tag{87}$$

MOST WIEDZY Downloaded from mostwiedzy.pl

*Membranes with constant surface tension*

Considering the material model from Equation (42),[§] Equation (77) becomes

$$\hat{\mathrm{g}}_{\mathrm{s}}^{\alpha\beta}\left(\hat{a}^{\gamma\delta}\right) = \frac{\hat{a}^{\alpha\beta} - \hat{a}_n^{\alpha\beta}}{\Delta t} + \frac{\hat{\gamma}}{\eta_{\mathrm{s}}}\, J_{\mathrm{el}}\, a^{\alpha\beta} = 0, \tag{88}$$

where $\hat{\gamma}$ denotes the prescribed surface tension w.r.t. the intermediate configuration.

### 4.4.2 | Bending material models

The numerical time integration of the evolution laws for bending viscosity follows in analogy to the presented scheme for the evolution laws for membrane viscosity. In analogy to Equation (77), the ODEs in Equation (60) reduce to the nonlinear algebraic equations

$$\hat{\mathrm{g}}_{\alpha\beta}^{\mathrm{b}}\left(\hat{b}_{\gamma\delta}\right) := \frac{\hat{b}_{\alpha\beta} - \hat{b}_{\alpha\beta}^{n}}{\Delta t} - \frac{J_{\mathrm{el}}}{\eta_{\mathrm{b}}}\, M_{\alpha\beta}^{(1)(\mathrm{el})}\left(\hat{b}_{\gamma\delta}\right) = 0, \tag{89}$$

with initial condition $\hat{b}_{\alpha\beta}\big|_{t=0} = B_{\alpha\beta}$.

*Koiter bending model*

The algebraic equations, see Equation (89),[¶] for the material model from Equation (44) become

$$\hat{\mathrm{g}}_{\alpha\beta}^{\mathrm{b}}\left(\hat{b}_{\gamma\delta}\right) = \frac{\hat{b}_{\alpha\beta} - \hat{b}_{\alpha\beta}^{n}}{\Delta t} + \frac{c_1}{\eta_{\mathrm{b}}}\,\left(\hat{b}_{\alpha\beta} - b_{\alpha\beta}\right) = 0. \tag{90}$$

This is also a linear model that can be directly solved for $\hat{b}_{\alpha\beta}$, similar to Equation (85).

*Helfrich bending model*

For the material model from Equation (46) with $k^\star = 0$,[§,¶] Equations (77) and (89) become

$$\hat{\mathrm{g}}_{\mathrm{s}}^{\alpha\beta}\left(\hat{a}^{\gamma\delta}\right) = \frac{\hat{a}^{\alpha\beta} - \hat{a}_n^{\alpha\beta}}{\Delta t} + \frac{k_1\, J_{\mathrm{el}}}{\eta_{\mathrm{b}}}\,\left[\left(H - \hat{H}\right)^2 a^{\alpha\beta} - 2\,\left(H - \hat{H}\right)\, b^{\alpha\beta}\right] = 0, \tag{91}$$

and

$$\hat{\mathrm{g}}_{\alpha\beta}^{\mathrm{b}}\left(\hat{b}_{\gamma\delta}\right) = \frac{\hat{b}_{\alpha\beta} - \hat{b}_{\alpha\beta}^{n}}{\Delta t} - \frac{k_1\, J_{\mathrm{el}}}{\eta_{\mathrm{b}}}\,\left(H - \hat{H}\right)\, a_{\alpha\beta} = 0. \tag{92}$$

The derivatives of all these material models, which are required in Equation (80), are reported in Appendix A.2.

*Remark* 5. For coupled membrane and bending viscosity, iteration (81) has to be performed for the unknowns $\hat{a}^{\alpha\beta}$ and $\hat{b}_{\alpha\beta}$ simultaneously. The linear equation system in Equation (81.1) then becomes

$$\begin{bmatrix} \partial\hat{\mathbf{g}}_{\mathrm{s}}\left(\hat{\mathbf{a}}_{n+1}, \hat{\mathbf{b}}_{n+1}\right)/\partial\hat{\mathbf{a}}_{n+1} & \partial\hat{\mathbf{g}}_{\mathrm{s}}\left(\hat{\mathbf{a}}_{n+1}, \hat{\mathbf{b}}_{n+1}\right)/\partial\hat{\mathbf{b}}_{n+1} \\ \partial\hat{\mathbf{g}}^{\mathrm{b}}\left(\hat{\mathbf{a}}_{n+1}, \hat{\mathbf{b}}_{n+1}\right)/\partial\hat{\mathbf{a}}_{n+1} & \partial\hat{\mathbf{g}}^{\mathrm{b}}\left(\hat{\mathbf{a}}_{n+1}, \hat{\mathbf{b}}_{n+1}\right)/\partial\hat{\mathbf{b}}_{n+1} \end{bmatrix}_i \begin{bmatrix} \Delta\hat{\mathbf{a}}_{n+1} \\ \Delta\hat{\mathbf{b}}_{n+1} \end{bmatrix}_{i+1} = -\begin{bmatrix} \hat{\mathbf{g}}_{\mathrm{s}}\left(\hat{\mathbf{a}}_{n+1}, \hat{\mathbf{b}}_{n+1}\right) \\ \hat{\mathbf{g}}_{\mathrm{b}}\left(\hat{\mathbf{a}}_{n+1}, \hat{\mathbf{b}}_{n+1}\right) \end{bmatrix}_i, \tag{93}$$

where the vector $\hat{\mathbf{b}}$ arranges the terms $\hat{b}_{\alpha\beta}$ analogously to Equation (78.2). For example, the discretized evolution laws for the Helfrich model, see Equations (91) and (92), lead to coupled membrane and bending viscosity, see also Equations (A11) and (A12).

*Remark* 6. Examining Equation (85) shows that the absolute value of the factor in front of $\hat{a}_n^{\alpha\beta}$ is $\eta_{\mathrm{s}}/(\eta_{\mathrm{s}} + \mu_1\,\Delta t)$, which is smaller to one and thus, the method is stable. For the explicit Euler scheme, this factor would be $|(\eta_{\mathrm{s}} - \mu_1\,\Delta t)/\eta_{\mathrm{s}}|$,

MOST WIEDZY Downloaded from mostwiedzy.pl

which might become larger to one, such that the method is not stable. Thus, the implicit Euler scheme is used in this work.

*Remark* 7. The presented formulation of membrane viscosity leads to ODEs for the intermediate surface metric $\hat{a}^{\alpha\beta}$. For some discretizations, for example, based on unstructured splines, solving for $\hat{a}^{\alpha\beta}$ might lead to numerical ill-conditioning. For instance, at the extraordinary points of an unstructured spline sphere,[86] the parametrization becomes singular, that is, one tangent vector $\boldsymbol{a}_\alpha$ approaches $\mathbf{0}$. The computation of the inverse $[a^{\alpha\beta}] = [a_{\alpha\beta}]^{-1}$ then might lead to numerical ill-conditioning. The same problem pertains to the intermediate surface metric $\hat{a}^{\alpha\beta}$. In order to resolve this issue, the ODEs for $\hat{a}^{\alpha\beta}$ may be reformulated, for example, as ODEs for $I_1^{\text{el}}$, $J_{\text{in}}$, and $J_{\text{el}}$, but also other options could be possible, for instance based on the Cauchy–Green tensor $\boldsymbol{C}_{\text{el}}$.

## 4.5 | Solution of the nonlinear equation system

The nonlinear equation system in Equation (76) is solved using a global Newton–Raphson iteration. This scheme requires the linearization of the force vector in Equation (76). This leads to the element-level stiffness matrix $\mathbf{k}^e := \mathbf{k}^e_{\tau\tau} + \mathbf{k}^e_{\tau M} + \mathbf{k}^e_{M\tau} + \mathbf{k}^e_{MM} + \mathbf{k}^e_{\tau} + \mathbf{k}^e_{M}$ with the element-level material stiffness matrices

$$\begin{aligned}
\mathbf{k}^e_{\tau\tau} &:= \int_{\Omega^e_0} c^{\alpha\beta\gamma\delta} \left(\mathbf{N}^e_{,\alpha}\right)^{\mathrm{T}} \left(\boldsymbol{a}_\beta \otimes \boldsymbol{a}_\gamma\right) \mathbf{N}^e_{,\delta} \, \mathrm{d}A \,, \quad \mathbf{k}^e_{\tau M} := \int_{\Omega^e_0} d^{\alpha\beta\gamma\delta} \left(\mathbf{N}^e_{,\alpha}\right)^{\mathrm{T}} \left(\boldsymbol{a}_\beta \otimes \boldsymbol{n}\right) \mathbf{N}^e_{;\gamma\delta} \, \mathrm{d}A \,, \\
\mathbf{k}^e_{M\tau} &:= \int_{\Omega^e_0} e^{\alpha\beta\gamma\delta} \left(\mathbf{N}^e_{;\alpha\beta}\right)^{\mathrm{T}} \left(\boldsymbol{n} \otimes \boldsymbol{a}_\gamma\right) \mathbf{N}^e_{,\delta} \, \mathrm{d}A \,, \quad \mathbf{k}^e_{MM} := \int_{\Omega^e_0} f^{\alpha\beta\gamma\delta} \left(\mathbf{N}^e_{;\alpha\beta}\right)^{\mathrm{T}} \left(\boldsymbol{n} \otimes \boldsymbol{n}\right) \mathbf{N}^e_{;\gamma\delta} \, \mathrm{d}A \,,
\end{aligned} \tag{94}$$

and the element-level geometric stiffness matrices

$$\mathbf{k}^e_{\tau} := \int_{\Omega^e_0} \left(\mathbf{N}^e_{,\alpha}\right)^{\mathrm{T}} \tau^{\alpha\beta} \, \mathbf{N}^e_{,\beta} \, \mathrm{d}A \,, \quad \text{and} \quad \mathbf{k}^e_{M} := \mathbf{k}^e_{M1} + \mathbf{k}^e_{M2} + (\mathbf{k}^e_{M2})^{\mathrm{T}}, \tag{95}$$

with

$$\begin{aligned}
\mathbf{k}^e_{M1} &:= -\int_{\Omega^e_0} b_{\alpha\beta} \, M_0^{\alpha\beta} \, a^{\gamma\delta} \left(\mathbf{N}^e_{,\gamma}\right)^{\mathrm{T}} \left(\boldsymbol{n} \otimes \boldsymbol{n}\right) \mathbf{N}^e_{,\delta} \, \mathrm{d}A \,, \quad \text{and} \\
\mathbf{k}^e_{M2} &:= -\int_{\Omega^e_0} M_0^{\alpha\beta} \left(\mathbf{N}^e_{,\gamma}\right)^{\mathrm{T}} \left(\boldsymbol{n} \otimes \boldsymbol{a}^\gamma\right) \mathbf{N}^e_{;\alpha\beta} \, \mathrm{d}A \,,
\end{aligned} \tag{96}$$

see Duong et al.[11] for more details and for the linearization of the external element-level force vector $\mathbf{f}^e_{\text{ext}}$ in Equation (75.2). In Equation (94), the material tangents

$$c^{\alpha\beta\gamma\delta} = 2\,\frac{\partial \tau^{\alpha\beta}}{\partial a_{\gamma\delta}} \,, \quad d^{\alpha\beta\gamma\delta} = \frac{\partial \tau^{\alpha\beta}}{\partial b_{\gamma\delta}} \,, \quad e^{\alpha\beta\gamma\delta} = 2\,\frac{\partial M_0^{\alpha\beta}}{\partial a_{\gamma\delta}} \,, \quad \text{and} \quad f^{\alpha\beta\gamma\delta} = \frac{\partial M_0^{\alpha\beta}}{\partial b_{\gamma\delta}}, \tag{97}$$

need to be defined for the employed material model. As the stresses and moments are composed of elastic and Maxwell components, see Equations (49) and (57), the material tangents in Equation (97) will also be composed of the two contributions

$$\tilde{c}^{\alpha\beta\gamma\delta} = \tilde{c}_0^{\alpha\beta\gamma\delta} + \tilde{c}_1^{\alpha\beta\gamma\delta} \,, \quad \tilde{c} = c, d, e, f, \tag{98}$$

where again the index "0" refers to the elastic branch and "1" refers to the Maxwell branch. The Maxwell material tangents $\tilde{c}_1^{\alpha\beta\gamma\delta}$ in Equation (98) are derived in Appendix A.3.

*Remark* 8. In Sauer et al.,[65] the variables $\hat{a}_{\alpha\beta}$ and $\hat{b}_{\alpha\beta}$ are assumed to be independent variables from $a_{\alpha\beta}$ and $b_{\alpha\beta}$. In this work here, the unknowns $\hat{a}_{\alpha\beta}$ and $\hat{b}_{\alpha\beta}$ are locally eliminated by solving Equations (54) and (60) at each quadrature point, see Section 4.4. This elimination makes $\hat{a}_{\alpha\beta}$ and $\hat{b}_{\alpha\beta}$ a function of $a_{\alpha\beta}$ and $b_{\alpha\beta}$, which leads to additional derivatives in the linearization that are not appearing in the theory of Sauer et al.[65]

MOST WIEDZY Downloaded from mostwiedzy.pl

### 4.6 | Summary of the computational formulation for viscoelastic shells

A concise summary of the presented computational formulation for viscoelastic shells is given in Table 1.

## 5 | NUMERICAL EXAMPLES

This section presents several numerical examples that illustrate viscoelastic behavior of shells. In Section 5.1, typical viscoelastic behavior is investigated on two-dimensional square membranes. The implementation of membrane, bending, and coupled membrane and bending viscosity is then verified in Sections 5.2–5.4. In Section 5.5, a viscoelastic Scordelis-Lo roof is investigated to illustrate inhomogeneous deformations. Section 5.6 shows that the presented formulation is also capable of modeling boundary viscoelasticity of 3D bodies. For all examples in this section, the surface is discretized by bi-quadratic NURBS, if not stated otherwise. Numerical integration on the bi-unit parent element is performed using Gaussian quadrature with $(p+1)\times(q+1)$ quadrature points, which represents a very conservative approach. Here, $p$ and $q$ refer to the polynomial orders of the surface discretization in the two parametric directions. To post-process the surface quantities $\hat{a}_{\alpha\beta}$ and $\hat{b}_{\alpha\beta}$ at any point on the surface, an $L^2$-projection is employed to map these values from the quadrature point level to the control point level. All quantities in this section are non-dimensionalized by the introduction of a reference length $L_0$, time $T_0$, and stiffness $\mu_0$, $K_0$, or $c_0$. For all examples, the shear viscosity model from Equation (51) is employed.

### 5.1 | 2D viscoelastic membrane

The first examples study two-dimensional viscoelasticity of an initially square membrane to demonstrate typical viscoelastic behavior, such as stress relaxation, creep, and strain rate dependence. Figure 4 shows the two setups that are used in

**TABLE 1** Summary of the computational formulation for viscoelastic shells

The governing nonlinear equation system for the shell deformation is

$$\mathbf{f}(\mathbf{x}) = \mathbf{f}_{\text{int}}(\mathbf{x}) - \mathbf{f}_{\text{ext}}(\mathbf{x}) = \mathbf{0}\,,$$

which is assembled from the element-level contributions

$$\mathbf{f}^e_{\text{int}} := \int_{\Omega^e} \sigma^{\alpha\beta}\, \mathbf{N}^{\mathrm{T}}_{,\alpha}\, \boldsymbol{a}^h_\beta \,\mathrm{d}a + \int_{\Omega^e} M^{\alpha\beta}\, \mathbf{N}^{\mathrm{T}}_{;\alpha\beta}\, \boldsymbol{n}^h \,\mathrm{d}a\,, \quad \text{and}$$

$$\mathbf{f}^e_{\text{ext}} := \int_{\Omega^e} \mathbf{N}^{\mathrm{T}}\, p\, \boldsymbol{n}^h \,\mathrm{d}a + \int_{\Omega^e} \mathbf{N}^{\mathrm{T}}\, f^\alpha\, \boldsymbol{a}^h_\alpha \,\mathrm{d}a\,.$$

The stresses and moments (considering one Maxwell branch) are given by

$$\sigma^{\alpha\beta} = \sigma_0^{\alpha\beta}\left(a^{\gamma\delta}\right) + \sigma_1^{\alpha\beta}\left(\hat{a}^{\gamma\delta}\right)\,, \quad \text{and} \quad M^{\alpha\beta} = M^{\alpha\beta}_{(0)}\left(b^{\gamma\delta}\right) + M^{\alpha\beta}_{(1)}\left(\hat{b}^{\gamma\delta}\right)\,.$$

Here, $\sigma_0^{\alpha\beta}$, $\sigma_1^{\alpha\beta} = \sigma^{\alpha\beta}_{1(\text{el})}$, $M^{\alpha\beta}_{(0)}$, and $M^{\alpha\beta}_{(1)} = M^{\alpha\beta}_{(1)(\text{el})}$ follow from a specific choice of the elastic energy density, see Section 3.1 for examples. The Maxwell stress $\sigma_1^{\alpha\beta}$ and moment $M^{\alpha\beta}_{(1)}$ follow from the conditions in Equations (50) and (58). For the simple shear viscosity models in Equations (51) and (59), the evolution laws for $\hat{a}^{\alpha\beta}$ and $\hat{b}_{\alpha\beta}$ are given by

$$\dot{\hat{a}}^{\alpha\beta} = -\frac{J_{\text{el}}}{\eta_{\text{s}}}\, \sigma^{\alpha\beta}_{1(\text{el})}\left(\hat{a}^{\gamma\delta}\right)\,, \quad \text{and} \quad \dot{\hat{b}}_{\alpha\beta} = \frac{J_{\text{el}}}{\eta_{\text{b}}}\, M^{(1)(\text{el})}_{\alpha\beta}\left(\hat{b}_{\gamma\delta}\right)\,,$$

with initial conditions $\hat{a}^{\alpha\beta}|_{t=0} = A^{\alpha\beta}$ and $\hat{b}_{\alpha\beta}|_{t=0} = B_{\alpha\beta}$. The resulting ODEs are solved with the implicit Euler scheme, which leads to the temporal discretized nonlinear equations

$$\hat{\mathrm{g}}^{\alpha\beta}_{\text{s}}\left(\hat{a}^{\gamma\delta}\right) := \frac{\hat{a}^{\alpha\beta} - \hat{a}^{\alpha\beta}_n}{\Delta t} + \frac{J_{\text{el}}}{\eta_{\text{s}}}\, \sigma^{\alpha\beta}_{1(\text{el})}\left(\hat{a}^{\gamma\delta}\right) = 0\,, \quad \text{and}$$

$$\hat{\mathrm{g}}^{\text{b}}_{\alpha\beta}\left(\hat{b}_{\gamma\delta}\right) := \frac{\hat{b}_{\alpha\beta} - \hat{b}^n_{\alpha\beta}}{\Delta t} - \frac{J_{\text{el}}}{\eta_{\text{b}}}\, M^{(1)(\text{el})}_{\alpha\beta}\left(\hat{b}_{\gamma\delta}\right) = 0\,,$$

which are solved with a local Newton–Raphson method, see Equation (81).

To solve $\mathbf{f}(\mathbf{x}) = \mathbf{0}$, a global Newton–Raphson method is employed. The required stiffness matrix is

$$\mathbf{k}^e := \mathbf{k}^e_{\tau\tau} + \mathbf{k}^e_{\tau M} + \mathbf{k}^e_{M\tau} + \mathbf{k}^e_{MM} + \mathbf{k}^e_{\tau} + \mathbf{k}^e_{M}\,,$$

with the individual terms given in Equations (94)–(96). The material tangents in the material stiffness matrices are computed from

$$\tilde{c}^{\alpha\beta\gamma\delta} = \tilde{c}_0^{\alpha\beta\gamma\delta} + \tilde{c}_1^{\alpha\beta\gamma\delta}\,, \quad \tilde{c} = c, d, e, f\,,$$

where the index "0" refers to the elastic branch and "1" refers to the Maxwell branch. The material tangent $\tilde{c}_1^{\alpha\beta\gamma\delta}$ is derived in Appendix A.3 for various material models.

MOST WIEDZY Downloaded from mostwiedzy.pl

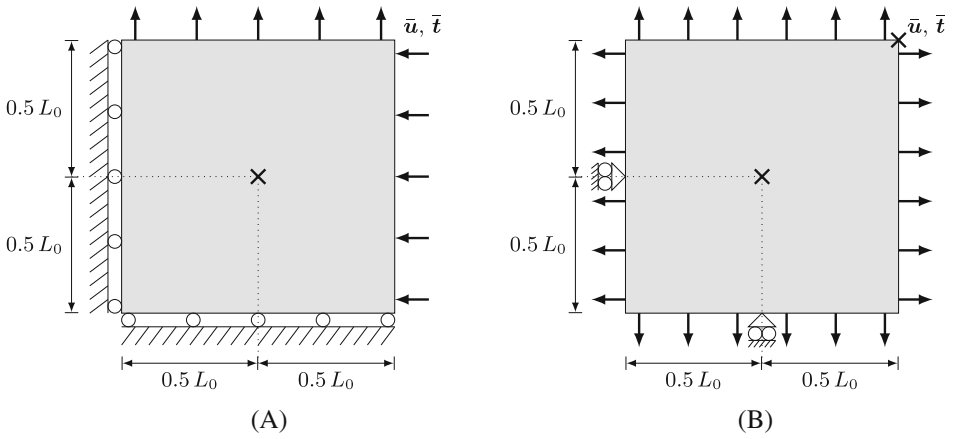


**FIGURE 4** 2D viscoelastic membrane: Geometry, loading and boundary conditions for (A) pure shear and (B) pure dilatation. The black crosses mark the positions where surface quantities are evaluated

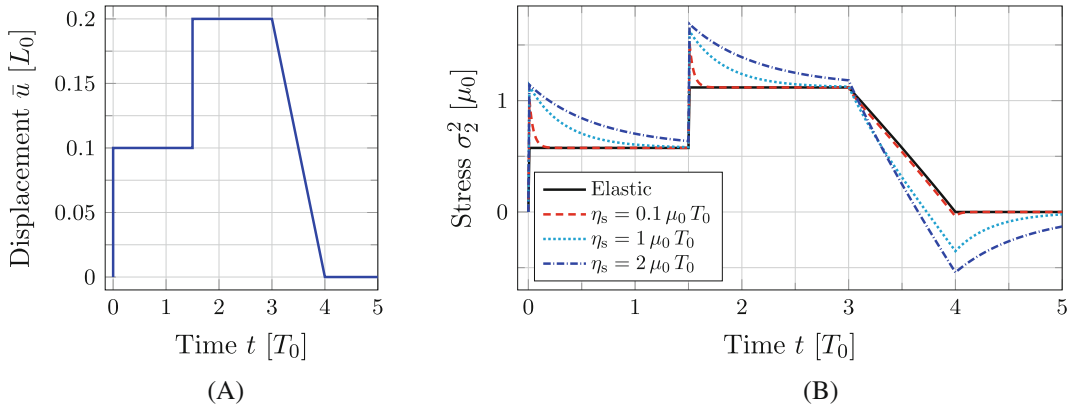


**FIGURE 5** 2D viscoelastic membrane: Stress relaxation for pure shear (according to Figure 4A). (A) Imposed displacement; (B) resulting stress

this section to model pure shear and pure dilatation. The black crosses in the figures mark the positions where the surface quantities are evaluated for visualization. Since the deformations are homogeneous, a single finite element is used for the computation, if not stated otherwise.

### 5.1.1 | Stress relaxation

First, the setup in Figure 4A is considered and the Neo-Hookean material model is employed for both the elastic and Maxwell branch, see Equation (38). The material parameters in the elastic branch are $\mu = 3\ \mu_0$ and $K = 0$; the ones in the Maxwell branch are $\mu_1 = \mu$ and $K_1 \in \{0, \mu/3\}$. The end time is $t_{\text{end}} = 5\,T_0$ and the constant time step size is chosen as $\Delta t = 0.1\ T_0$.

On the top edge, the displacement profile as shown in Figure 5A is imposed, which leads to the stretch $\lambda_y = 1 + \bar{u}/L_0$. On the right edge, the stretch $\lambda_x = 1/\lambda_y$ is imposed to ensure pure shear.

The resulting stress $\sigma_2^{2,\#}$ which is composed of elastic and Maxwell stresses, is shown over time in Figure 5B for three different values of the in-plane shear viscosity $\eta_s$ and the purely elastic case. The stress exhibits jumps whenever there is a jump of the imposed displacement. In the viscoelastic case, the magnitude of the stress is higher because the Maxwell stress is added to the total stress, see Equation (49). Over time, the Maxwell stress relaxes such that the elastic stress level is approached. In Figure 6, the invariants $I_1$ and $I_1^{\text{el}}$ from Equations (9.1) and (21) are visualized over time. For

MOST WIEDZY Downloaded from mostwiedzy.pl

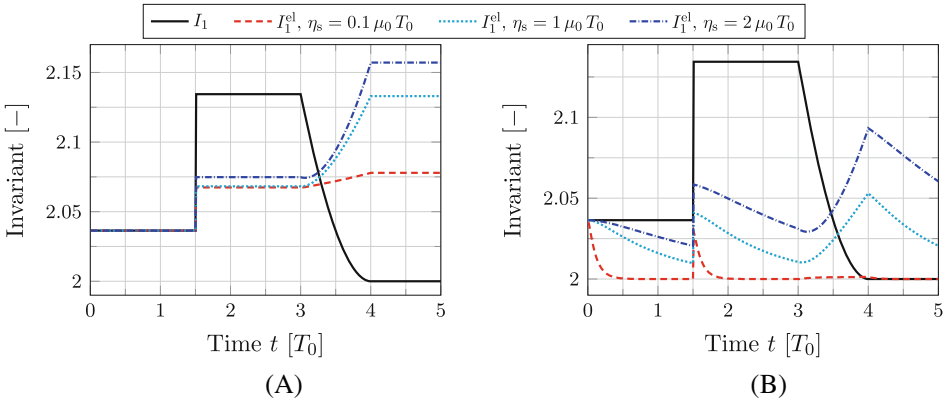


**FIGURE 6** 2D viscoelastic membrane: Stress relaxation for pure shear: First invariant for the imposed displacement profile from Figure 6A and two different areal bulk moduli $K_1$. (A) $K_1 = 0$; (B) $K_1 = \mu/3$

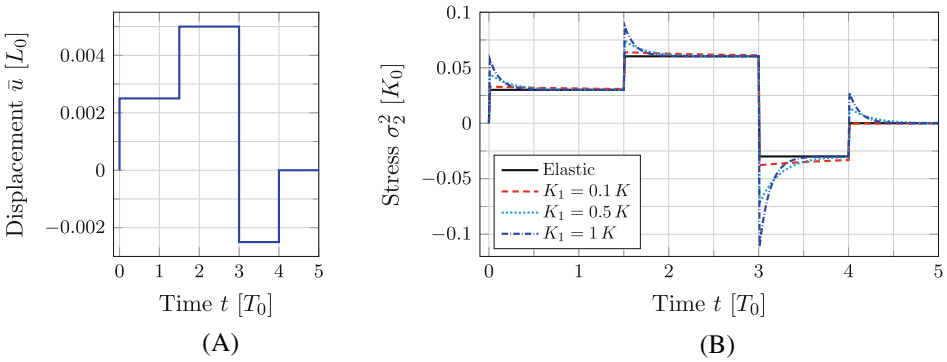


**FIGURE 7** 2D viscoelastic membrane: Stress relaxation for pure dilatation (according to Figure 4B). (A) Imposed displacement; (B) resulting stress

$K_1 = 0$, the elastic invariant $I_1^{\mathrm{el}}$ is monotonically increasing. In contrast, if $K_1$ is not vanishing, $I_1^{\mathrm{el}}$ decreases to its initial value. This happens faster for lower values of $\eta_s$. This behavior happens because the employed shear viscosity model from Equation (51) is not a pure shear model. Instead, it causes both shear and dilatation.

Next, pure dilatation is considered, see Figure 4B, and the Koiter material model is employed, see Equation (33). The material parameters in the elastic branch are $\mu = 0$ and $\Lambda = K = 3\,K_0$; the ones in the Maxwell branch are $\mu_1 = 0, \Lambda_1 = K_1$ and $\eta_s = 0.33\ K_0\ T_0$. The time stepping is the same as in the previous example. The displacement profile from Figure 7A is imposed, and the surface quantities are evaluated at the center of the sheet, see Figure 4B. The resulting stress $\sigma_2^2$ is shown in Figure 7B, which exhibits similar behavior as in the previous example. For larger values of $K_1$, the total stress is larger and the relaxation time decreases. The inelastic and elastic surface stretches, $J_{\mathrm{in}}$ and $J_{\mathrm{el}}$, respectively, are visualized in Figure 8. For larger values of $K_1$, the inelastic surface stretch is also larger, whereas the elastic surface stretch decreases. Note that the total surface stretch $J = J_{\mathrm{in}}\,J_{\mathrm{el}}$ is equal to $J_{\mathrm{el}}$ in the purely elastic case.

### 5.1.2 | Creep

Second, creep under pure dilatation (according to Figure 4B) is considered using the Neo-Hookean material model from Equation (38) with material parameters $\mu = 3\ \mu_0, K = \mu, \mu_1 = \mu$, and $K_1 = K$. The end time is $t_{\mathrm{end}} = 5\,T_0$ and the constant time step size is chosen as $\Delta t = 0.1\ T_0$. Figure 9A shows the imposed traction profile. The surface quantities are evaluated at the top right corner of the membrane, see the top right cross in Figure 4B. Figure 9B shows the resulting vertical displacement for different values of the in-plane shear viscosity $\eta_s$. A jump of the imposed traction leads to an instantaneous

MOST WIEDZY Downloaded from mostwiedzy.pl

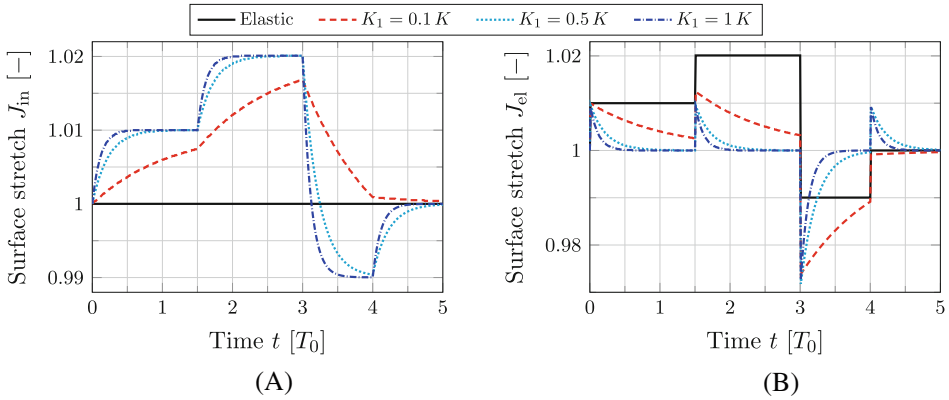


**FIGURE 8** 2D viscoelastic membrane: Stress relaxation for pure dilatation: Surface stretches for the imposed displacement profile from Figure 7A. Note that the total surface stretch $J = J_{\text{in}}\,J_{\text{el}}$ is equal to $J_{\text{el}}$ in the purely elastic case. (A) Inelastic surface stretch $J_{\text{in}}$; (B) elastic surface stretch $J_{\text{el}}$

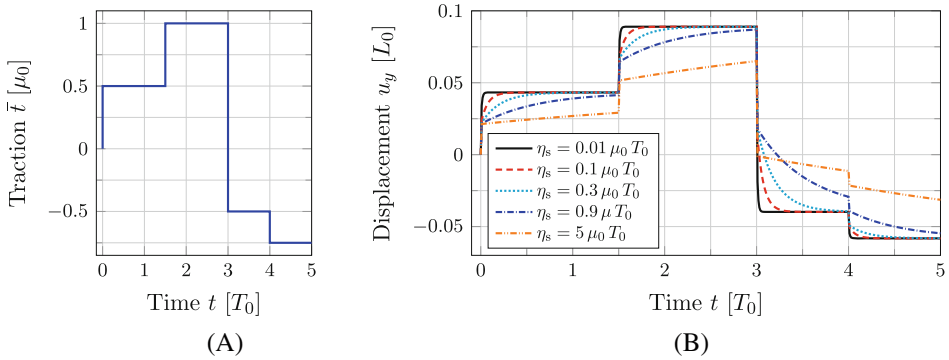


**FIGURE 9** 2D viscoelastic membrane: Creep for pure dilatation (according to Figure 4B). (A) Imposed traction; (B) resulting displacement

elastic response, that is, a jump of the displacement. Over time, the displacement magnitude increases further, which is known as creep.

### 5.1.3 | Strain rate dependence

Third, the setup in Figure 4A is used again to show the influences of different strain rates and cyclic loading. The Neo-Hookean material model from Equation (38) is used with $K_1 = \mu_1 = \mu = 1\ \mu_0, K = 0$, and the in-plane shear viscosity is set to $\eta_s = 0.25\ \mu_0\ T_0$. The imposed displacement over time is given by the function

$$\bar{u}_y(t) = 0.25\ L_0\ \sin(\omega\ t), \tag{99}$$

with excitation frequency $\omega$. At first, the time span $t \in [0, \pi/\omega]$ is considered such that only one loading-unloading cycle is computed. The time step size is constant and 500 time steps are used. Figure 10 shows the total, elastic, and Maxwell stress over the displacement. In the elastic case, the stress-displacement curve is identical for loading and unloading, see Figure 10B. But in the viscoelastic case, these curves are not coinciding. Instead, the unloading occurs at lower stress than the loading, which can be seen for both the total stress in Figure 10A and the Maxwell stress in Figure 10C. This indicates that energy is dissipated during the loading-unloading cycle, which is further studied in the next section. Figure 10 shows that with increasing excitation frequency, and thus with increasing strain rate, the Maxwell stress is larger. Further, for

MOST WIEDZY Downloaded from mostwiedzy.pl

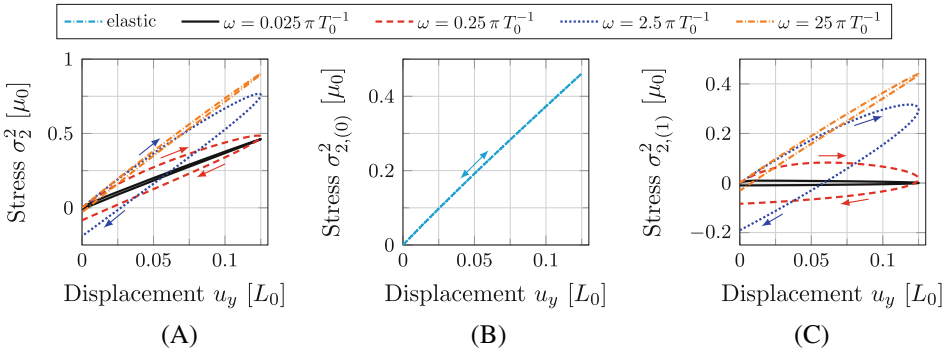


**FIGURE 10** 2D viscoelastic membrane: Strain rate dependence for one loading-unloading cycle. The Maxwell branch exhibits hysteresis—the loading and unloading curves do not coincide. (A) Total stress; (B) elastic stress; (C) Maxwell stress

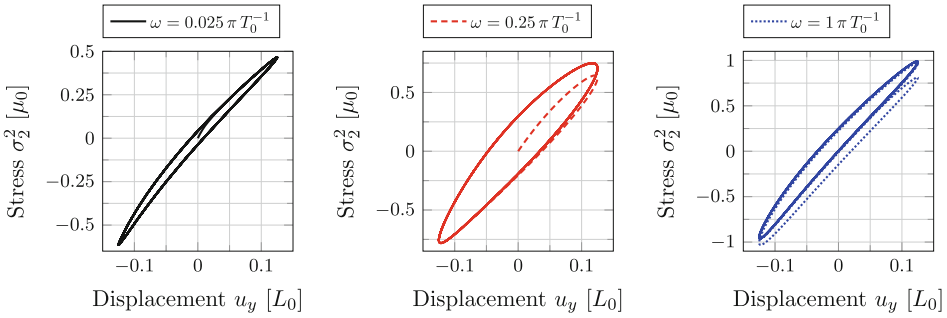


**FIGURE 11** 2D viscoelastic membrane: Hystereses for cyclic loading and different excitation frequencies

very low and very high strain rates, the loading and unloading curves come closer to each other such that less energy is dissipated.

### 5.1.4 | Cyclic loading

Fourth, the same setup as in Section 5.1.3 with the displacement profile from Equation (99) is considered, but the time span is now extended to $t \in [0, 20\,\pi/\omega]$, such that ten loading-unloading cycles occur. For this, 10,000 time steps are used. The resulting stress-displacement curves are shown in Figure 11 for three different excitation frequencies $\omega$ and $\eta_s = 1\ \mu_0\ T_0$. Note that the first loading-unloading cycle is slightly offset from the following cycles as the first one starts at zero stress, whereas the next ones start at non-vanishing stress. The areas within the hystereses are an indicator for the dissipated energy. This energy decreases for very low or very high excitation frequencies. Note that the shown results exhibit nonlinear and non-symmetric behavior in compression and tension. Figure 12 shows the dissipated energy, see Equation (53), over the excitation frequencies for three different values of $\eta_s$. For each setup, there exists an excitation frequency where the dissipation is maximum.

## 5.2 | Inflated membrane balloon

This section deals with the inflation of a viscoelastic spherical rubber balloon, similar to the elastic counterpart considered in Sauer et al.[83] This example is used to verify the formulation and implementation for membrane viscosity as an analytical solution for this problem can be derived. The finite element model is shown in Figure 13A. Only a quarter of the sphere is used for the simulation and appropriate boundary conditions are provided to prevent rigid body motion and to maintain the symmetry of the inflating balloon across the gray marked planes. The bold black lines mark the patch interfaces between the four patches, of which the quarter mesh is composed. The finite element mesh contains $6m^2$ elements, where

MOST WIEDZY Downloaded from mostwiedzy.pl

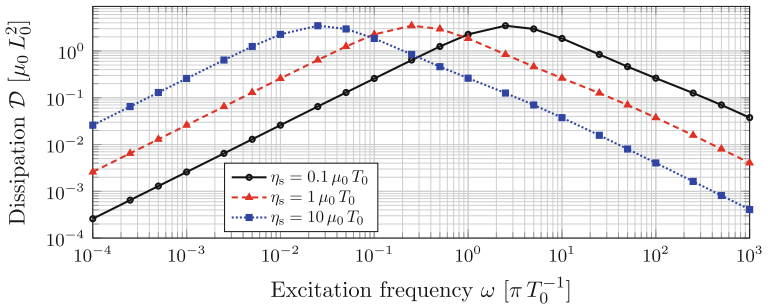


**FIGURE 12** 2D viscoelastic membrane: Dissipation $\mathcal{D}$, see Equation (53), over the excitation frequency $\omega$ for cyclic loading

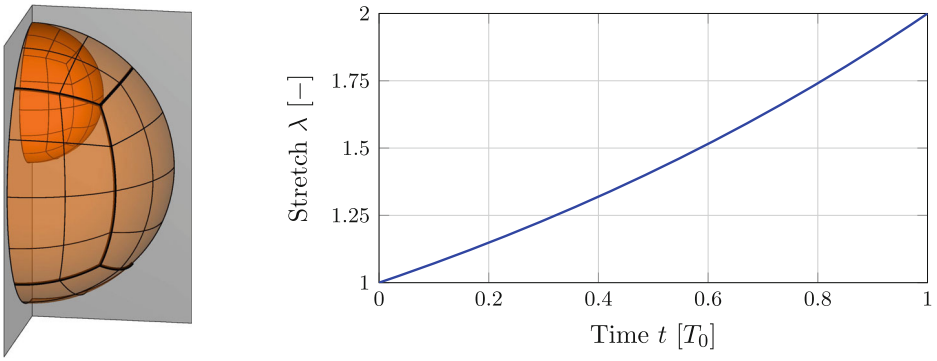


**FIGURE 13** Inflated membrane balloon: (A) Initial and deformed configuration (with the bold black lines marking patch interfaces) and (B) imposed stretch over time for $t_{\text{end}} = 1\,T_0$ and $\lambda_{\text{end}} = 2$, see Equation (100)

$2m$ ($m = 1, 2, \ldots$) denotes the number of elements along the equator of the quarter sphere. The initial and current radii are denoted $R$ and $r$, respectively. Likewise, the initial thickness is denoted $T$, while the current thickness is denoted $\tilde{t}$. As shown subsequently, the pressure initially increases but later decreases. Thus, the finite element computation is performed by imposing the enclosed volume $V$ instead of the pressure $p$, see Sauer et al.[83] for more details. The prescribed stretch $\lambda$ as a function of time $t$ is chosen as

$$\lambda(t) = \exp\left(\frac{t}{\tau_\lambda}\right), \tag{100}$$

with the characteristic time

$$\tau_\lambda := \frac{t_{\text{end}}}{\ln(\lambda_{\text{end}})}, \tag{101}$$

where $t_{\text{end}}$ denotes the end time and $\lambda_{\text{end}}$ denotes the final stretch, see Figure 13B. The choice for $\lambda(t)$ in Equation (100) allows for an analytical solution. The resulting volume is then given by

$$V(t) = \exp\left(\frac{3\,t}{\tau_\lambda}\right)\, V_0, \tag{102}$$

where the relation $V = \lambda^3\, V_0$ with initial volume $V_0$ has been used. For this example, $\lambda_{\text{end}}$ is set to 2, such that the final volume is $V(t_{\text{end}}) = 8\,V_0$. The elastic behavior of the rubber membrane is described by the incompressible Neo-Hookean material model from Equation (41), and the elastic energy in the Maxwell branch is given by Equation (36) with $\Lambda = 0$.

MOST WIEDZY Downloaded from mostwiedzy.pl

In analogy to Equation (49), the total pressure $p$ can be decomposed into the contributions

$$p(t) = p_{\text{el}}(t) + p_{\text{visc}}(t), \tag{103}$$

where $p_{\text{el}}(t)$ is the pressure function coming from the elastic branch, and $p_{\text{visc}}(t)$ is the one from the Maxwell branch. These two contributions $p_\bullet(t)$ are derived in detail in Appendix B.1, and they are given by

$$p_{\text{el}}(t) = \frac{2\,\mu}{R}\left(\frac{1}{\lambda} - \frac{1}{\lambda^7}\right) = \frac{2\,\mu}{R}\left(\left(\frac{V_0}{V}\right)^{\frac{1}{3}} - \left(\frac{V_0}{V}\right)^{\frac{7}{3}}\right). \tag{104}$$

and

$$p_{\text{visc}}(t) = \frac{2\,\mu_1}{R}\left(\frac{1}{\lambda} - \frac{1}{\lambda^3\,\hat{a}_{\text{ev}}}\right), \tag{105}$$

and

$$\hat{a}_{\text{ev}}(t) := \frac{\mu_1\,\tau_\lambda\,\exp\left(-2\,t/\tau_\lambda\right) - 2\,\eta_{\text{s}}\,\exp\left(-\mu_1\,t/\eta_{\text{s}}\right)}{\mu_1\,\tau_\lambda - 2\,\eta_{\text{s}}}. \tag{106}$$

First, the convergence of the model with respect to mesh and time step size refinement is investigated. For this, the pressure error

$$\varepsilon_p := \frac{\left|p_{\text{num}}(t_{\text{end}}) - p_{\text{ana}}(t_{\text{end}})\right|}{p_{\text{ana}}(t_{\text{end}})}, \tag{107}$$

is defined. The parameters used for the convergence study are $\mu_1 = \mu$, $\eta_{\text{s}} = 0.1\ \mu\ T_0$, and $t_{\text{end}} = 1\ T_0$. The time step size $\Delta t$ is chosen to be constant in $[0, t_{\text{end}}]$. Figure 14 clearly shows that the dominating error stems from the time step size, and not from the finite element mesh. Beyond $m \geq 2$, an increase of the number of elements for fixed $\Delta t$ does not lead to a further decrease of the error. As the deformation in this example is homogeneous, even a small number of elements is sufficient to accurately capture it. In contrast, the error decreases linearly with a decrease of the time step size $\Delta t$. This convergence rate is also the expected rate for the employed implicit Euler scheme. As the mesh $m = 2$ is sufficient to accurately capture the deformation, this mesh is used for all subsequent balloon examples.

Second, the $p(t)$ relation is shown over a logarithmic time axis in Figure 15A for different values of the in-plane shear viscosity $\eta_{\text{s}}$ and fixed $\mu_1 = \mu$, and in Figure 15B for different values of the stiffness ratio $\chi_1 := \mu_1/\mu$ and fixed $\eta_{\text{s}} = 0.5\ \mu\ T_0$.

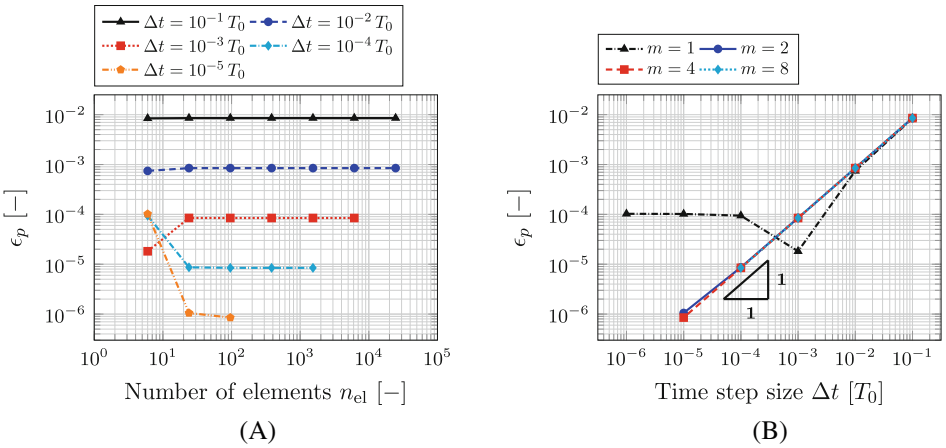


**FIGURE 14** Inflated membrane balloon: Convergence of the pressure error $\varepsilon_p$, see Equation (107), over mesh and time step size refinement. (A) Mesh refinement; (B) time step size refinement

MOST WIEDZY Downloaded from mostwiedzy.pl

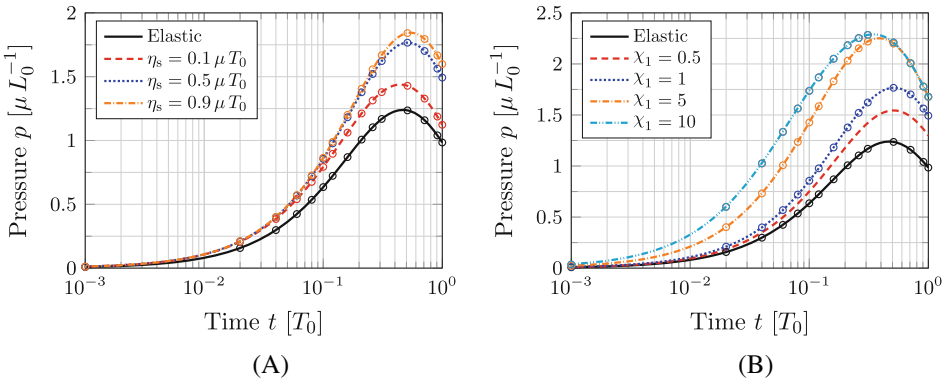


**FIGURE 15** Inflated membrane balloon: Influence of the in-plane shear viscosity $\eta_s$ and stiffness ratio $\chi_1 := \mu_1/\mu$ on the pressure $p$. The circles mark the numerical results at various snapshots in time, while the lines show the corresponding analytical results. (A) Influence of $\eta_s$; (B) influence of $\chi_1$

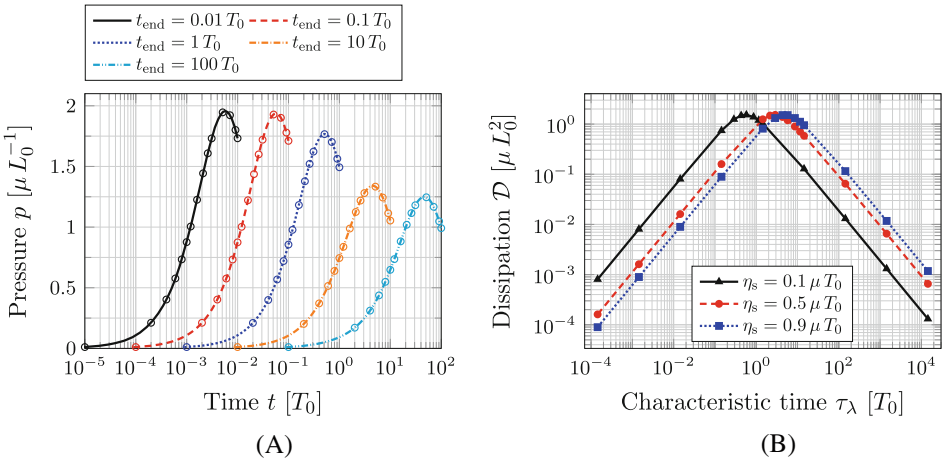


**FIGURE 16** Inflated membrane balloon: (A) Influence of the end time $t_{end}$ on the pressure $p$. Here, the circles mark the numerical results at various snapshots in time, while the lines mark the corresponding analytical results. (B) Dissipation $\mathcal{D}$, see Equation (53), over the characteristic time $\tau_\lambda$ defined in Equation (101)

The end time is fixed to $t_{end} = 1\,T_0$ and 1000 time steps are used. The strong nonlinear behavior is captured accurately by the numerical results as Figure 15 shows. For increasing values of $\eta_s$ or $\chi_1$, the magnitude of the pressure increases. The location of the maximum pressure also shifts when those parameters are varied.

Third, the effect of the loading rate is investigated. For this, the end time $t_{end}$ is varied in Equation (101), while the parameters $\eta_s = 0.5\ \mu\ T_0$ and $\chi_1 = 1$ are fixed. For the temporal integration, 1000 time steps are used. As shown in Figure 16A, the total pressure decreases for increasing $t_{end}$, and the maximum is shifted to later times. The dissipation $\mathcal{D}$, see Equation (53), is visualized in Figure 16B for three different values of the in-plane shear viscosity. For each value of $\eta_s$, there exists one characteristic time $\tau_\lambda$, see Equation (101), for which the dissipation is maximal.

## 5.3 | Pure bending of a flat strip

This section presents the pure bending of an initially flat shell to verify the formulation for viscoelastic bending. The geometry, boundary and loading conditions are shown in Figure 17. At the left and right edge, a distributed bending moment $M$ is applied. Additionally, a displacement is applied on the right edge and a pressure acts on the whole structure. This loading combination ensures that the initially flat sheet is bent into a curved sheet with curvature $\kappa_2$, but not stretched, that is, the surface stretches are exactly $\lambda_1 = \lambda_2 = 1$.[‖] The curvature is related to the radius $r$ of the deformed shell via

MOST WIEDZY Downloaded from mostwiedzy.pl

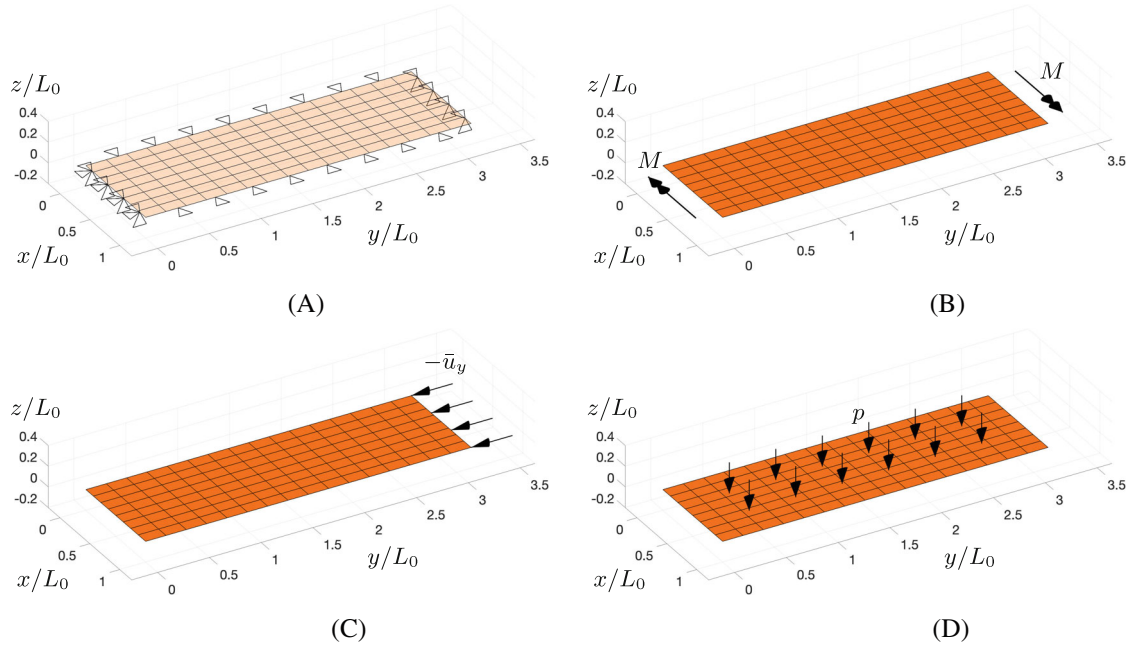


**FIGURE 17** Pure bending of a flat strip: Setup including Dirichlet boundary conditions and three different external loads that are simultaneously applied. (A) Dirichlet boundary conditions; (B) applied moments; (C) applied displacement; (D) applied pressure

$\kappa_2 = 1/r$. The membrane response in the elastic branch is based on the Neo-Hookean model from Equation (36), and the bending response in the elastic and Maxwell branch is based on the Koiter bending model from Equation (44).

Choosing the applied moment

$$M(t) = M_v\, t, \tag{108}$$

with constant loading rate $M_v$, the sheet becomes stretch-free for the imposed displacement and pressure

$$\bar{u}_y(t) = -\left(S - \frac{2}{\kappa_2(t)}\,\sin\left(\frac{S\,\kappa_2(t)}{2}\right)\right), \quad \text{and} \quad p(t) = -\left((c+c_1)\,\kappa_2(t)^3 - c_1\,\kappa_2(t)^2\,\kappa_2^{\text{in}}(t)\right), \tag{109}$$

where $S = \pi$ denotes the length of the sheet in $y$-direction. Equation (108) is a chosen rate that allows for an analytical solution as shown in Appendix B.2. The displacement $\bar{u}_y(t)$ in Equation (109.1) is chosen such that a perfect circular arc is obtained for any given curvature $\kappa_2(t)$. The pressure $p(t)$ in Equation (109.2) is required to equilibrate the structure, and it follows from the well-known formula for thin-walled cylindrical pressure vessels, which requires $p(t) = N_2^2(t)/r(t) = N_2^2(t)\,\kappa_2(t)$, where $N_2^2$ denotes the in-plane stress component in $y$-direction. The derivation of the latter is provided in Appendix B.2. This problem can be solved analytically, which leads to the curvatures

$$\kappa_2^{\text{in}}(t) = \frac{M_v\,\tau_b}{c}\left(e^{-t/\tau_b} + \frac{t}{\tau_b} - 1\right), \tag{110}$$

with the characteristic time

$$\tau_b := \frac{\eta_b\,(c+c_1)}{c\,c_1}, \tag{111}$$

and

$$\kappa_2(t) = \frac{M(t) + c_1\,\kappa_2^{\text{in}}(t)}{c+c_1}, \tag{112}$$

MOST WIEDZY Downloaded from mostwiedzy.pl

see Appendix B.2. The loading rate $M_v$ in Equation (108) is chosen in a way, such that the final curvature is equal to $\kappa_2^{\text{end}} := \kappa_2(t_{\text{end}})$. Using Equations (108) and (110)–(112), this leads to the constant loading rate

$$M_v := \frac{c + c_1}{t_{\text{end}} + \dfrac{c_1\ \tau_b}{c}\ \tilde{\kappa}^{\text{in}}_{2,\text{end}}}, \tag{113}$$

where $\kappa_2^{\text{in}}(t_{\text{end}}) := M_v\ \tilde{\kappa}^{\text{in}}_{2,\text{end}}$ with $\tilde{\kappa}^{\text{in}}_{2,\text{end}} := \tau_b\ \left(\exp(-t_{\text{end}}/\tau_b) + t_{\text{end}}/\tau_b - 1\right)/c$.

First, the convergence with respect to the two relative curvature errors

$$\varepsilon_\kappa := \frac{\left|\kappa_{2,\text{num}}(t_{\text{end}}) - \kappa_{2,\text{ana}}(t_{\text{end}})\right|}{\kappa_{2,\text{ana}}(t_{\text{end}})}, \quad \text{and} \quad \varepsilon^{\text{in}}_\kappa := \frac{\left|\kappa^{\text{in}}_{2,\text{num}}(t_{\text{end}}) - \kappa^{\text{in}}_{2,\text{ana}}(t_{\text{end}})\right|}{\kappa^{\text{in}}_{2,\text{ana}}(t_{\text{end}})}, \tag{114}$$

is investigated. The chosen parameters are $\mu = 10\ L_0^2$, $\Lambda = 5\ L_0^2/c$, $c = c_1$, $\eta_{\text{b}} = 0.5\ c\ T_0$, $t_{\text{end}} = 1\ T_0$, and $\kappa_2^{\text{end}} = 0.5$, such that $\tau_b = 1\ T_0$. Figure 18 shows that the errors converge linearly with an increase of the number of elements and a decrease of the time step size.

Figure 19 shows the deformed surface at various snapshots in time for the parameters $\mu = 10\ L_0^2$, $\Lambda = 5\ L_0^2/c$, $c = c_1$, $\eta_{\text{b}} = 0.5\ c\ T_0$, $t_{\text{end}} = 1\ T_0$, $\kappa_2^{\text{end}} = 1$, and $\tau_b = 1\ T_0$. The surfaces are colored with the relative curvature error $\varepsilon_\kappa$. The maximum error of the surface stretches $|\lambda_1 - 1|$ and $|\lambda_2 - 1|$ over all time steps are of order $\mathcal{O}(10^{-3})$, which indicates that the chosen boundary and loading conditions in Figure 17 work well to obtain stretch-free bending deformations. The relative curvature error is of the same magnitude. At $t = t_{\text{end}}$, the sheet is deformed into a half circle exhibiting large bending deformations. The applied loads over time are visualized in Figure 20 for this example.

Figure 21 shows the total and inelastic curvatures, $\kappa_2$ and $\kappa_2^{\text{in}}$, respectively, over time for different values of $\eta_{\text{b}}$. While the total curvature is not influenced significantly by $\eta_{\text{b}}$, the curvature of the intermediate configuration shows a strong dependency on $\eta_{\text{b}}$. For smaller values of $\eta_{\text{b}}$, the inelastic curvature increases, that is, the intermediate surface is bent more.

## 5.4 | Inflated spherical shell

This section considers a similar example as in Section 5.2, but here, also bending resistance is considered. The setup is the same as in Figure 13 and the parameters $\lambda_{\text{end}} = 4^{1/3}$ and $t_{\text{end}} = 1\ T_0$ are used, see also Equation (101). The final volume is thus four times as large compared to the initial volume, that is, $V(t_{\text{end}}) = 4\ V_0$. The employed thin shell formulation requires $C^1$-continuity of the numerical discretization, such that patch constraints need to be enforced along the marked patch interfaces $\Gamma$ in Figure 13A. A detailed derivation for the enforcement of patch constraints is provided in Paul et al.[12] Here, the Lagrange multiplier method with element-wise constant interpolation is employed to enforce the constraint

$$\boldsymbol{g}_{\text{n}}^{\text{planar}} = \boldsymbol{n} - \tilde{\boldsymbol{n}} = \boldsymbol{0}\,, \quad \forall\, \boldsymbol{x} \in \Gamma, \tag{115}$$

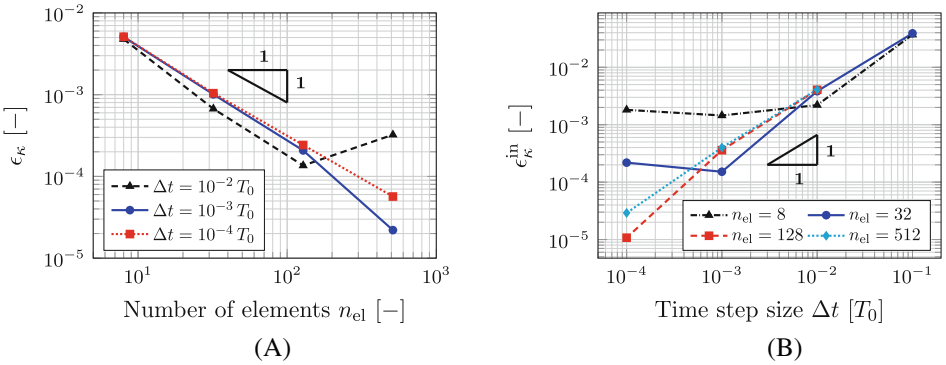


**FIGURE 18** Pure bending of a flat strip: Convergence of the relative curvature errors, see Equation (114), over (A) mesh and (B) time step size refinement

MOST WIEDZY Downloaded from mostwiedzy.pl

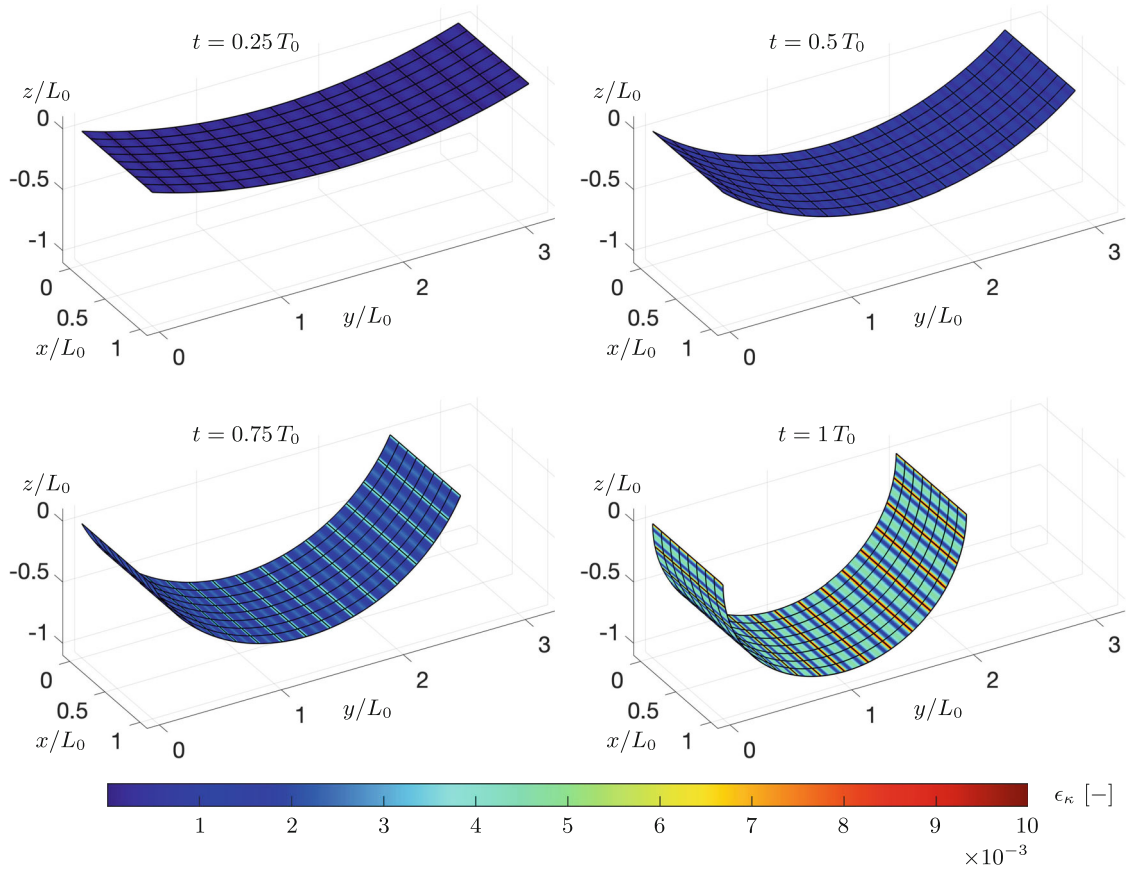


**FIGURE 19** Pure bending of a flat strip: Deformed surfaces at various snapshots in time colored by the relative curvature error $\varepsilon_\kappa$ see Equation (114.1)

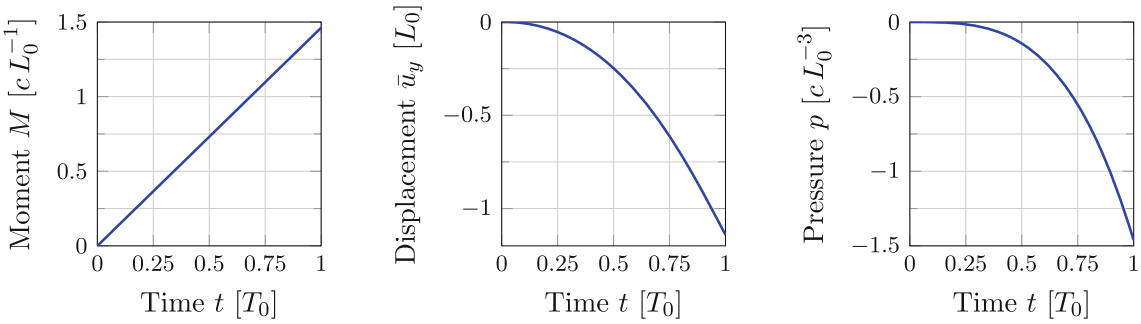


**FIGURE 20** Pure bending of a flat strip: Imposed loads over time, see also Figure 17

along the patch interfaces $\Gamma$. Here, $\boldsymbol{n}$ and $\tilde{\boldsymbol{n}}$ denote the two surface normals of the elements adjacent to $\Gamma$. Further, the symmetry across the gray marked symmetry planes is enforced by the constraint in Equation (115). In that case, $\tilde{\boldsymbol{n}}$ denotes the normal of the symmetry plane.

In the elastic branch, the membrane energy density is given by the incompressible Neo-Hookean material model from Equation (41), and the bending energy density is given by the Helfrich model from Equation (46). For the Maxwell branch, the Neo-Hookean model from Equation (36) with $\Lambda = 0$ and Koiter bending model from Equation (44) are employed.

Similar to Section 5.2, the pressure is composed of two contributions, that is,

$$p(t) = p_{\text{el}}(t) + p_{\text{visc}}(t), \tag{116}$$

MOST WIEDZY Downloaded from mostwiedzy.pl

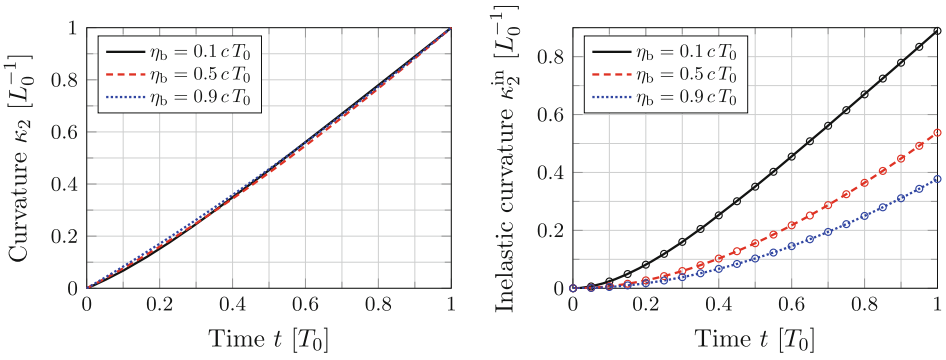


**FIGURE 21** Pure bending of a flat strip: Influence of the parameter $\eta_b$ on the total and inelastic curvatures, $\kappa_2$ and $\kappa_2^{in}$, respectively. The circles mark the numerical results at various snapshots in time, while the lines show the corresponding analytical results. Given $\kappa_2$ and $\kappa_2^{in}$, the elastic curvature follows from $\kappa_2 = \kappa_2^{el} + \kappa_2^{in}$, which is a consequence of Equation (22)

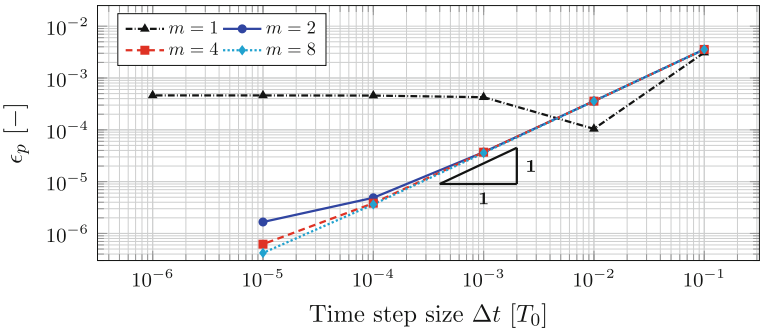


**FIGURE 22** Inflated spherical shell: Convergence of the pressure error $\epsilon_p$, see Equation (107), over time step size refinement

where $p_{el}(t)$ is the pressure function coming from the elastic branch, and $p_{visc}(t)$ is the one from the Maxwell branch. These two contributions $p_\bullet(t)$ are derived in detail in Appendix B.3, and they are given by

$$p_{el}(t) = \frac{2}{R^3}\left[\mu\, R\,\left(\frac{1}{\lambda} - \frac{1}{\lambda^7}\right) + k\,\left(\frac{H_0\, R}{\lambda^2} + \frac{H_0^2\, R^2}{\lambda}\right)\right]. \tag{117}$$

and

$$p_{visc}(t) = \frac{2}{R^3}\left[\mu_1\, R^2\,\left(\frac{1}{\lambda} - \frac{1}{\lambda^3\,\hat{a}_{ev}}\right) + c_1\,\hat{a}_{ev}\,\left(\frac{1}{\lambda} - \frac{\hat{b}_{ev}}{\lambda^2}\right)\right], \tag{118}$$

with $\hat{a}_{ev}(t)$ given in Equation (106) and $\hat{b}_{ev}(t)$ given by

$$\hat{b}_{ev}(t) := \frac{c_1\,\tau_\lambda\,\exp\left(t/\tau_\lambda\right) + \eta_b\,\exp\left(-c_1\,t/\eta_s\right)}{\eta_b + c_1\,\tau_\lambda}. \tag{119}$$

First, the convergence of the model with respect to time step size refinement is investigated. The parameters are $\mu = 5\,k/R^2$, $\mu_1 = \mu$, $c_1 = k$, $k^\star = 0$, $\eta_s = 0.5\,\mu_0\,T_0$, $\eta_b = 0.5\,k\,T_0$, $H_0 = 1/R$, and $t_{end} = 1\,T_0$. Figure 22 shows the convergence of the pressure error $\epsilon_p$, see Equation (107), over the time step size $\Delta t$. As expected for the implicit Euler scheme, the error decreases linearly with decreasing time step size. There is no significant difference between the considered meshes for $m \geq 2$, such that the mesh $m = 2$ is used for the subsequent examples.

For the subsequent results, the parameters as given above are used if not stated otherwise. The time step size is set to $\Delta t = 10^{-3}\,T_0$. Figure 23 shows the resulting pressure over time relation for different values of $\eta_s$ and $\eta_b$, and two different

MOST WIEDZY Downloaded from mostwiedzy.pl

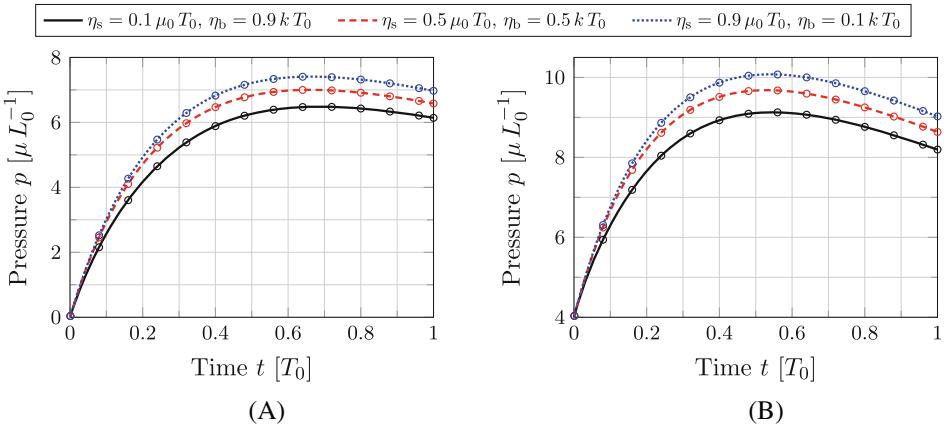


**FIGURE 23** Inflated spherical shell: Influence of the in-plane shear viscosity $\eta_s$ and out-of-plane viscosity $\eta_b$ on the pressure $p$ for two different values of $H_0$. The circles mark the numerical results at various snapshots in time, while the lines show the corresponding analytical results. (A) $H_0 = 0$; (B) $H_0 = 1/R$

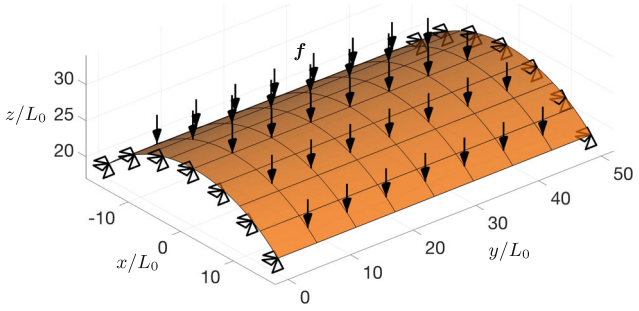


**FIGURE 24** Sagging Scordelis-Lo roof: Geometry, loading, and boundary conditions

values of $H_0 \in \{0, 1/R\}$. With increasing $\eta_s$ and decreasing $\eta_b$, the total pressure increases. Further, the pressure is larger for $H_0 = 1/R$ than for $H_0 = 0$.

## 5.5 | Sagging Scordelis-Lo roof

This section presents a viscoelastic shell that exhibits inhomogeneous deformations. The geometry, loading, and boundary conditions are visualized in Figure 24. The setup corresponds to the Scordelis-Lo roof.[87]

The following time-dependent load is applied

$$\boldsymbol{f}(t) = f_v(t)\begin{bmatrix} 0 \\ 0 \\ -1 \end{bmatrix}, \quad \text{where} \quad f_v(t) := \frac{1}{25}\begin{cases} \dfrac{f_0}{t_0}\,t\,, & t \le t_0 \\ f_0\,, & t > t_0 \end{cases}, \tag{120}$$

with $t_0 = 10\,T_0$ and $f_0 = 1\ \mu_0/L_0$. The Neo-Hookean material model from Equation (38) is used for the membrane response in the elastic and Maxwell branches, and the Koiter model from Equation (44) is employed for the bending response in both branches. For the elastic case, the material parameters $\mu = 10\ \mu_0$, $K = 10\ \mu_0$, $c = 10\ \mu_0\ L_0^2$, and $\mu_1 = K_1 = c_1 = 0$ are used. For the viscoelastic case, the material parameters $\mu = 2\ \mu_0$, $K = 2\ \mu_0$, $c = 2\ \mu_0\ L_0^2$, $\mu_1 = 8\ \mu_0$, $K_1 = 8\ \mu_0$, and $c_1 = 8\ \mu_0\ L_0^2$ are used. Further, $c_0 := \mu_0\ L_0^2$. The finite element mesh is constructed from 8 elements in each direction, the end time is $t_{\text{end}} = 50\,T_0$, and 1000 time steps are used.

The deformed structure is visualized in Figure 25 for the elastic and viscoelastic case using different values for $\eta_s$ and $\eta_b$. As shown, the creep is considerably larger for smaller $\eta_s$ and $\eta_b$.

MOST WIEDZY Downloaded from mostwiedzy.pl

Figure 26 shows the vertical displacement $u_z$ and the surface stretch $J$ over time. There are large creep deformations, which happen faster for smaller values of $\eta_s$ and $\eta_b$. The decomposition of the surface stretch into its inelastic and elastic components, see Equations (19) and (20), is visualized in Figure 27.

In Figure 28, the intermediate mean curvature $\hat{H}$ and mean curvature $H$ are shown over time. The curvature is larger for smaller values of $\eta_s$ and $\eta_b$, which can also be seen in Figure 25, for example, the creep deformations are larger for small $\eta_s$ and $\eta_b$ in the given time span $t \in [0, t_{end}]$.

## 5.6 | Cube encased by a viscoelastic surface

This section highlights that the presented formulation for viscoelastic shells can be applied to model boundary viscoelasticity of 3D bodies without any further modifications. The finite element connectivity automatically enforces the coupling between bulk and surface elements and their constitutive behavior. For this, a cube with side length $2\,L_0$ is encased with a viscoelastic surface. Only one eighth of the geometry is modeled by exploiting the symmetry of the problem and the

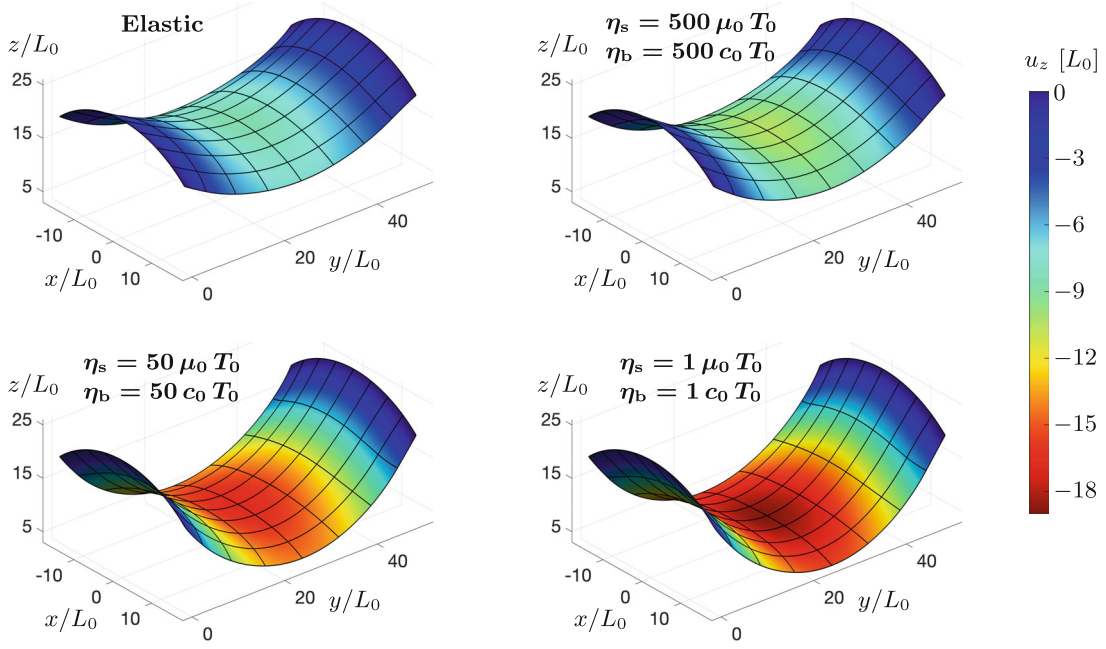


**FIGURE 25** Sagging Scordelis-Lo roof: Final deformation for the elastic and viscoelastic case for three different values of $\eta_s$ and $\eta_b$. The surfaces are colored by the vertical displacement $u_z$

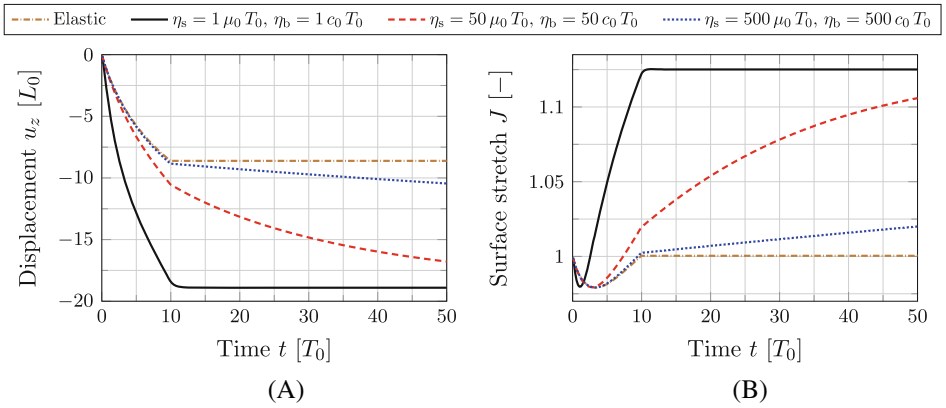


**FIGURE 26** Sagging Scordelis-Lo roof: (A) Vertical displacements and (B) surface stretches for different values of $\eta_s$ and $\eta_b$ over time, measured at the center of the structure

MOST WIEDZY Downloaded from mostwiedzy.pl

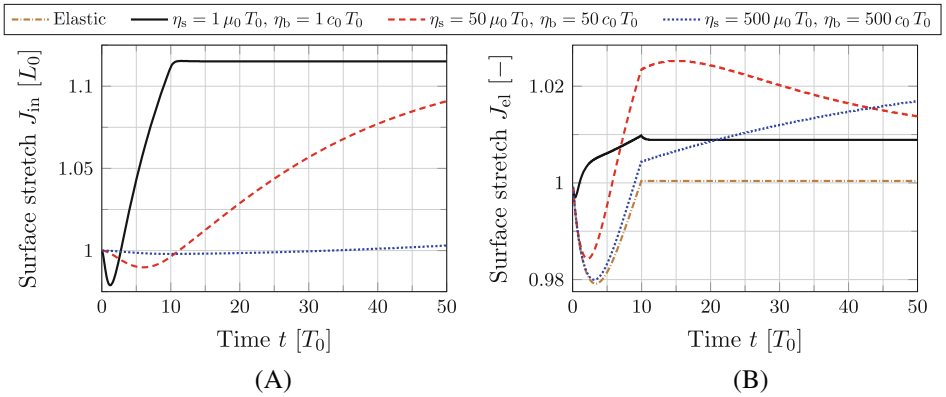


**FIGURE 27** Sagging Scordelis-Lo roof: (A) Inelastic surface stretches $J_{in}$ and (B) elastic surface stretches $J_{el}$ for different values of $\eta_s$ and $\eta_b$ over time, measured at the center of the structure. The total surface stretch, shown in Figure 26B, satisfies $J = J_{in}\,J_{el}$.

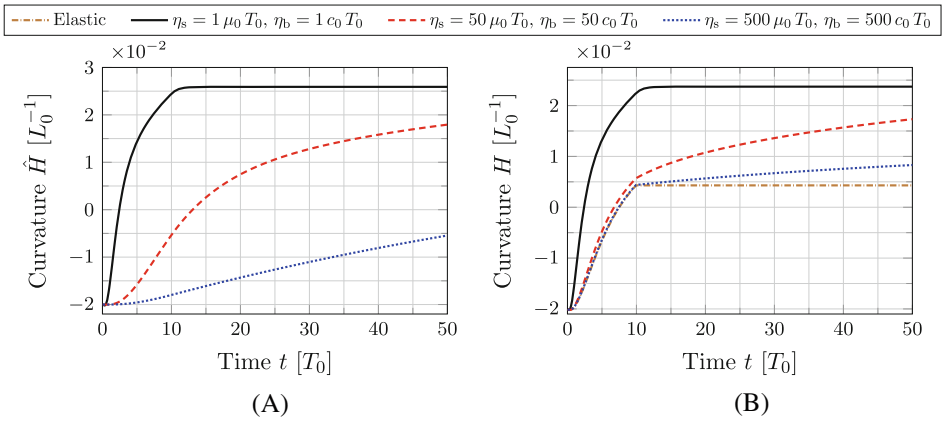


**FIGURE 28** Sagging Scordelis-Lo roof: (A) Intermediate mean curvature $\hat{H}$ and (B) mean curvature $H$ for different values of $\eta_s$ and $\eta_b$ over time, measured at the center of the structure

mesh is *a priori* refined towards the sharp edges, see Figure 29. A similar example is considered by Dortdivanlioglu and Javili.[75] In total, 512 hexahedral elements and 192 quadrilateral elements are used to discretize the eighth cube and its encasing surface, respectively. Both are discretized by quadratic NURBS shape functions. The material behavior of the bulk material is modeled by a Neo-Hookean material model with elastic energy density and stresses

$$\tilde{\Psi} = \frac{\tilde{\Lambda}}{2}\left(\ln\tilde{J}\right)^2 + \frac{\tilde{\mu}}{2}\left(\tilde{I}_1 - 3 - 2\,\ln\tilde{J}\right), \quad \text{and} \quad \tilde{\boldsymbol{\sigma}} = \frac{\tilde{\Lambda}}{\tilde{J}}\,\ln\tilde{J} + \frac{\tilde{\mu}}{\tilde{J}}\left(\tilde{\boldsymbol{B}} + \tilde{\boldsymbol{I}}\right). \tag{121}$$

Here, $\tilde{\boldsymbol{I}}$ is the full identity in 3D, $\tilde{\boldsymbol{B}}$ is the left Cauchy–Green tensor in 3D, and $\tilde{I}_1$ and $\tilde{J}$ are the invariants of $\tilde{\boldsymbol{B}}$. A tilde is added to avoid confusion with the corresponding surface quantities presented in Section 2.2. The material parameters for the bulk are $\tilde{\Lambda} = 5\ \tilde{\Lambda}_0$ and $\tilde{\mu} = 5\ \tilde{\Lambda}_0$. The elastic energy density in the elastic branch is given by Equation (42) with prescribed surface tension $\gamma$. Since this model provides no deviatoric surface stiffness, the second part of Equation (38) with $\mu = 1\ \tilde{\Lambda}_0\ L_0$ is added for numerical stabilization. For the Maxwell branch, the spring element from Figure 2 is omitted, such that the constitutive model resembles a Kelvin model with $\hat{a}_{\alpha\beta} = a_{\alpha\beta}$, $J_{in} = J$, and $J_{el} = 1$. The dashpot is chosen to follow model (52), which in this special case is a pure dilatational model that requires no evolution laws and can be directly computed using $\dot{J} \approx (J - J_n)/\Delta t$, where $J_n$ denotes the surface stretch from the previous time step. The surface tension is imposed over time as

$$\gamma(t) = \gamma_0 \begin{cases} t/(2.5\ T_0)\,, & t \le 2.5\ T_0 \\ 1\,, & t > 2.5\ T_0 \end{cases}. \tag{122}$$

The end time is $t_{end} = 10\ T_0$ and 2500 time steps are used for the temporal integration.

MOST WIEDZY Downloaded from mostwiedzy.pl

Figure 29 shows the deformed geometry at $t_{\text{end}}$ for different values of $\gamma_0$ and fixed $\eta_s = 1\ \tilde{\Lambda}_0\ L_0\ T_0$. Energetically, a sphere is the optimal geometry for constant surface tension. Thus, for larger prescribed surface tension, the bulk deforms more into a spherical shape. Due to the stiffness of the bulk material, not a perfect sphere is obtained, but the sharp edges and corners are smoothed out.

The displacement norm $\|\boldsymbol{u}\|_2 = \|\boldsymbol{x} - \boldsymbol{X}\|_2$ over time is plotted in Figure 30A for different values of the in-plane shear viscosity $\eta_s$ and fixed $\gamma_0 = 5\ \tilde{\Lambda}_0\ L_0$, and in Figure 30B for different values of the surface tension $\gamma_0$ and fixed $\eta_s = 1\ \tilde{\Lambda}_0\ L_0\ T_0$.

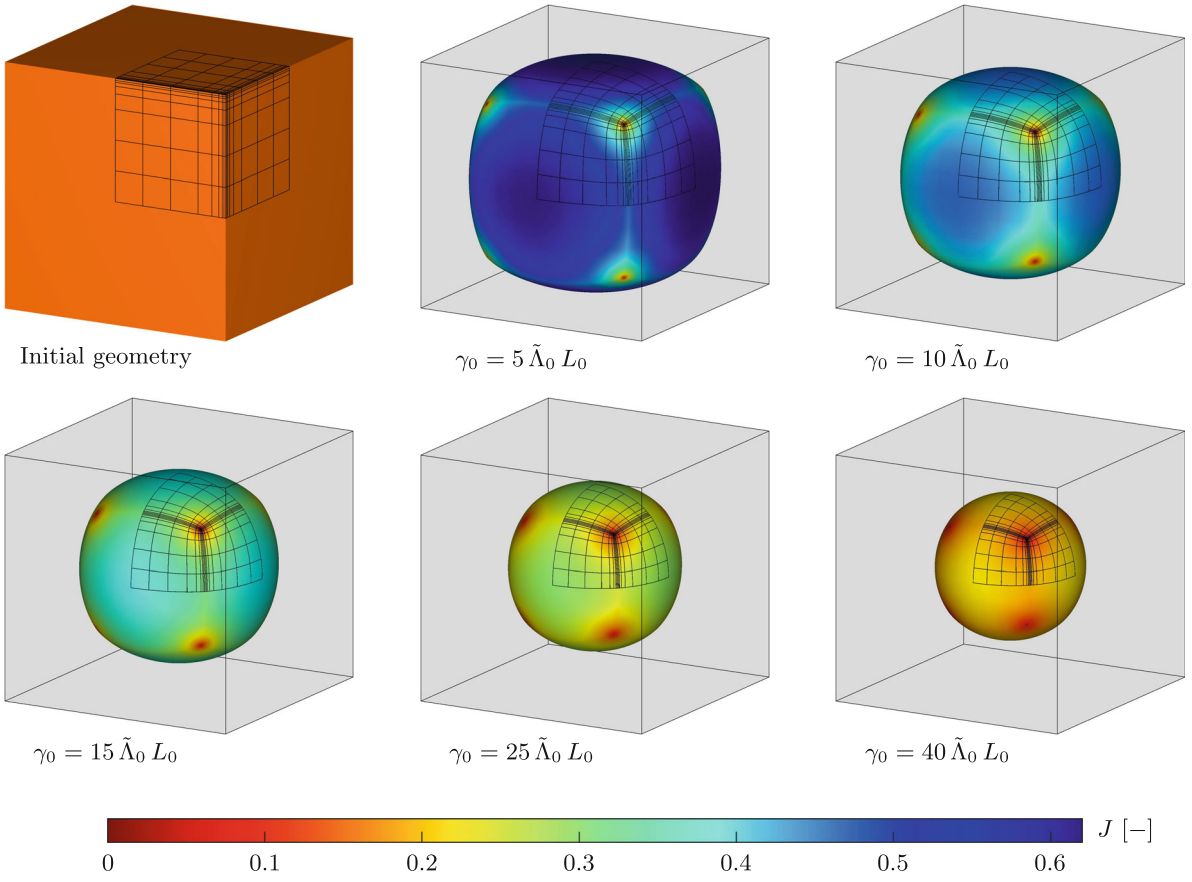


**FIGURE 29** Cube encased by a viscoelastic surface: Deformed cubes at $t_{\text{end}}$ for different values of the imposed surface tension $\gamma_0$, colored by the surface stretch $J$, see Equation (9.2)

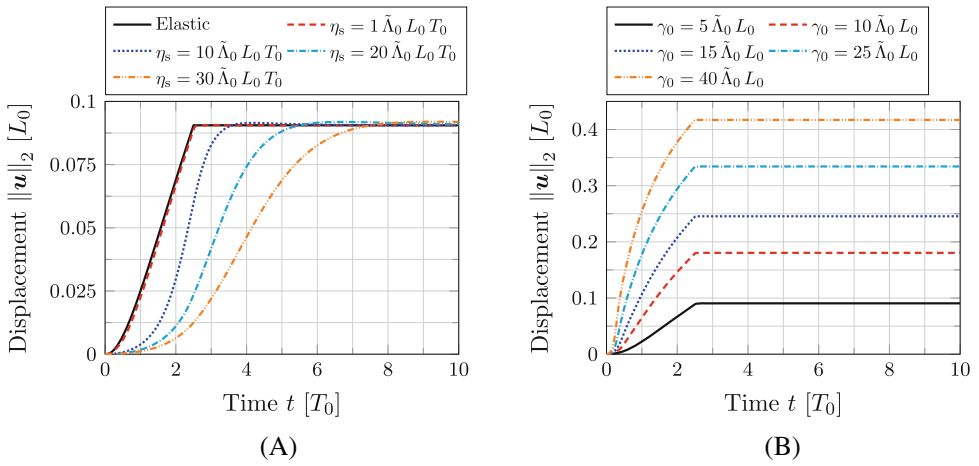


**FIGURE 30** Cube encased by a viscoelastic surface: Displacement norm $\|\boldsymbol{u}\|_2$ for different values of the in-plane shear viscosity $\eta_s$ and surface tension $\gamma_0$, measured at the central point of the top surface. (A) Influence of $\eta_s$ for $\gamma_0 = 5\ \tilde{\Lambda}_0\ L_0$; (B) Influence of $\gamma_0$ for $\eta_s = 1\ \tilde{\Lambda}_0\ L_0\ T_0$

MOST WIEDZY Downloaded from mostwiedzy.pl

Figure 30A shows creep behavior, which becomes more pronounced for increasing $\eta_s$. Figure 30B shows that larger values of the surface tension lead to larger deformations, see also Figure 29.

## 6 | CONCLUSION

This work presents a computational formulation to model isotropic finite strain viscoelasticity for membranes, thin shells, and boundaries of 3D bodies. The material behavior is modeled based on the generalized viscoelastic solid, for which a multiplicative split of the surface deformation gradient is employed. The implementation of membrane and bending viscosity is verified by several numerical examples and ideal convergence rates are obtained in all cases. The chosen examples capture large deformations and standard viscoelasticity behavior of thin shells, as well as boundary viscoelasticity of 3D bodies.

This work demonstrates that the previously developed multiplicative split of the surface deformation gradient works robustly and accurately in finite strain computations. The employed direct surface formulation and its decomposition of the elastic energy density into membrane and bending parts makes the constitutive modeling more flexible. For example, one can consider viscous material behavior only for membrane deformations but not for bending, or vice versa. At the same time, the formulation allows to use known 3D material models. The presented formulation also allows to describe boundary viscoelasticity of 3D bodies. Thus, the proposed formulation unifies boundary, membrane and shell viscoelasticity. The use of rotation-free finite elements and isogeometric shape functions increases efficiency and accuracy in comparison to classical FE discretizations. This increase is greatest when used in conjunction with direct surface-based constitutive models such as are provided here.

In order to avoid problems stemming from ill-conditioned parametrizations noted in Remark 7, the ODEs for $\hat{a}^{\alpha\beta}$ can be reformulated, for example, as ODEs for $I_1^{\text{el}}$, $J_{\text{in}}$, and $J_{\text{el}}$. Also, constant area for the inelastic deformation can be enforced by coupling the evolution laws to the constraint $J_{\text{in}} = 1$, which can be directly plugged into the ODEs to eliminate one of them, or enforced by a Lagrange multiplier approach, for instance.

As the viscoelastic framework introduces a time scale, the quasi-static shell framework can also be extended to incorporate inertia, for example, to investigate the influence of the viscous effects and inertia on each other. Further, temperature can be introduced in the formulation in order to model the change of temperature as a cause of dissipation. The elastic and viscoelastic material properties can then also be dependent on the temperature.

### ACKNOWLEDGMENTS

The authors acknowledge funding by the Deutsche Forschungsgemeinschaft (DFG, German Research Foundation) – 333849990/GRK2379 (IRTG Modern Inverse Problems). Simulations were partly performed with computing resources granted by RWTH Aachen University under project rwth0917. Open Access funding enabled and organized by Projekt DEAL.

### DATA AVAILABILITY STATEMENT

The data that support the findings of this study are available from the corresponding author upon reasonable request.

### ENDNOTES

*A tilde is placed on the current thickness to distinguish it from the time $t$.

†As the elastic and inelastic stresses are equal in the Maxwell model, the indices "(el)" and "(in)" can be omitted. But they are kept here in order to emphasize that these are the stresses in the spring and dashpot elements.

‡Here, the brackets in the index are used in order to distinguish the moments in the elastic branch, $M^{\alpha\beta}_{(0)}$, from the moments components w.r.t. the reference configuration, $M^{\alpha\beta}_0$, see also Equation (28.2).

§with $A_{\alpha\beta}$ replaced by $\hat{a}_{\alpha\beta}$, see also Remark 4

¶with $B_{\alpha\beta}$ replaced by $\hat{b}_{\alpha\beta}$, see also Remark 4

#$\sigma^{\alpha}_{\beta} = \sigma^{\alpha\gamma} a_{\gamma\beta}$

‖According to thin shell theory, there is a high-order coupling between curvatures and stretches; see, for example, Sauer and Duong.[79]

**with the modifications mentioned in Remark 4

### ORCID

*Roger A. Sauer* https://orcid.org/0000-0001-5625-8295

MOST WIEDZY Downloaded from mostwiedzy.pl

## REFERENCES


1. Hughes TJR, Cottrell JA, Bazilevs Y. Isogeometric analysis: CAD, finite elements, NURBS, exact geometry and mesh refinement. *Comput Methods Appl Mech Eng*. 2005;194(39–41):4135-4195. doi:10.1016/j.cma.2004.10.008
2. Cottrell J, Hughes T, Bazilevs Y. *Isogeometric Analysis: Toward integration of CAD and FEA*. Wiley; 2009.
3. Evans JA, Bazilevs Y, Babuška I, Hughes TJ. n-Widths, sup–infs, and optimality ratios for the K-version of the isogeometric finite element method. *Comput Methods Appl Mech Eng*. 2009;198(21):1726-1741. doi:10.1016/j.cma.2009.01.021
4. Borden MJ, Scott MA, Evans JA, Hughes TJR. Isogeometric finite element data structures based on Bézier extraction of NURBS. *Int J Numer Methods Eng*. 2011;87(1–5):15-47. doi:10.1002/nme.2968
5. Schillinger D, Ruthala PK, Nguyen LH. Lagrange extraction and projection for NURBS basis functions: a direct link between isogeometric and standard nodal finite element formulations. *Int J Numer Methods Eng*. 2016;108(6):515-534. doi:10.1002/nme.5216
6. Nguyen VP, Anitescu C, Bordas SP, Rabczuk T. Isogeometric analysis: an overview and computer implementation aspects. *Math Comput Simul*. 2015;117:89-116. doi:10.1016/j.matcom.2015.05.008
7. Kiendl J, Bletzinger KU, Linhard J, Wüchner R. Isogeometric shell analysis with Kirchhoff-Love elements. *Comput Methods Appl Mech Eng*. 2009;198:3902-3914. doi:10.1016/j.cma.2009.08.013
8. Benson DJ, Hartmann S, Bazilevs Y, Hsu MC, Hughes TJR. Blended isogeometric shells. *Comput Methods Appl Mech Eng*. 2013;255:133-146. doi:10.1016/j.cma.2012.11.020
9. Echter R, Oesterle B, Bischoff M. A hierarchic family of isogeometric shell finite elements. *Comput Methods Appl Mech Eng*. 2013;254:170-180. doi:10.1016/j.cma.2012.10.018
10. Kiendl J, Hsu MC, Wu MC, Reali A. Isogeometric Kirchhoff–Love shell formulations for general hyperelastic materials. *Comput Methods Appl Mech Eng*. 2015;291:280-303. doi:10.1016/j.cma.2015.03.010
11. Duong TX, Roohbakhshan F, Sauer RA. A new rotation-free isogeometric thin shell formulation and a corresponding continuity constraint for patch boundaries. *Comput Methods Appl Mech Eng*. 2017;316:43-83. doi:10.1016/j.cma.2016.04.008
12. Paul K, Zimmermann C, Duong TX, Sauer RA. Isogeometric continuity constraints for multi-patch shells governed by fourth-order deformation and phase field models. *Comput Methods Appl Mech Eng*. 2020;370:113219. doi:10.1016/j.cma.2020.113219
13. Thai CH, Nguyen-Xuan H, Nguyen-Thanh N, Le TH, Nguyen-Thoi T, Rabczuk T. Static, free vibration, and buckling analysis of laminated composite Reissner–Mindlin plates using NURBS-based isogeometric approach. *Int J Numer Methods Eng*. 2012;91(6):571-603. doi:10.1002/nme.4282
14. Deng X, Korobenko A, Yan J, Bazilevs Y. Isogeometric analysis of continuum damage in rotation-free composite shells. *Comput Methods Appl Mech Eng*. 2015;284:349-372. doi:10.1016/j.cma.2014.09.015
15. Nagy AP, IJsselmuiden ST, Abdalla MM. Isogeometric design of anisotropic shells: optimal form and material distribution. *Comput Methods Appl Mech Eng*. 2013;264:145-162. doi:10.1016/j.cma.2013.05.019
16. Faroughi S, Shafei E, Rabczuk T. Anisotropic solid-like shells modeled with NURBS-based isogeometric approach: vibration, buckling, and divergence analyses. *Comput Methods Appl Mech Eng*. 2020;359:112668. doi:10.1016/j.cma.2019.112668
17. Kiendl J, Schmidt R, Wüchner R, Bletzinger KU. Isogeometric shape optimization of shells using semi-analytical sensitivity analysis and sensitivity weighting. *Comput Methods Appl Mech Eng*. 2014;274:148-167. doi:10.1016/j.cma.2014.02.001
18. Hirschler T, Bouclier R, Duval A, Elguedj T, Morlier J. The embedded isogeometric Kirchhoff–Love shell: from design to shape optimization of non-conforming stiffened multipatch structures. *Comput Methods Appl Mech Eng*. 2019;349:774-797. doi:10.1016/j.cma.2019.02.042
19. Sauer RA. Stabilized finite element formulations for liquid membranes and their application to droplet contact. *Int J Numer Methods Fluids*. 2014;75(7):519-545.
20. Roohbakhshan F, Sauer RA. A finite membrane element formulation for surfactants. *Colloids Surf A Physicochem Eng Asp*. 2019;566:84-103. doi:10.1016/j.colsurfa.2018.11.022
21. Tepole AB, Kabaria H, Bletzinger KU, Kuhl E. Isogeometric Kirchhoff–Love shell formulations for biological membranes. *Comput Methods Appl Mech Eng*. 2015;293:328-347. doi:10.1016/j.cma.2015.05.006
22. Roohbakhshan F, Sauer RA. Efficient isogeometric thin shell formulations for soft biological materials. *Biomech Model Mechanobiol*. 2017;16(5):1569-1597. doi:10.1007/s10237-017-0906-6
23. Kang P, Youn SK. Isogeometric topology optimization of shell structures using trimmed NURBS surfaces. *Finite Elem Anal Des*. 2016;120:18-40. doi:10.1016/j.finel.2016.06.003
24. Zhang W, Li D, Kang P, Guo X, Youn SK. Explicit topology optimization using IGA-based moving morphable void (MMV) approach. *Comput Methods Appl Mech Eng*. 2020;360:112685. doi:10.1016/j.cma.2019.112685
25. Ambati M, De Lorenzis L. Phase-field modeling of brittle and ductile fracture in shells with isogeometric NURBS-based solid-shell elements. *Comput Methods Appl Mech Eng*. 2016;312:351-373. doi:10.1016/j.cma.2016.02.017
26. Kiendl J, Ambati M, De Lorenzis L, Gomez H, Reali A. Phase-field description of brittle fracture in plates and shells. *Comput Methods Appl Mech Eng*. 2016;312:374-394. doi:10.1016/j.cma.2016.09.011
27. Sauer RA, Duong TX, Mandadapu KK, Steigmann DJ. A stabilized finite element formulation for liquid shells and its application to lipid bilayers. *J Comput Phys*. 2017;330:436-466. doi:10.1016/j.jcp.2016.11.004
28. Bartezzaghi A, Dedè L, Quarteroni A. Biomembrane modeling with isogeometric analysis. *Comput Methods Appl Mech Eng*. 2019;347:103-119. doi:10.1016/j.cma.2018.12.025
29. Ghaffari R, Duong TX, Sauer RA. A new shell formulation for graphene structures based on existing ab-initio data. *Int J Solids Struct*. 2018;135:37-60. doi:10.1016/j.ijsolstr.2017.11.008


MOST WIEDZY Downloaded from mostwiedzy.pl

30. Ghaffari R, Shirazian F, Hu M, Sauer RA. A nonlinear hyperelasticity model for single layer blue phosphorus based on ab initio calculations. *Proc Royal Soc A Math Phys Eng Sci*. 2019;475(2229):20190149. doi:10.1098/rspa.2019.0149
31. Ambati M, Kiendl J, De Lorenzis L. Isogeometric Kirchhoff–Love shell formulation for elasto-plasticity. *Comput Methods Appl Mech Eng*. 2018;340:320-339. doi:10.1016/j.cma.2018.05.023
32. Huynh G, Zhuang X, Bui H, Meschke G, Nguyen-Xuan H. Elasto-plastic large deformation analysis of multi-patch thin shells by isogeometric approach. *Finite Elem Anal Des*. 2020;173:103389. doi:10.1016/j.finel.2020.103389
33. Vu-Bac N, Duong T, Lahmer T, et al. A NURBS-based inverse analysis for reconstruction of nonlinear deformations of thin shell structures. *Comput Methods Appl Mech Eng*. 2018;331:427-455. doi:10.1016/j.cma.2017.09.034
34. Borzeszkowski B, Lubowiecka I, Sauer RA. Nonlinear material identification of heterogeneous isogeometric Kirchhoff–Love shells. *Comput Methods Appl Mech Eng*. 2022;390:114442. doi:10.1016/j.cma.2021.114442
35. Valizadeh N, Rabczuk T. Isogeometric analysis for phase-field models of geometric PDEs and high-order PDEs on stationary and evolving surfaces. *Comput Methods Appl Mech Eng*. 2019;351:599-642. doi:10.1016/j.cma.2019.03.043
36. Zimmermann C, Toshniwal D, Landis CM, Hughes TJR, Mandadapu KK, Sauer RA. An isogeometric finite element formulation for phase transitions on deforming surfaces. *Comput Methods Appl Mech Eng*. 2019;351:441-477. doi:10.1016/j.cma.2019.03.022
37. Paul K, Zimmermann C, Mandadapu KK, Hughes TJR, Landis CM, Sauer RA. An adaptive space-time phase field formulation for dynamic fracture of brittle shells based on LR NURBS. *Comput Mech*. 2020;65:1039-1062. doi:10.1007/s00466-019-01807-y
38. Proserpio D, Ambati M, De Lorenzis L, Kiendl J. A framework for efficient isogeometric computations of phase-field brittle fracture in multipatch shell structures. *Comput Methods Appl Mech Eng*. 2020;372:113363. doi:10.1016/j.cma.2020.113363
39. Schulte J, Dittmann M, Eugster S, et al. Isogeometric analysis of fiber reinforced composites using Kirchhoff–Love shell elements. *Comput Methods Appl Mech Eng*. 2020;362:112845. doi:10.1016/j.cma.2020.112845
40. Duong TX, Itskov M, Sauer RA. A general isogeometric finite element formulation for rotation-free shells with in-plane bending of embedded fibers. *Int J Numer Methods Eng*. 2022;123(14):3115-3147. doi:10.1002/nme.6937
41. Coleman BD, Noll W. Foundations of linear viscoelasticity. *Rev Mod Phys*. 1961;33:239-249. doi:10.1103/RevModPhys.33.239
42. Crochet M, Naghdi P. A class of simple solids with fading memory. *Int J Eng Sci*. 1969;7(12):1173-1198. doi:10.1016/0020-7225(69)90028-7
43. Koh S, Eringen A. On the foundations of non-linear thermo-viscoelasticity. *Int J Eng Sci*. 1963;1(2):199-229. doi:10.1016/0020-7225(63)90034-X
44. Sidoroff F. Nonlinear viscoelastic model with an intermediate configuration. [Un Modele Viscoelastique Non Lineaire Avec Configuration Intermediaire.]. *J Mecan*. 1974;13(4):679-713.
45. Simo J. On a fully three-dimensional finite-strain viscoelastic damage model: formulation and computational aspects. *Comput Methods Appl Mech Eng*. 1987;60(2):153-173. doi:10.1016/0045-7825(87)90107-1
46. Govindjee S, Simo JC. Mullins' effect and the strain amplitude dependence of the storage modulus. *Int J Solids Struct*. 1992;29(14):1737-1751. doi:10.1016/0020-7683(92)90167-R
47. Reese S, Govindjee S. A theory of finite viscoelasticity and numerical aspects. *Int J Solids Struct*. 1998;35(26):3455-3482. doi:10.1016/S0020-7683(97)00217-5
48. Lubarda V. Constitutive theories based on the multiplicative decomposition of deformation gradient: thermoelasticity, elastoplasticity, and biomechanics. *Appl Mech Rev*. 2004;57(1–6):95-108. doi:10.1115/1.1591000
49. Gupta A, Steigmann DJ, Stölken JS. On the evolution of plasticity and incompatibility. *Math Mech Solids*. 2007;12(6):583-610. doi:10.1177/1081286506064721
50. Reina C, Fokoua Djodom L, Ortiz M, Conti S. Kinematics of elasto-plasticity: validity and limits of applicability of F=FeFp for general three-dimensional deformations. *J Mech Phys Solids*. 2018;121:99-113. doi:10.1016/j.jmps.2018.07.006
51. Shaw S, Johnson A, Whiteman J. Modelling and finite element analysis of applied polymer viscoelasticity problems. *Math Finite Elem Appl*. 1999;10:63-86.
52. Miehe C, Keck J. Superimposed finite elastic–viscoelastic–plastoelastic stress response with damage in filled rubbery polymers. Experiments, modelling and algorithmic implementation. *J Mech Phys Solids*. 2000;48(2):323-365. doi:10.1016/S0022-5096(99)00017-4
53. Holzapfel GA, Gasser TC. A viscoelastic model for fiber-reinforced composites at finite strains: continuum basis, computational aspects and applications. *Comput Methods Appl Mech Eng*. 2001;190(34):4379-4403. doi:10.1016/S0045-7825(00)00323-6
54. Bonet J. Large strain viscoelastic constitutive models. *Int J Solids Struct*. 2001;38(17):2953-2968. doi:10.1016/S0020-7683(00)00215-8
55. Adolfsson K, Enelund M. Fractional derivative viscoelasticity at large deformations. *Nonlinear Dyn*. 2003;33:301-321. doi:10.1023/A:1026003130033
56. Fancello E, Ponthot JP, Stainier L. A variational formulation of constitutive models and updates in non-linear finite viscoelasticity. *Int J Numer Methods Eng*. 2006;65:1831-1864. doi:10.1002/nme.1525
57. Amin A, Lion A, Sekita S, Okui Y. Nonlinear dependence of viscosity in modeling the rate-dependent response of natural and high damping rubbers in compression and shear: experimental identification and numerical verification. *Int J Plast*. 2006;22(9):1610-1657. doi:10.1016/j.ijplas.2005.09.005
58. Hossain M, Possart G, Steinmann P. A finite strain framework for the simulation of polymer curing. Part II. Viscoelasticity and shrinkage. *Comput Mech*. 2010;46:363-375. doi:10.1007/s00466-010-0479-z
59. Kästner M, Obst M, Brummund J, Thielsch K, Ulbricht V. Inelastic material behavior of polymers – Experimental characterization, formulation and implementation of a material model. *Mech Mater*. 2012;52:40-57. doi:10.1016/j.mechmat.2012.04.011
60. Marques SP, Creus GJ. *Computational Viscoelasticity*. Springer Science & Business Media; 2012.


MOST WIEDZY Downloaded from mostwiedzy.pl

61. Shutov A, Landgraf R, Ihlemann J. An explicit solution for implicit time stepping in multiplicative finite strain viscoelasticity. *Comput Methods Appl Mech Eng*. 2013;265:213-225. doi:10.1016/j.cma.2013.07.004
62. James KA, Waisman H. On the importance of viscoelastic response consideration in structural design optimization. *Optim Eng*. 2016;17:631-650. doi:10.1007/s11081-016-9327-0
63. Evans E, Hochmuth R. Membrane viscoelasticity. *Biophys J*. 1976;16:1-11. doi:10.1016/S0006-3495(76)85658-5
64. Neff P. A geometrically exact viscoplastic membrane-shell with viscoelastic transverse shear resistance avoiding degeneracy in the thin-shell limit. *Z Angew Math Phys*. 2005;56:148-182. doi:10.1007/s00033-004-4065-0
65. Sauer RA, Ghaffari R, Gupta A. The multiplicative deformation split for shells with application to growth, chemical swelling, thermoelasticity, viscoelasticity and elastoplasticity. *Int J Solids Struct*. 2019;174-175:53-68. doi:10.1016/j.ijsolstr.2019.06.002
66. Lubarda V. Rate-type elasticity and viscoelasticity of an erythrocyte membrane. *J Mech Mater Struct*. 2011;6(1–4):361-376. doi:10.2140/jomms.2011.6.361
67. Li F. A justification of two-dimensional nonlinear viscoelastic shells model. *Abstr Appl Anal*. 2012;2012:1-24. doi:10.1155/2012/287865
68. Altenbach H, Eremeyev V. On the constitutive equations of viscoelastic micropolar plates and shells of differential type. *Math Mech Complex Syst*. 2015;3(3):273-283. doi:10.2140/memocs.2015.3.273
69. Dörr D, Schirmaier FJ, Henning F, Kärger L. A viscoelastic approach for modeling bending behavior in finite element forming simulation of continuously fiber reinforced composites. *Compos A Appl Sci Manuf*. 2017;94:113-123. doi:10.1016/j.compositesa.2016.11.027
70. Liu L, Yu M, Lin H, Foty R. Deformation and relaxation of an incompressible viscoelastic body with surface viscoelasticity. *J Mech Phys Solids*. 2017;98:309-329. doi:10.1016/j.jmps.2016.09.013
71. Hernandez E, Naranjo C, Vellojin J. Modelling of thin viscoelastic shell structures under Reissner–Mindlin kinematic assumption. *Appl Math Model*. 2020;79:180-199. doi:10.1016/j.apm.2019.10.031
72. Dadgar-Rad F, Firouzi N. Time-dependent response of incompressible membranes based on quasi-linear viscoelasticity theory. *Int J Appl Mech*. 2021;13(3):2150036. doi:10.1142/S1758825121500368
73. Javili A, Steinmann P. A finite element framework for continua with boundary energies. Part I: the two-dimensional case. *Comput Methods Appl Mech Eng*. 2009;198(27):2198-2208. doi:10.1016/j.cma.2009.02.008
74. Javili A, Steinmann P. A finite element framework for continua with boundary energies. Part II: the three-dimensional case. *Comput Methods Appl Mech Eng*. 2010;199(9):755-765. doi:10.1016/j.cma.2009.11.003
75. Dortdivanlioglu B, Javili A. Boundary viscoelasticity theory at finite deformations and computational implementation using isogeometric analysis. *Comput Methods Appl Mech Eng*. 2021;374:113579. doi:10.1016/j.cma.2020.113579
76. Shafei E, Faroughi S, Rabczuk T. Nonlinear transient vibration of viscoelastic plates: a NURBS-based isogeometric HSDT approach. *Comput Math Appl*. 2021;84:1-15. doi:10.1016/j.camwa.2020.12.006
77. Sun D, Dai R, Liu X, Zhan Y, Dong C. RI-IGABEM for 2D viscoelastic problems and its application to solid propellant grains. *Comput Methods Appl Mech Eng*. 2021;378:113737. doi:10.1016/j.cma.2021.113737
78. Sauer RA. On the computational modeling of lipid bilayers using thin-shell theory. In: Steigmann DJ, ed. *The Role of Mechanics in the Study of Lipid Bilayers*. Springer International Publishing; 2018:221-286.
79. Sauer RA, Duong TX. On the theoretical foundations of thin solid and liquid shells. *Math Mech Solids*. 2017;22(3):343-371. doi:10.1177/1081286515594656
80. Simo J, Fox D. On a stress resultant geometrically exact shell model. Part I: Formulation and optimal parametrization. *Comput Methods Appl Mech Eng*. 1989;72(3):267-304. doi:10.1016/0045-7825(89)90002-9
81. Ciarlet PG. An introduction to differential geometry with applications to elasticity. *J Elast*. 2005;78(1):1-215.
82. Ogden RW. *Non-Linear Elastic Deformations*. Courier Corporation; 1997.
83. Sauer RA, Duong TX, Corbett CJ. A computational formulation for constrained solid and liquid membranes considering isogeometric finite elements. *Comput Methods Appl Mech Eng*. 2014;271:48-68. doi:10.1016/j.cma.2013.11.025
84. Sauer RA. A contact theory for surface tension driven systems. *Math Mech Solids*. 2016;21(3):305-325. doi:10.1177/1081286514521230
85. Helfrich W. Elastic properties of lipid bilayers: theory and possible experiments. *Z Naturforsch C*. 1973;28(11–12):693-703. doi:10.1515/znc-1973-11-1209
86. Toshniwal D, Speleers H, Hughes TJ. Smooth cubic spline spaces on unstructured quadrilateral meshes with particular emphasis on extraordinary points: geometric design and isogeometric analysis considerations. *Comput Methods Appl Mech Eng*. 2017;327:411-458. doi:10.1016/j.cma.2017.06.008
87. Macneal RH, Harder RL. A proposed standard set of problems to test finite element accuracy. Finite Elements in Analysis and Design. 1985;1(1):3-20. doi:10.1016/0168-874x(85)90003-4
88. Needleman A. Inflation of spherical rubber balloons. *Int J Solids Struct*. 1977;13(5):409-421. doi:10.1016/0020-7683(77)90036-1


**How to cite this article:** Paul K, Sauer RA. An isogeometric finite element formulation for boundary and shell viscoelasticity based on a multiplicative surface deformation split. *Int J Numer Methods Eng*. 2022;123(22):5570-5617. doi: 10.1002/nme.7080

MOST WIEDZY Downloaded from mostwiedzy.pl

## APPENDIX A. LINEARIZATION

### A.1 Auxiliary derivatives

For the linearization in Appendix A.2, the derivatives of Equations (20.1), (21), and (24.1) w.r.t. $\hat{a}^{\alpha\beta}$ and $\hat{b}_{\alpha\beta}$ are required. They are given by

$$\frac{\partial I_1^{\mathrm{el}}}{\partial \hat{a}^{\alpha\beta}} = a_{\alpha\beta} \ , \quad \frac{\partial J_{\mathrm{el}}}{\partial \hat{a}^{\alpha\beta}} = \frac{1}{2}\, J_{\mathrm{el}}\, \hat{a}_{\alpha\beta} \ , \quad \frac{\partial \hat{H}}{\partial \hat{a}^{\alpha\beta}} = \frac{1}{2}\, \hat{b}_{\alpha\beta} \ , \quad \text{and} \quad \frac{\partial \hat{H}}{\partial \hat{b}_{\alpha\beta}} = \frac{1}{2}\, \hat{a}^{\alpha\beta}, \tag{A1}$$

where $\partial \left(\det[\hat{a}^{\alpha\beta}]\right) / \partial t = \det[\hat{a}^{\alpha\beta}]\, \hat{a}_{\gamma\delta}\, \dot{\hat{a}}^{\gamma\delta}$ has been used.

For the linearization of the stresses in the Maxwell branch, see Appendix A.3, the derivatives of $J_{\mathrm{el}}$, $J_{\mathrm{in}}$, and $I_1^{\mathrm{el}}$ w.r.t. $a_{\gamma\delta}$ are required, see Equations (20) and (21). They are given by

$$\frac{\partial I_1^{\mathrm{el}}}{\partial a_{\gamma\delta}} = \hat{a}^{\gamma\delta} + \frac{\partial \hat{a}^{\varepsilon\zeta}}{\partial a_{\gamma\delta}}\, a_{\varepsilon\zeta} \ , \tag{A2}$$

and

$$\begin{aligned} \frac{\partial J_{\mathrm{in}}}{\partial a_{\gamma\delta}} = \frac{\partial J_{\mathrm{in}}}{\partial \hat{a}^{\varepsilon\zeta}}\, \frac{\partial \hat{a}^{\varepsilon\zeta}}{\partial a_{\gamma\delta}} &= \frac{1}{\sqrt{\det[A_{\alpha\beta}]}}\, \frac{\partial}{\partial \hat{a}^{\varepsilon\zeta}} \left( \frac{1}{\sqrt{\det[\hat{a}^{\alpha\beta}]}} \right) \frac{\partial \hat{a}^{\varepsilon\zeta}}{\partial a_{\gamma\delta}} \\ &= -\frac{1}{2}\, \frac{1}{\sqrt{\det[A_{\alpha\beta}]}}\, \frac{1}{\left(\sqrt{\det[\hat{a}^{\alpha\beta}]}\right)^{3/2}}\, \frac{\partial}{\partial \hat{a}^{\varepsilon\zeta}} \left(\det[\hat{a}^{\alpha\beta}]\right)\, \frac{\partial \hat{a}^{\varepsilon\zeta}}{\partial a_{\gamma\delta}} \\ &= -\frac{1}{2}\, J_{\mathrm{in}}\, \hat{a}_{\varepsilon\zeta}\, \frac{\partial \hat{a}^{\varepsilon\zeta}}{\partial a_{\gamma\delta}} \ , \end{aligned} \tag{A3}$$

as $\partial \left(\det[\hat{a}^{\alpha\beta}]\right) / \partial \hat{a}^{\varepsilon\zeta} = \det[\hat{a}^{\alpha\beta}]\, \hat{a}_{\varepsilon\zeta}$. Likewise,

$$\begin{aligned} \frac{\partial J_{\mathrm{el}}}{\partial a_{\gamma\delta}} &= \sqrt{\det[\hat{a}^{\alpha\beta}]}\, \frac{\partial \left(\sqrt{\det[a_{\alpha\beta}]}\right)}{\partial a_{\gamma\delta}} + \sqrt{\det[a_{\alpha\beta}]}\, \frac{\partial \left(\sqrt{\det[\hat{a}^{\alpha\beta}]}\right)}{\partial a_{\gamma\delta}} \\ &= \frac{1}{2}\, \frac{\sqrt{\det[\hat{a}^{\alpha\beta}]}}{\sqrt{\det[a_{\alpha\beta}]}}\, \frac{\partial \left(\det[a_{\alpha\beta}]\right)}{\partial a_{\gamma\delta}} + \frac{1}{2}\, \frac{\sqrt{\det[a_{\alpha\beta}]}}{\sqrt{\det[\hat{a}^{\alpha\beta}]}}\, \frac{\partial \left(\det[\hat{a}^{\alpha\beta}]\right)}{\partial \hat{a}^{\varepsilon\zeta}}\, \frac{\partial \hat{a}^{\varepsilon\zeta}}{\partial a_{\gamma\delta}} \\ &= \frac{1}{2}\, J_{\mathrm{el}}\, a^{\gamma\delta} + \frac{1}{2}\, J_{\mathrm{el}}\, \hat{a}_{\varepsilon\zeta}\, \frac{\partial \hat{a}^{\varepsilon\zeta}}{\partial a_{\gamma\delta}} \ , \end{aligned} \tag{A4}$$

as $\partial \left(\det[a_{\alpha\beta}]\right) / \partial a_{\gamma\delta} = \det[a_{\alpha\beta}]\, a^{\gamma\delta}$. The derivatives of the mean curvature $\hat{H}$, see Equation (24.1), w.r.t. $a_{\gamma\delta}$ and $b_{\gamma\delta}$ are given by

$$\frac{\partial \hat{H}}{\partial a_{\gamma\delta}} = \frac{1}{2} \left( \frac{\partial \hat{a}^{\varepsilon\zeta}}{\partial a_{\gamma\delta}}\, \hat{b}_{\varepsilon\zeta} + \hat{a}^{\varepsilon\zeta}\, \frac{\partial \hat{b}_{\varepsilon\zeta}}{\partial a_{\gamma\delta}} \right) , \quad \text{and} \quad \frac{\partial \hat{H}}{\partial b_{\gamma\delta}} = \frac{1}{2} \left( \frac{\partial \hat{a}^{\varepsilon\zeta}}{\partial b_{\gamma\delta}}\, \hat{b}_{\varepsilon\zeta} + \hat{a}^{\varepsilon\zeta}\, \frac{\partial \hat{b}_{\varepsilon\zeta}}{\partial b_{\gamma\delta}} \right). \tag{A5}$$

For the derivatives in Equations (A2)–(A5), the derivatives of $\hat{a}^{\varepsilon\zeta}$ and $\hat{b}_{\varepsilon\zeta}$ w.r.t. $a_{\gamma\delta}$ and $b_{\gamma\delta}$ need to be computed, due to the elimination noted in Remark 8. The derivation of these derivatives depends on the employed material model and is presented in Appendix A.3. Further, the following derivatives are used in the subsequent sections[78]

$$\begin{aligned} a^{\alpha\beta\gamma\delta} &:= \frac{\partial a^{\alpha\beta}}{\partial a_{\gamma\delta}} = -\frac{1}{2} \left( a^{\alpha\gamma}\, a^{\beta\delta} + a^{\alpha\delta}\, a^{\beta\gamma} \right) , \\ \hat{a}^{\alpha\beta\gamma\delta} &:= \frac{\partial \hat{a}^{\alpha\beta}}{\partial \hat{a}_{\gamma\delta}} = -\frac{1}{2} \left( \hat{a}^{\alpha\gamma}\, \hat{a}^{\beta\delta} + \hat{a}^{\alpha\delta}\, \hat{a}^{\beta\gamma} \right) , \quad \text{and} \\ b^{\alpha\beta\gamma\delta} &:= \frac{\partial b^{\alpha\beta}}{\partial a_{\gamma\delta}} = -\frac{1}{2} \left( a^{\alpha\gamma}\, b^{\beta\delta} + b^{\alpha\gamma}\, a^{\beta\delta} + a^{\alpha\delta}\, b^{\beta\gamma} + b^{\alpha\delta}\, a^{\beta\gamma} \right) , \end{aligned} \tag{A6}$$

from which $\partial b^{\alpha\beta} / \partial b_{\gamma\delta} = -a^{\alpha\beta\gamma\delta}$ follows.

MOST WIEDZY Downloaded from mostwiedzy.pl

### A.2 Linearization for the implicit Euler scheme

For the time integration of the evolution laws based on the implicit Euler scheme, the derivatives in Equation (80) are required for the different material models. Subsequently, those derivatives are reported.

#### A.2.1 Koiter membrane model

The derivative of Equation (83) w.r.t. $\hat{a}^{\alpha\beta}$ is given by

$$\frac{\partial \hat{\mathrm{g}}_{\mathrm{s}}^{\alpha\beta}}{\partial \hat{a}^{\gamma\delta}} = \frac{1}{\Delta t}\ \delta_{\gamma}^{\alpha}\ \delta_{\delta}^{\beta} + \frac{\Lambda_1}{2\ \eta_{\mathrm{s}}}\ \left(\hat{a}^{\alpha\beta}\ a_{\gamma\delta} + \left(I_1^{\mathrm{el}} - 2\right)\ \delta_{\gamma}^{\alpha}\ \delta_{\delta}^{\beta}\right) + \frac{\mu_1}{\eta_{\mathrm{s}}}\ \left(a_{\delta\varepsilon}\ \left(\delta_{\gamma}^{\alpha}\ \hat{a}^{\beta\varepsilon} + \delta_{\gamma}^{\beta}\ \hat{a}^{\alpha\varepsilon}\right) - \delta_{\gamma}^{\alpha}\ \delta_{\delta}^{\beta}\right), \tag{A7}$$

with Kronecker delta $\delta_{\beta}^{\alpha}$.

#### A.2.2 Neo-Hookean membrane model with dilatational/deviatoric split

The derivative of Equation (86) w.r.t. $\hat{a}^{\alpha\beta}$ is given by

$$\frac{\partial \hat{\mathrm{g}}_{\mathrm{s}}^{\alpha\beta}}{\partial \hat{a}^{\gamma\delta}} = \frac{1}{\Delta t}\ \delta_{\gamma}^{\alpha}\ \delta_{\delta}^{\beta} + \frac{K_1}{2\ \eta_{\mathrm{s}}}\ J_{\mathrm{el}}^2\ a^{\alpha\beta}\ \hat{a}_{\gamma\delta} + \frac{\mu_1}{2\ \eta_{\mathrm{s}}\ J_{\mathrm{el}}}\ \left(2\ \delta_{\gamma}^{\alpha}\ \delta_{\delta}^{\beta} - a^{\alpha\beta}\ a_{\gamma\delta} - \hat{a}^{\alpha\beta}\ \hat{a}_{\gamma\delta} + \frac{1}{2}\ I_1^{\mathrm{el}}\ a^{\alpha\beta}\ \hat{a}_{\gamma\delta}\right), \tag{A8}$$

with $\left[\hat{a}_{\alpha\beta}\right] = \left[\hat{a}^{\alpha\beta}\right]^{-1}$ and Kronecker delta $\delta_{\beta}^{\alpha}$.

#### A.2.3 Incompressible Neo-Hookean membrane model

The derivative of Equation (87) w.r.t. $\hat{a}^{\gamma\delta}$ is given by

$$\frac{\partial \hat{\mathrm{g}}_{\mathrm{s}}^{\alpha\beta}}{\partial \hat{a}^{\gamma\delta}} = \frac{1}{\Delta t}\ \delta_{\gamma}^{\alpha}\ \delta_{\delta}^{\beta} + \frac{\mu_1}{\eta_{\mathrm{s}}}\ \left(\delta_{\gamma}^{\alpha}\ \delta_{\delta}^{\beta} + \frac{a^{\alpha\beta}}{J_{\mathrm{el}}^2}\ \hat{a}_{\gamma\delta}\right), \tag{A9}$$

with $\left[\hat{a}_{\alpha\beta}\right] = \left[\hat{a}^{\alpha\beta}\right]^{-1}$ and Kronecker delta $\delta_{\beta}^{\alpha}$.

#### A.2.4 Membranes with constant surface tension

The derivative of Equation (88) w.r.t. $\hat{a}^{\gamma\delta}$ is given by

$$\frac{\partial \hat{\mathrm{g}}_{\mathrm{s}}^{\alpha\beta}}{\partial \hat{a}^{\gamma\delta}} = \frac{1}{\Delta t}\ \delta_{\gamma}^{\alpha}\ \delta_{\delta}^{\beta} + \frac{\hat{\gamma}}{2\ \eta_{\mathrm{s}}}\ J_{\mathrm{el}}\ a^{\alpha\beta}\ \hat{a}_{\gamma\delta}, \tag{A10}$$

with $\left[\hat{a}_{\alpha\beta}\right] = \left[\hat{a}^{\alpha\beta}\right]^{-1}$ and Kronecker delta $\delta_{\beta}^{\alpha}$.

#### A.2.5 Helfrich bending model

The derivatives of Equations (91) and (92) w.r.t. $\hat{a}^{\gamma\delta}$ and $\hat{b}_{\gamma\delta}$ are given by

$$\begin{aligned}
\frac{\partial \hat{\mathrm{g}}_{\mathrm{s}}^{\alpha\beta}}{\partial \hat{a}^{\gamma\delta}} &= \frac{1}{\Delta t}\ \delta_{\gamma}^{\alpha}\ \delta_{\delta}^{\beta} + \frac{k_1\ J_{\mathrm{el}}}{\eta_{\mathrm{s}}}\ \left[\left(\frac{1}{2}\Delta H^2\ a^{\alpha\beta} - \Delta H\ b^{\alpha\beta}\right)\ \hat{a}_{\gamma\delta} - \left(\Delta H\ a^{\alpha\beta} - b^{\alpha\beta}\right)\ \hat{b}_{\gamma\delta}\right]\ , \\
\frac{\partial \hat{\mathrm{g}}_{\mathrm{s}}^{\alpha\beta}}{\partial \hat{b}_{\gamma\delta}} &= -\frac{k_1\ J_{\mathrm{el}}}{\eta_{\mathrm{s}}}\ \left(\Delta H\ a^{\alpha\beta} - b^{\alpha\beta}\right)\ \hat{a}^{\gamma\delta}\ ,
\end{aligned} \tag{A11}$$

and

$$\begin{aligned}
\frac{\partial \hat{\mathrm{g}}_{\alpha\beta}^{\mathrm{b}}}{\partial \hat{a}^{\gamma\delta}} &= -\frac{k_1\ J_{\mathrm{el}}}{\eta_{\mathrm{b}}}\ a_{\alpha\beta}\ \left(\Delta H\ \hat{a}_{\gamma\delta} - \hat{b}_{\gamma\delta}\right)\ , \\
\frac{\partial \hat{\mathrm{g}}_{\alpha\beta}^{\mathrm{b}}}{\partial \hat{b}_{\gamma\delta}} &= \frac{1}{\Delta t}\ \delta_{\gamma}^{\alpha}\ \delta_{\delta}^{\beta} + \frac{k_1\ J_{\mathrm{el}}}{2\ \eta_{\mathrm{b}}}\ a_{\alpha\beta}\ \hat{a}^{\gamma\delta}\ ,
\end{aligned} \tag{A12}$$

with $\left[\hat{a}_{\alpha\beta}\right] = \left[\hat{a}^{\alpha\beta}\right]^{-1}$, Kronecker delta $\delta_{\beta}^{\alpha}$, and $\Delta H := H - \hat{H}$.

MOST WIEDZY Downloaded from mostwiedzy.pl

### A.3 Linearization for the finite element method

Subsequently, the additional contributions in the tangent matrices, see Equations (97)–(98), coming from the Maxwell branch are derived for the employed material models.

#### A.3.1 Koiter membrane model

Given the stresses in Equation (35),** the contribution in the linearized weak form is

$$\begin{aligned} c_1^{\alpha\beta\gamma\delta} &= 2\,\frac{\partial \tau_{1(\mathrm{el})}^{\alpha\beta}}{\partial a_{\gamma\delta}} \\ &= \Lambda_1\,\frac{\partial J_{\mathrm{in}}}{\partial a_{\gamma\delta}}\,\left(I_1^{\mathrm{el}}-2\right)\,\hat{a}^{\alpha\beta} + \Lambda_1\,J_{\mathrm{in}}\left(\frac{\partial I_1^{\mathrm{el}}}{\partial a_{\gamma\delta}}\,\hat{a}^{\alpha\beta} + \left(I_1^{\mathrm{el}}-2\right)\,\frac{\partial \hat{a}^{\alpha\beta}}{\partial a_{\gamma\delta}}\right) \\ &\quad + 2\,\mu_1\,\frac{\partial J_{\mathrm{in}}}{\partial a_{\gamma\delta}}\,\left(\hat{a}^{\alpha\epsilon}\,a_{\epsilon\zeta}\,\hat{a}^{\beta\zeta} - \hat{a}^{\alpha\beta}\right) \\ &\quad + 2\,\mu_1\,J_{\mathrm{in}}\left(\frac{\partial \hat{a}^{\alpha\epsilon}}{\partial a_{\gamma\delta}}\,a_{\epsilon\zeta}\,\hat{a}^{\beta\zeta} + \frac{1}{2}\,\left(\hat{a}^{\alpha\gamma}\,\hat{a}^{\beta\delta} + \hat{a}^{\alpha\delta}\,\hat{a}^{\beta\gamma}\right) + \hat{a}^{\alpha\epsilon}\,a_{\epsilon\zeta}\,\frac{\partial \hat{a}^{\beta\zeta}}{\partial a_{\gamma\delta}} - \frac{\partial \hat{a}^{\alpha\beta}}{\partial a_{\gamma\delta}}\right). \end{aligned} \tag{A13}$$

Still, the derivative $\partial \hat{a}^{\alpha\beta}/\partial a_{\gamma\delta}$ needs to be found to evaluate Equation (A13). For this, the nonlinear equations in Equation (83), which need to be solved for $\hat{a}^{\alpha\beta}$ within the element routine at each quadrature point and each time step, need to be differentiated w.r.t. $a_{\gamma\delta}$. The auxiliary arrays

$$\hat{\mathbf{a}}_{\mathrm{con}} := \begin{bmatrix} \hat{a}^{11} \\ \hat{a}^{12} \\ \hat{a}^{21} \\ \hat{a}^{22} \end{bmatrix}, \quad \hat{\mathbf{a}}_{\mathrm{co}} := \begin{bmatrix} \hat{a}_{11} \\ \hat{a}_{12} \\ \hat{a}_{21} \\ \hat{a}_{22} \end{bmatrix}, \quad \mathbf{a}_{\mathrm{con}} := \begin{bmatrix} a^{11} \\ a^{12} \\ a^{21} \\ a^{22} \end{bmatrix}, \quad \text{and} \quad \mathbf{a}_{\mathrm{co}} := \begin{bmatrix} a_{11} \\ a_{12} \\ a_{21} \\ a_{22} \end{bmatrix}, \tag{A14}$$

are defined to simplify the notation. The required derivatives $\partial \hat{a}^{\alpha\beta}/\partial a_{\gamma\delta}$ can then be extracted from the $(4\times 4)$-matrix

$$\frac{\partial \hat{\mathbf{a}}_{\mathrm{con}}}{\partial \mathbf{a}_{\mathrm{co}}} = \begin{bmatrix} \partial \hat{a}^{11}/\partial a_{11} & \partial \hat{a}^{11}/\partial a_{12} & \partial \hat{a}^{11}/\partial a_{21} & \partial \hat{a}^{11}/\partial a_{22} \\ \partial \hat{a}^{12}/\partial a_{11} & \partial \hat{a}^{12}/\partial a_{12} & \partial \hat{a}^{12}/\partial a_{21} & \partial \hat{a}^{12}/\partial a_{22} \\ \partial \hat{a}^{21}/\partial a_{11} & \partial \hat{a}^{21}/\partial a_{12} & \partial \hat{a}^{21}/\partial a_{21} & \partial \hat{a}^{21}/\partial a_{22} \\ \partial \hat{a}^{22}/\partial a_{11} & \partial \hat{a}^{22}/\partial a_{12} & \partial \hat{a}^{22}/\partial a_{21} & \partial \hat{a}^{22}/\partial a_{22} \end{bmatrix}, \tag{A15}$$

which follows from the solution of

$$\left[\left(\frac{\eta_{\mathrm{s}}}{\Delta t} - \mu_1 + \frac{\Lambda_1}{2}\,\left(I_1^{\mathrm{el}}-2\right)\right)\,\mathbf{I}_4 + \frac{\Lambda_1}{2}\,\hat{\mathbf{a}}_{\mathrm{con}}\,\mathbf{a}_{\mathrm{co}}^{\mathrm{T}} + \mu_1\,\tilde{\mathbf{C}}\right]\,\frac{\partial \hat{\mathbf{a}}_{\mathrm{con}}}{\partial \mathbf{a}_{\mathrm{co}}} = -\frac{\Lambda_1}{2}\,\hat{\mathbf{a}}_{\mathrm{con}}\,\hat{\mathbf{a}}_{\mathrm{con}}^{\mathrm{T}} + \mu_1\,\frac{\partial \hat{\mathbf{a}}_{\mathrm{con}}}{\partial \hat{\mathbf{a}}_{\mathrm{co}}}, \tag{A16}$$

where $\mathbf{I}_4$ denotes the $(4\times 4)$-identity matrix. The derivative $\partial \hat{\mathbf{a}}_{\mathrm{con}}/\partial \hat{\mathbf{a}}_{\mathrm{co}}$ follows from Equation (A6.2) and it is arranged in analogy to Equation (A15). The matrix $\tilde{\mathbf{C}}$ is given by

$$\tilde{\mathbf{C}} := \begin{bmatrix} 2\,c_1^1 & 2\,c_2^1 & 0 & 0 \\ c_1^2 & c_2^2 & c_1^1 & c_2^1 \\ c_1^2 & c_2^2 & c_1^1 & c_2^1 \\ 0 & 0 & 2\,c_1^2 & 2\,c_2^2 \end{bmatrix}, \tag{A17}$$

with $c_\gamma^\alpha := \hat{a}^{\alpha\beta}\,a_{\beta\gamma}$.

*Remark* 9. Note that the computation of the derivatives $\partial \hat{a}^{\alpha\beta}/\partial a_{\gamma\delta}$ can become more efficient by exploiting the symmetries of $\hat{a}^{\alpha\beta}$ and $a_{\alpha\beta}$, i.e., $\hat{a}^{12} = \hat{a}^{21}$ and $a_{12} = a_{21}$. The $(4\times 4)$-matrix in Equation (A15) can then be reduced to a $(3\times 3)$-matrix, such that also the dimension of the linear system of equations in Equation (A16) decreases.

MOST WIEDZY Downloaded from mostwiedzy.pl

### A.3.2 Neo-Hookean membrane model

Considering the stresses in Equation (37) with $\Lambda = 0$,[8] the corresponding linearization is

$$c_1^{\alpha\beta\gamma\delta} = 2\,\frac{\partial \tau_{1(\mathrm{el})}^{\alpha\beta}}{\partial a_{\gamma\delta}} = 2\,\mu_1\,\left[\frac{\partial J_{\mathrm{in}}}{\partial a_{\gamma\delta}}\,\left(\hat{a}^{\alpha\beta} - a^{\alpha\beta}\right) + J_{\mathrm{in}}\,\left(\frac{\partial \hat{a}^{\alpha\beta}}{\partial a_{\gamma\delta}} - a^{\alpha\beta\gamma\delta}\right)\right], \tag{A18}$$

where

$$\frac{\partial \hat{a}^{\alpha\beta}}{\partial a_{\gamma\delta}} = \frac{\mu_1\,\Delta t}{\eta_{\mathrm{s}} + \mu_1\,\Delta t}\,a^{\alpha\beta\gamma\delta}, \tag{A19}$$

see also Equation (85). Note that if $\eta_{\mathrm{s}}/\Delta t \to 0$, the derivative in Equation (A19) approaches $a^{\alpha\beta\gamma\delta}$, and for $\eta_{\mathrm{s}}/\Delta t \to \infty$ it approaches zero.

### A.3.3 Neo-Hookean membrane model with dilatational/deviatoric split

Given the stress in Equation (39),[8] the contribution in the linearized weak form is

$$\begin{aligned} c_1^{\alpha\beta\gamma\delta} = 2\,\frac{\partial \tau_{1(\mathrm{el})}^{\alpha\beta}}{\partial a_{\gamma\delta}} = K_1\,&\left[\frac{\partial J_{\mathrm{in}}}{\partial a_{\gamma\delta}}\,\left(J_{\mathrm{el}}^2 - 1\right)\,a^{\alpha\beta} + 2\,J\,\frac{\partial J_{\mathrm{el}}}{\partial a_{\gamma\delta}}\,a^{\alpha\beta} + J_{\mathrm{in}}\,\left(J_{\mathrm{el}}^2 - 1\right)\,a^{\alpha\beta\gamma\delta}\right] \\ &+ \mu_1\,\left[-\frac{J_{\mathrm{in}}}{J_{\mathrm{el}}^2}\,\frac{\partial J_{\mathrm{el}}}{\partial a_{\gamma\delta}}\,\left(2\,\hat{a}^{\alpha\beta} - I_1^{\mathrm{el}}\,a^{\alpha\beta}\right) + \frac{1}{J_{\mathrm{el}}}\,\frac{\partial J_{\mathrm{in}}}{\partial a_{\gamma\delta}}\,\left(2\,\hat{a}^{\alpha\beta} - I_1^{\mathrm{el}}\,a^{\alpha\beta}\right)\right. \\ &\left. + \frac{J_{\mathrm{in}}}{J_{\mathrm{el}}}\,\left(2\,\frac{\partial \hat{a}^{\alpha\beta}}{\partial a_{\gamma\delta}} - \frac{\partial I_1^{\mathrm{el}}}{\partial a_{\gamma\delta}}\,a^{\alpha\beta} - I_1^{\mathrm{el}}\,a^{\alpha\beta\gamma\delta}\right)\right]. \end{aligned} \tag{A20}$$

Still, the derivative $\partial \hat{a}^{\alpha\beta}/\partial a_{\gamma\delta}$ needs to be found to evaluate Equation (A20). For this, the nonlinear equations from Equation (86), which need to be solved for $\hat{a}^{\alpha\beta}$ in the element routine at each quadrature point and each time step, need to be differentiated w.r.t. $a_{\gamma\delta}$. Similar to Equation (A16), the required derivatives $\partial \hat{a}^{\alpha\beta}/\partial a_{\gamma\delta}$ can be extracted from the $(4\times 4)$-matrix $\partial \hat{\mathbf{a}}_{\mathrm{con}}/\partial \mathbf{a}_{\mathrm{co}}$, see Equation (A15), which follows from the solution of

$$\begin{aligned} &\left[\left(\frac{2\,\eta_{\mathrm{s}}}{\Delta t} + \frac{2\,\mu_1}{J_{\mathrm{el}}}\right)\,\mathbf{I}_4 + \left(K_1\,J_{\mathrm{el}}^2 + \frac{\mu_1\,I_1^{\mathrm{el}}}{2\,J_{\mathrm{el}}}\right)\,\mathbf{a}_{\mathrm{con}}\,\hat{\mathbf{a}}_{\mathrm{co}}^{\mathrm{T}} - \frac{\mu_1}{J_{\mathrm{el}}}\,\left(\hat{\mathbf{a}}_{\mathrm{con}}\,\hat{\mathbf{a}}_{\mathrm{co}}^{\mathrm{T}} + \mathbf{a}_{\mathrm{con}}\,\mathbf{a}_{\mathrm{co}}^{\mathrm{T}}\right)\right]\,\frac{\partial \hat{\mathbf{a}}_{\mathrm{con}}}{\partial \mathbf{a}_{\mathrm{co}}} \\ &= -K_1\,\left(J_{\mathrm{el}}^2\,\mathbf{a}_{\mathrm{con}}\,\mathbf{a}_{\mathrm{con}}^{\mathrm{T}} + \left(J_{\mathrm{el}}^2 - 1\right)\,\frac{\partial \mathbf{a}_{\mathrm{con}}}{\partial \mathbf{a}_{\mathrm{co}}}\right) \\ &\quad + \frac{\mu_1}{J_{\mathrm{el}}}\,\left(\mathbf{a}_{\mathrm{con}}\,\hat{\mathbf{a}}_{\mathrm{con}}^{\mathrm{T}} + I_1^{\mathrm{el}}\,\frac{\partial \mathbf{a}_{\mathrm{con}}}{\partial \mathbf{a}_{\mathrm{co}}} + \hat{\mathbf{a}}_{\mathrm{con}}\,\mathbf{a}_{\mathrm{con}}^{\mathrm{T}} - \frac{I_1^{\mathrm{el}}}{2}\,\mathbf{a}_{\mathrm{con}}\,\mathbf{a}_{\mathrm{con}}^{\mathrm{T}}\right), \end{aligned} \tag{A21}$$

where $\mathbf{I}_4$ denotes the $(4\times 4)$-identity matrix. The derivative $\partial \mathbf{a}_{\mathrm{con}}/\partial \mathbf{a}_{\mathrm{co}}$ follows from Equation (A6.1) and it is arranged in analogy to Equation (A15).

### A.3.4 Incompressible Neo-Hookean membrane model

Given the stresses in Equation (41),[8] the contribution in the linearized weak form is

$$c_1^{\alpha\beta\gamma\delta} = 2\,\frac{\partial \tau_{1(\mathrm{el})}^{\alpha\beta}}{\partial a_{\gamma\delta}} = 2\,\mu_1\,\left[\frac{\partial J_{\mathrm{in}}}{\partial a_{\gamma\delta}}\,\left(\hat{a}^{\alpha\beta} - \frac{a^{\alpha\beta}}{J_{\mathrm{el}}^2}\right) + J_{\mathrm{in}}\,\left(\frac{\partial \hat{a}^{\alpha\beta}}{\partial a_{\gamma\delta}} - \frac{a^{\alpha\beta\gamma\delta}}{J_{\mathrm{el}}^2} + 2\,\frac{a^{\alpha\beta}}{J_{\mathrm{el}}^3}\,\frac{\partial J_{\mathrm{el}}}{\partial a_{\gamma\delta}}\right)\right]. \tag{A22}$$

The required derivative $\partial \hat{a}^{\alpha\beta}/\partial a_{\gamma\delta}$ is extracted from the $(4\times 4)$-matrix $\partial \hat{\mathbf{a}}_{\mathrm{con}}/\partial \mathbf{a}_{\mathrm{co}}$, see Equation (A15), which follows from the solution of

$$\left[\left(\frac{\eta_{\mathrm{s}}}{\Delta t} + \mu_1\right)\,\mathbf{I}_4 + \frac{\mu_1}{J_{\mathrm{el}}^2}\,\mathbf{a}_{\mathrm{con}}\,\hat{\mathbf{a}}_{\mathrm{co}}^{\mathrm{T}}\right]\,\frac{\partial \hat{\mathbf{a}}_{\mathrm{con}}}{\partial \mathbf{a}_{\mathrm{co}}} = \frac{\mu_1}{J_{\mathrm{el}}^2}\,\left(\frac{\partial \mathbf{a}_{\mathrm{con}}}{\partial \mathbf{a}_{\mathrm{co}}} - \mathbf{a}_{\mathrm{con}}\,\mathbf{a}_{\mathrm{con}}^{\mathrm{T}}\right), \tag{A23}$$

MOST WIEDZY Downloaded from mostwiedzy.pl

where $\mathbf{I}_4$ denotes the $(4 \times 4)$-identity matrix. The derivative $\partial \mathbf{a}_{\text{con}} / \partial \mathbf{a}_{\text{co}}$ follows from Equation (A6.1) and it is arranged in analogy to Equation (A15).

### A.3.5 Membranes with constant surface tension

Given the stresses in Equation (43),[8] the contribution in the linearized weak form is

$$c_1^{\alpha\beta\gamma\delta} = 2\, \frac{\partial \tau_{1(\text{el})}^{\alpha\beta}}{\partial a_{\gamma\delta}} = \hat{\gamma}\, J\, \left( a^{\alpha\beta}\, a^{\gamma\delta} + 2\, a^{\alpha\beta\gamma\delta} \right). \tag{A24}$$

### A.3.6 Koiter bending model

For the moment components given in Equation (45),[8] the material tangent is given by

$$f_1^{\alpha\beta\gamma\delta} = \frac{\partial M_{0(1)(\text{el})}^{\alpha\beta}}{\partial b_{\gamma\delta}} = J_{\text{in}}\, \hat{f}^{\alpha\beta\gamma\delta}\, \frac{\eta_{\text{b}}}{\eta_{\text{b}} + c_1\, \Delta t}, \tag{A25}$$

as the derivative $\partial \hat{b}_{\alpha\beta} / \partial b_{\gamma\delta}$ follows in analogy to Equation (A19).

### A.3.7 Helfrich bending model

Given the stress and moment components in Equations (47)–(48) with $k^\star = 0$,[8] the material tangents in Equation (97) follow as

$$\begin{aligned}
c_1^{\alpha\beta\gamma\delta} &= 2\, k_1\, J\, \left( \left( \frac{1}{2} \Delta H^2\, a^{\alpha\beta} - \Delta H\, b^{\alpha\beta} \right) a^{\gamma\delta} \right. \\
&\qquad \left. + \left( \Delta H\, a^{\alpha\beta} - b^{\alpha\beta} \right)\, \Delta H_a^{\gamma\delta} + \Delta H^2\, a^{\alpha\beta\gamma\delta} - 2\, \Delta H\, b^{\alpha\beta\gamma\delta} \right), \\
d_1^{\alpha\beta\gamma\delta} &= k_1\, J\, \left( \left( \Delta H\, a^{\alpha\beta} - b^{\alpha\beta} \right)\, \Delta H_b^{\gamma\delta} + 2\, \Delta H\, a^{\alpha\beta\gamma\delta} \right), \\
e_1^{\alpha\beta\gamma\delta} &= k_1\, J\, \left( \Delta H\, a^{\alpha\beta}\, a^{\gamma\delta} + \Delta H_a^{\gamma\delta}\, a^{\alpha\beta} + 2\, \Delta H\, a^{\alpha\beta\gamma\delta} \right), \\
f_1^{\alpha\beta\gamma\delta} &= \frac{k_1\, J}{2}\, \Delta H_b^{\gamma\delta}\, a^{\alpha\beta},
\end{aligned} \tag{A26}$$

where $\Delta H := H - \hat{H}$ and

$$\Delta H_a^{\gamma\delta} := -b^{\gamma\delta} - \frac{\partial \hat{a}^{\varepsilon\zeta}}{\partial a_{\gamma\delta}}\, \hat{b}_{\varepsilon\zeta} - \hat{a}^{\varepsilon\zeta}\, \frac{\partial \hat{b}_{\varepsilon\zeta}}{\partial a_{\gamma\delta}}, \quad \text{and} \quad \Delta H_b^{\gamma\delta} := a^{\gamma\delta} - \frac{\partial \hat{a}^{\varepsilon\zeta}}{\partial b_{\gamma\delta}}\, \hat{b}_{\varepsilon\zeta} - \hat{a}^{\varepsilon\zeta}\, \frac{\partial \hat{b}_{\varepsilon\zeta}}{\partial b_{\gamma\delta}}. \tag{A27}$$

Still, the derivatives of $\hat{a}^{\varepsilon\zeta}$ and $\hat{b}_{\varepsilon\zeta}$ w.r.t. $a_{\gamma\delta}$ and $b_{\gamma\delta}$ are required. For this, the nonlinear algebraic equations from Equations (91) and (92) are differentiated w.r.t. $a_{\gamma\delta}$ and $b_{\gamma\delta}$. In analogy to Equation (A14), the auxiliary arrays

$$\hat{\mathbf{b}}_{\text{con}} := \begin{bmatrix} \hat{b}^{11} \\ \hat{b}^{12} \\ \hat{b}^{21} \\ \hat{b}^{22} \end{bmatrix}, \quad \hat{\mathbf{b}}_{\text{co}} := \begin{bmatrix} \hat{b}_{11} \\ \hat{b}_{12} \\ \hat{b}_{21} \\ \hat{b}_{22} \end{bmatrix}, \quad \mathbf{b}_{\text{con}} := \begin{bmatrix} b^{11} \\ b^{12} \\ b^{21} \\ b^{22} \end{bmatrix}, \quad \text{and} \quad \mathbf{b}_{\text{co}} := \begin{bmatrix} b_{11} \\ b_{12} \\ b_{21} \\ b_{22} \end{bmatrix}, \tag{A28}$$

are defined to simplify the notation. The required derivatives are then obtained by solving

$$\begin{bmatrix} \partial \hat{\mathbf{g}}_{\text{s}} / \partial \mathbf{a}_{\text{co}} \\ \partial \hat{\mathbf{g}}_{\text{s}} / \partial \mathbf{b}_{\text{co}} \\ \partial \hat{\mathbf{g}}^{\text{b}} / \partial \mathbf{a}_{\text{co}} \\ \partial \hat{\mathbf{g}}^{\text{b}} / \partial \mathbf{b}_{\text{co}} \end{bmatrix} = \mathbf{0}, \tag{A29}$$

MOST WIEDZY Downloaded from mostwiedzy.pl

for the unknown derivatives. The resulting linear equation system is given by

$$\begin{bmatrix} \mathbf{A}_{11} & \mathbf{0} & \mathbf{A}_{13} & \mathbf{0} \\ \mathbf{0} & \mathbf{A}_{22} & \mathbf{0} & \mathbf{A}_{24} \\ \mathbf{A}_{31} & \mathbf{0} & \mathbf{A}_{33} & \mathbf{0} \\ \mathbf{0} & \mathbf{A}_{42} & \mathbf{0} & \mathbf{A}_{44} \end{bmatrix} \begin{bmatrix} \partial \hat{\mathbf{a}}_{\mathrm{con}} / \partial \mathbf{a}_{\mathrm{co}} \\ \partial \hat{\mathbf{a}}_{\mathrm{con}} / \partial \mathbf{b}_{\mathrm{co}} \\ \partial \hat{\mathbf{b}}_{\mathrm{co}} / \partial \mathbf{a}_{\mathrm{co}} \\ \partial \hat{\mathbf{b}}_{\mathrm{co}} / \partial \mathbf{b}_{\mathrm{co}} \end{bmatrix} = \begin{bmatrix} \mathbf{r}_1 \\ \mathbf{r}_2 \\ \mathbf{r}_3 \\ \mathbf{r}_4 \end{bmatrix}, \tag{A30}$$

with the $(4 \times 4)$-tangent matrix blocks

$$\begin{aligned} \mathbf{A}_{11} &:= \frac{\eta_{\mathrm{s}}}{k_1\ \Delta t\ J_{\mathrm{el}}}\ \mathbf{I}_4 + \mathbf{c}_{\mathrm{con}}\ \hat{\mathbf{a}}_{\mathrm{co}}^{\mathrm{T}} - \mathbf{d}_{\mathrm{con}}\ \hat{\mathbf{b}}_{\mathrm{co}}^{\mathrm{T}}\ , & \mathbf{A}_{13} &:= -\mathbf{d}_{\mathrm{con}}\ \hat{\mathbf{a}}_{\mathrm{con}}^{\mathrm{T}}\ , \\ \mathbf{A}_{22} &:= \frac{\eta_{\mathrm{s}}}{k_1\ \Delta t\ J_{\mathrm{el}}}\ \mathbf{I}_4 - \mathbf{d}_{\mathrm{con}}\ \hat{\mathbf{b}}_{\mathrm{co}}^{\mathrm{T}}\ , & \mathbf{A}_{24} &:= -\mathbf{d}_{\mathrm{con}}\ \hat{\mathbf{a}}_{\mathrm{con}}^{\mathrm{T}}\ , \\ \mathbf{A}_{31} &:= -\frac{1}{2}\ \left(\Delta H\ \mathbf{a}_{\mathrm{co}}\ \hat{\mathbf{a}}_{\mathrm{co}}^{\mathrm{T}} - \mathbf{a}_{\mathrm{co}}\ \hat{\mathbf{b}}_{\mathrm{co}}^{\mathrm{T}}\right)\ , & \mathbf{A}_{33} &:= \frac{\eta_{\mathrm{b}}}{k_1\ \Delta t\ J_{\mathrm{el}}}\ \mathbf{I}_4 + \frac{1}{2}\ \mathbf{a}_{\mathrm{co}}\ \hat{\mathbf{a}}_{\mathrm{con}}^{\mathrm{T}}\ , \\ \mathbf{A}_{42} &:= \frac{1}{2}\ \mathbf{a}_{\mathrm{co}}\ \hat{\mathbf{b}}_{\mathrm{co}}^{\mathrm{T}}\ , & \mathbf{A}_{44} &:= \frac{\eta_{\mathrm{b}}}{k_1\ \Delta t\ J_{\mathrm{el}}}\ \mathbf{I}_4 + \frac{1}{2}\ \mathbf{a}_{\mathrm{co}}\ \hat{\mathbf{a}}_{\mathrm{con}}^{\mathrm{T}}\ , \end{aligned} \tag{A31}$$

and the $(4 \times 4)$-right-hand-side blocks

$$\begin{aligned} \mathbf{r}_1 &:= -\mathbf{c}_{\mathrm{con}}\ \mathbf{a}_{\mathrm{con}}^{\mathrm{T}} + \mathbf{d}_{\mathrm{con}}\ \mathbf{b}_{\mathrm{con}}^{\mathrm{T}} - \Delta H^2\ \frac{\partial \mathbf{a}_{\mathrm{con}}}{\partial \mathbf{a}_{\mathrm{co}}} + 2\ \Delta H\ \frac{\partial \mathbf{b}_{\mathrm{con}}}{\partial \mathbf{b}_{\mathrm{co}}}\ , \\ \mathbf{r}_2 &:= -\mathbf{d}_{\mathrm{con}}\ \mathbf{a}_{\mathrm{con}}^{\mathrm{T}} + 2\ \Delta H\ \frac{\partial \mathbf{b}_{\mathrm{con}}}{\partial \mathbf{b}_{\mathrm{co}}}\ , \\ \mathbf{r}_3 &:= \frac{1}{2}\ \Delta H\ \mathbf{a}_{\mathrm{co}}\ \mathbf{a}_{\mathrm{con}}^{\mathrm{T}} - \frac{1}{2}\ \mathbf{a}_{\mathrm{co}}\ \mathbf{b}_{\mathrm{con}}^{\mathrm{T}} + \Delta H\ \mathbf{I}_4\ , \\ \mathbf{r}_4 &:= \frac{1}{2}\ \mathbf{a}_{\mathrm{co}}\ \mathbf{a}_{\mathrm{con}}^{\mathrm{T}}\ , \end{aligned} \tag{A32}$$

where

$$\mathbf{c}_{\mathrm{con}} := \frac{1}{2}\ \left(\Delta H^2\ \mathbf{a}_{\mathrm{con}} - 2\ \Delta H\ \mathbf{b}_{\mathrm{con}}\right)\ , \quad \text{and} \quad \mathbf{d}_{\mathrm{con}} := \Delta H\ \mathbf{a}_{\mathrm{con}} - \mathbf{b}_{\mathrm{con}}. \tag{A33}$$

Here, the $(4 \times 4)$-identity matrix is denoted $\mathbf{I}_4$ and the derivatives $\partial \mathbf{a}_{\mathrm{con}} / \partial \mathbf{a}_{\mathrm{co}}$, $\partial \mathbf{b}_{\mathrm{con}} / \partial \mathbf{a}_{\mathrm{co}}$, and $\partial \mathbf{b}_{\mathrm{con}} / \partial \mathbf{b}_{\mathrm{co}}$ follow from Equation (A6) and they are arranged in analogy to Equation (A15).

## APPENDIX B. ANALYTICAL SOLUTIONS

### B.1 Inflated membrane balloon

This appendix derives the analytical solution for the inflated spherical membrane example from Section 5.2, see also Equations (103)–(105). The two contributions $p_{\mathrm{el}}(t)$ and $p_{\mathrm{visc}}(t)$ are derived subsequently.

#### B.1.1 Pressure from the elastic branch

The elastic behavior of rubber can be described by the incompressible Neo-Hookean material model from Equation (41). For the inflated balloon, the current radius $r$ is related to the initial radius $R$ via the stretch $\lambda$, that is, $r = \lambda\ R$. As $\mathrm{d}\boldsymbol{x} = \boldsymbol{F}\ \mathrm{d}\boldsymbol{X}$, the surface deformation gradient becomes $\boldsymbol{F} = \lambda\ \boldsymbol{i}$. The left surface Cauchy–Green tensor then becomes $\boldsymbol{B} = \boldsymbol{F}\boldsymbol{F}^{\mathrm{T}} = \lambda^2\ \boldsymbol{i}$. The surface stretch, which is related to the area change, that is, $\mathrm{d}a = J\ \mathrm{d}A$, is given by $J = \lambda^2$. Finally, the incompressibility of the material results in the relation $\tilde{t} = T/J$ between the current and initial thickness.

Using these kinematic relations, Equation (41), and the plane stress condition $\sigma_{33} = 0$, the stress tensor becomes

$$\tilde{\boldsymbol{\sigma}} = \frac{\boldsymbol{\sigma}}{\tilde{t}} + \sigma_{33}\ (\boldsymbol{n} \otimes \boldsymbol{n}) = \frac{1}{\tilde{t}}\ \frac{\mu}{J}\ \left(\boldsymbol{B} - \frac{\boldsymbol{i}}{J^2}\right) = \frac{1}{\tilde{t}}\ \frac{\mu}{\lambda^2}\ \left(\lambda^2\ \boldsymbol{i} - \frac{\boldsymbol{i}}{\lambda^4}\right) = \frac{\mu}{\tilde{t}}\ \left(1 - \frac{1}{\lambda^6}\right)\ \boldsymbol{i}. \tag{B1}$$

MOST WIEDZY Downloaded from mostwiedzy.pl

As derived in Needleman,[88] the in-plane normal stress in Equation (B1) is equal to $\tilde{\sigma} = p_{\text{el}}\, r/2/\tilde{t}$, which leads to the pressure-stretch or pressure-volume relation from Equation (104). The surface tension, see Equation (30.1), is then given by $\gamma = \mu\,(1-\lambda^{-6})$.

### B.1.2 Solution of the evolution laws

To determine the Maxwell stresses, the intermediate configuration needs to be fully specified. For this, the evolution laws

$$\dot{\hat{a}}^{\alpha\beta} + \frac{\mu_1}{\eta_{\text{s}}}\,\hat{a}^{\alpha\beta} = \frac{\mu_1}{\eta_{\text{s}}}\,a^{\alpha\beta}(t)\,, \quad \hat{a}^{\alpha\beta}(t=0) = A^{\alpha\beta}, \tag{B2}$$

need to be solved, see Equation (56). Based on the kinematic relations

$$\hat{a}_{\alpha\beta} = J_{\text{in}}\,A_{\alpha\beta}\,, \qquad \hat{a}^{\alpha\beta} = \frac{A^{\alpha\beta}}{J_{\text{in}}}\,, \qquad a_{\alpha\beta} = J\,A_{\alpha\beta}\,, \qquad a^{\alpha\beta} = \frac{A^{\alpha\beta}}{J}, \tag{B3}$$

the contravariant surface metric can be written as $a^{\alpha\beta} = A^{\alpha\beta}/\lambda^2$. Thus, Equation (B2) represent linear, inhomogeneous, first-order ODEs, which are solved with variation of constants. The solution is composed of an homogeneous ("hom") and particular ("p") part, that is,

$$\hat{a}^{\alpha\beta}(t) = \hat{a}^{\alpha\beta}_{\text{hom}}(t) + \hat{a}^{\alpha\beta}_{\text{p}}(t). \tag{B4}$$

The homogeneous part is given by

$$\hat{a}^{\alpha\beta}_{\text{hom}}(t) = c_0^{\alpha\beta}\,\exp\left(-\frac{\mu_1}{\eta_{\text{s}}}\,t\right)\,, \quad c_0^{\alpha\beta} = \text{const.} \tag{B5}$$

The particular part is now assumed to take the form $\hat{a}^{\alpha\beta}_{\text{p}}(t) = c^{\alpha\beta}(t)\;\exp(-\mu_1/\eta_{\text{s}}\,t)$, where $c^{\alpha\beta}(t)$ denotes an unknown function. Plugging this $\hat{a}^{\alpha\beta}_{\text{p}}$ into the ODEs in Equation (B2) and applying some algebraic manipulations yields

$$\dot{c}^{\alpha\beta}(t) = \frac{\mu_1}{\eta_{\text{s}}}\,a^{\alpha\beta}(t)\;\exp\left(\frac{\mu_1}{\eta_{\text{s}}}\,t\right), \tag{B6}$$

which resembles ODEs for the unknown $c^{\alpha\beta}(t)$. The solution is given by

$$c^{\alpha\beta}(t) = \int \frac{\mu_1}{\eta_{\text{s}}}\,a^{\alpha\beta}(\tilde{t})\;\exp\left(\frac{\mu_1}{\eta_{\text{s}}}\,\tilde{t}\right)\,\mathrm{d}\tilde{t} + c_1^{\alpha\beta}\,, \quad c_1^{\alpha\beta} = \text{const.} \tag{B7}$$

Plugging the homogeneous and particular solution into Equation (B4) then results in the solution

$$\hat{a}^{\alpha\beta}(t) = \exp\left(-\frac{\mu_1}{\eta_{\text{s}}}\,t\right)\left[c_2^{\alpha\beta} + \frac{\mu_1}{\eta_{\text{s}}}\int_0^t a^{\alpha\beta}(\tilde{t})\;\exp\left(\frac{\mu_1}{\eta_{\text{s}}}\,\tilde{t}\right)\right], \tag{B8}$$

where the constant $c_2^{\alpha\beta} = A^{\alpha\beta}$ follows from the initial condition in Equation (B2). The integral in Equation (B8) can then be explicitly computed using $a^{\alpha\beta} = A^{\alpha\beta}/\lambda^2$ with $\lambda(t)$ given in Equation (100). Defining $\hat{a}^{\alpha\beta}(t) := A^{\alpha\beta}\;\hat{a}_{\text{ev}}(t)$, with $\hat{a}_{\text{ev}}(t)$ given in Equation (106), the intermediate surface metric is given as the initial surface metric multiplied with an evolution function.

### B.1.3 Pressure from the Maxwell branch

For the Maxwell branch, the elastic energy density shown in Equation (36) with $\Lambda = 0$ is considered. The resulting stresses are given in Equation (37). Plugging the kinematic relations from Equation (B3) into the analytical solution for the contravariant surface metric in the intermediate configuration, $\hat{a}^{\alpha\beta}$, from Appendix B.1.2 yields

$$\frac{A^{\alpha\beta}}{J_{\text{in}}} = A^{\alpha\beta}\;\hat{a}_{\text{ev}}(t). \tag{B9}$$

MOST WIEDZY Downloaded from mostwiedzy.pl

Multiplying Equation (B9) with the surface stretch $J$, eliminating $A^{\alpha\beta}$, and using $J = J_{\text{el}}\, J_{\text{in}}$ results in the required relation for the elastic surface stretch, that is,

$$J_{\text{el}} = J\ \hat{a}_{\text{ev}}(t), \tag{B10}$$

with $\hat{a}_{\text{ev}}(t)$ given in Equation (106).

Based on the kinematic relations and the analytical solution for $\hat{a}^{\alpha\beta}$, the stresses in Equation (37) become

$$\sigma^{\alpha\beta}_{1(\text{el})} = \frac{\mu_1}{J\ \hat{a}_{\text{ev}}(t)}\ \left(A^{\alpha\beta}\ \hat{a}_{\text{ev}}(t) - a^{\alpha\beta}\right). \tag{B11}$$

In tensor notation, this becomes

$$\boldsymbol{\sigma}_{1(\text{el})} = \sigma^{\alpha\beta}_{1(\text{el})}\ \left(\boldsymbol{a}_\alpha \otimes \boldsymbol{a}_\beta\right) = \frac{\mu_1\ (\boldsymbol{B}\ \hat{a}_{\text{ev}}(t) - \boldsymbol{i})}{J\ \hat{a}_{\text{ev}}(t)} = \frac{\mu_1\ \left(\lambda^2\ \hat{a}_{\text{ev}}(t) - 1\right)}{\lambda^2\ \hat{a}_{\text{ev}}(t)}\ \boldsymbol{i} = \mu_1\ \left(1 - \frac{1}{\lambda^2\ \hat{a}_{\text{ev}}(t)}\right)\ \boldsymbol{i}, \tag{B12}$$

where the kinematic relations for $\boldsymbol{B}$ and $J$ have been inserted. Similar to Equation (B1), the in-plane normal stress is compared to $\tilde{\sigma} = p\ r/2/\tilde{t}$ to obtain the pressure-stretch relation, see Equation (105). The total pressure in the system is then given by the sum of Equations (104) and (105), see also Equation (103). The surface tension w.r.t. the intermediate configuration, see also Equation (30.1), is then given by $\hat{\gamma} = \mu_1\ (1 - \lambda^{-2}\ \hat{a}_{\text{ev}}^{-1})$.

### B.2 Pure bending of a flat strip

In this section, the analytical solution from Equations (110) to (112) is derived. The initially flat sheet of dimension $L \times S$ is deformed to a curved sheet with radius $r = 1/\kappa_2$. The boundary and loading conditions are chosen such that the surface stretches are equal to one, that is, $\lambda_1 = \lambda_2 = 1$. The derivation follows the elastic case considered in Sauer and Duong.[79] The surface is parametrized by the coordinates $\xi \in [0, L]$ and $\eta \in [0, S]$, that is, $\xi$ points along the $x$-direction in Figure 17 and $\eta$ points along the $y$-direction. The reference and current surface can be described via the mappings

$$\boldsymbol{X}(\xi, \eta) = \xi\ \boldsymbol{e}_1 + \eta\ \boldsymbol{e}_2, \tag{B13}$$

and

$$\boldsymbol{x}(\xi, \eta) = \xi\ \boldsymbol{e}_1 + r\ \sin\theta\ \boldsymbol{e}_2 + r\ (1 - \cos\theta)\ \boldsymbol{e}_3, \tag{B14}$$

with $\theta := \kappa_2\ \eta$. Based on these mappings, the tangent vectors follow as $\boldsymbol{A}_1 = \boldsymbol{e}_1$, $\boldsymbol{A}_2 = \boldsymbol{e}_2$, $\boldsymbol{a}_1 = \boldsymbol{e}_1$, and $\boldsymbol{a}_2 = \cos\theta\ \boldsymbol{e}_2 + \sin\theta\ \boldsymbol{e}_2$, and the surface normal follows as $\boldsymbol{n} = -\sin\theta\ \boldsymbol{e}_2 + \cos\theta\ \boldsymbol{e}_3$. The surface metrics are then given by

$$\left[A_{\alpha\beta}\right] = \left[A^{\alpha\beta}\right] = \left[a_{\alpha\beta}\right] = \left[a^{\alpha\beta}\right] = \begin{bmatrix} 1 & 0 \\ 0 & 1 \end{bmatrix}, \tag{B15}$$

such that the surface stretch is $J = 1$ by construction. The curvature tensor components are given by

$$\left[b_{\alpha\beta}\right] = \left[b^{\alpha}_{\beta}\right] = \left[b^{\alpha\beta}\right] = \begin{bmatrix} 0 & 0 \\ 0 & \kappa_2 \end{bmatrix}, \tag{B16}$$

such that the mean and Gaussian curvature follow as $H = \kappa_2/2$ and $\kappa = 0$, respectively. Similar to Equations (B15) and (B16), the intermediate surface metric and curvature tensor components are

$$\left[\hat{a}_{\alpha\beta}\right] = \left[\hat{a}^{\alpha\beta}\right] = \begin{bmatrix} 1 & 0 \\ 0 & 1 \end{bmatrix}, \quad \text{and} \quad \left[\hat{b}_{\alpha\beta}\right] = \left[\hat{b}^{\alpha\beta}\right] = \begin{bmatrix} 0 & 0 \\ 0 & \kappa_2^{\text{in}} \end{bmatrix}, \tag{B17}$$

with inelastic curvature $\kappa_2^{\text{in}}$. The intermediate mean curvature follows from $\hat{H} = \kappa_2^{\text{in}}/2$. Further, $J_{\text{in}} = J_{\text{el}} = 1$.

MOST WIEDZY Downloaded from mostwiedzy.pl

Based on the Neo-Hookean and Koiter bending material models for the elastic and Maxwell branch, see Equations (36) and (44), the stresses are given by $\sigma^{11} = \sigma^{12} = \sigma^{21} = \sigma^{22} = 0$, as $\lambda_1 = \lambda_2 = \lambda_1^{\text{el}} = \lambda_2^{\text{el}} = 1$. The moment components are $M^{11} = M^{12} = M^{21} = 0$ and

$$M^{22} = c\ \kappa_2 + c_1\ \left(\kappa_2 - \kappa_2^{\text{in}}\right). \tag{B18}$$

The resulting in-plane stress components $N^{\alpha\beta} = \sigma^{\alpha\beta} + b_\gamma^\alpha\ M^{\gamma\beta}$ follow as

$$N^{11} = N^{12} = N^{21} = 0\ , \quad \text{and} \quad N^{22} = c\ \kappa_2^2 + c_1\ \left(\kappa_2^2 - \kappa_2\ \kappa_2^{\text{in}}\right). \tag{B19}$$

As $[a_{\alpha\beta}]$ is equal to the identity matrix, see Equation (B15), it follows that $[N_\beta^\alpha] = [N^{\alpha\beta}]$. Considering a cut at $\theta$, which is perpendicular to the normal $\boldsymbol{\nu} = \boldsymbol{a}_2$, the distributed bending moment on this cut can be computed as

$$M = M^{\alpha\beta}\ \nu_\alpha\ \nu_\beta = c\ \kappa_2 + c_1\ \left(\kappa_2 - \kappa_2^{\text{in}}\right), \tag{B20}$$

such that the curvature $\kappa_2(t)$ follows as given in Equation (112).

Still, the inelastic curvature $\kappa_2^{\text{in}}(t)$ is unknown. Using Equations (62), (112), and (B17), the ODE for $\kappa_2^{\text{in}}$ is given by

$$\dot{\kappa}_2^{\text{in}} = \frac{c_1}{\eta_{\text{b}}\ (c + c_1)}\ \left(M - c\ \kappa_2^{\text{in}}\right), \tag{B21}$$

with initial condition $\kappa_2^{\text{in}}(t = 0) = 0$. Using the definition from Equation (111), the ODE is rewritten in the form

$$\dot{\kappa}_2^{\text{in}} + \frac{1}{\tau_b}\ \kappa_2^{\text{in}} = \frac{1}{c\ \tau_b}\ M(t). \tag{B22}$$

In analogy to Appendix B.1.2, this ODE can be solved based on the variation of parameters. The solution reads

$$\kappa_2^{\text{in}}(t) = \frac{1}{c\ \tau_b}\ e^{-t/\tau_b} \int_0^t M(\tilde{t})\ e^{\tilde{t}/\tau_b}\ \mathrm{d}\tilde{t}. \tag{B23}$$

Using the moment profile $M(t)$ from Equation (108), the integral in Equation (B23) can be analytically solved such that $\kappa_2^{\text{in}}(t)$ is obtained as given in Equation (110).

### B.3 Inflated spherical shell

This section derives the analytical solution for the inflated spherical shell example from Section 5.4, see also Equations (116)–(118). The derivation of the elastic pressure, $p_{\text{el}}(t)$, can be found in Sauer et al.,[27] but it is repeated here for completeness.

#### B.3.1 Pressure from the elastic branch

Given the material models from Equations (41) and (46), the in-plane traction components are given by

$$N_{\text{el}}^{\alpha\beta} = N_a^{\text{el}}\ a^{\alpha\beta} + N_b^{\text{el}}\ b^{\alpha\beta}, \tag{B24}$$

with

$$N_a^{\text{el}} := \mu\ \left(1 - \frac{1}{J^3}\right) + k\ (H - H_0)^2\ , \quad \text{and} \quad N_b^{\text{el}} := -k\ (H - H_0). \tag{B25}$$

Based on the surface parametrization

$$\boldsymbol{x}(\varphi, \theta) = \begin{bmatrix} r\ \cos\varphi\ \sin\theta \\ r\ \sin\varphi\ \sin\theta \\ -\,r\ \cos\theta \end{bmatrix}, \tag{B26}$$

MOST WIEDZY Downloaded from mostwiedzy.pl

the following relations can be found

$$\left[a^{\alpha\beta}\right] = \frac{1}{r^2}\begin{bmatrix} 1/\sin^2\theta & 0 \\ 0 & 1 \end{bmatrix}, \quad b^{\alpha\beta} = -a^{\alpha\beta}/r\,, \quad \text{and} \quad H = -\frac{1}{r}. \tag{B27}$$

The traction vector $\boldsymbol{T} = \boldsymbol{T}^{\alpha}\ \nu_{\alpha}$ on a cut orthogonal to $\boldsymbol{\nu}$ then becomes

$$\boldsymbol{T} = \left(N_{\text{el}}^{\alpha\beta}\ \boldsymbol{a}_{\beta} + S^{\alpha}\ \boldsymbol{n}\right)\ \nu_{\alpha} = \left[N_a^{\text{el}} - \frac{N_b^{\text{el}}}{r}\right]\ \boldsymbol{\nu}, \tag{B28}$$

where the kinematic relations from Equation (B27) have been used. Similar to Appendix B.1, the in-plane component $T_{\nu} := N_a^{\text{el}} - N_b^{\text{el}}/r$ needs to equilibrate the current pressure according to[88]

$$p_{\text{el}} = \frac{2\ T_{\nu}}{r} = \frac{2}{r}\ \left[N_a^{\text{el}} - \frac{N_b^{\text{el}}}{r}\right]. \tag{B29}$$

Plugging Equation (B25) into Equation (B29) and using the kinematic relations $J = \lambda^2$, $r = \lambda\ R$ and $H = -1/r$ yields the elastic pressure given in Equation (117).

### B.3.2 Solution of the evolution laws

To determine the Maxwell moments, the intermediate configuration needs to be fully specified. The intermediate surface metric is the same as derived in Appendix B.1.2, that is, $\hat{a}^{\alpha\beta}(t) = A^{\alpha\beta}\ \hat{a}_{\text{ev}}(t)$ and $J_{\text{el}}(t) = J(t)\ \hat{a}_{\text{ev}}(t)$ with $\hat{a}_{\text{ev}}(t)$ given in Equation (106). The bending of the intermediate surface follows from the solution of the evolution laws

$$\dot{\hat{b}}_{\alpha\beta} + \frac{c_1}{\eta_{\text{b}}}\ \hat{b}_{\alpha\beta} = \frac{c_1}{\eta_{\text{b}}}\ b_{\alpha\beta}(t)\,, \quad \hat{b}_{\alpha\beta}(t=0) = B_{\alpha\beta}, \tag{B30}$$

see Equation (62). Based on the surface parametrization in Equation (B26), the relation $b_{\alpha\beta}(t) = \lambda(t)\ B_{\alpha\beta}$ can be derived. As Equation (B30) resembles first-order, linear, inhomogeneous ODEs, the same approach as in Appendix B.1.2 can be used in order to solve for $\hat{b}_{\alpha\beta}$. The solution is then given by

$$\hat{b}_{\alpha\beta}(t) = B_{\alpha\beta}\ \hat{b}_{\text{ev}}(t), \tag{B31}$$

with $\hat{b}_{\text{ev}}(t)$ given in Equation (119). Note that the function $\lambda(t)$ from Equation (100) has been inserted to obtain a closed-form solution for $\hat{b}_{\text{ev}}(t)$.

### B.3.3 Pressure from the Maxwell branch

Given the material models in Equations (36) and (44) with $\Lambda = 0$, the Maxwell stresses and moments follow as

$$\sigma_{1(\text{el})}^{\alpha\beta} = \frac{\mu_1}{J_{\text{el}}}\ \left(\hat{a}^{\alpha\beta} - a^{\alpha\beta}\right)\,, \quad \text{and} \quad M_{1(\text{el})}^{\alpha\beta} = \frac{1}{J_{\text{el}}}\ \hat{f}^{\alpha\beta\gamma\delta}\ \kappa_{\gamma\delta}^{\text{el}}. \tag{B32}$$

Using the kinematic relations from Equation (B3), $b_{\alpha\beta} = \lambda\ B_{\alpha\beta}$ and $B^{\alpha\beta} = \lambda^3\ b^{\alpha\beta}$ yields

$$\sigma_{1(\text{el})}^{\alpha\beta} = \mu_1\ \left(1 - \frac{1}{J_{\text{el}}}\right)\ a^{\alpha\beta}\,, \quad \text{and} \quad M_{1(\text{el})}^{\alpha\beta} = c_1\ \hat{a}_{\text{ev}}\ \left(\lambda^2 - \lambda\ \hat{b}_{\text{ev}}\right)\ b^{\alpha\beta}, \tag{B33}$$

with $\hat{a}_{\text{ev}}(t)$ given in Equation (106) and $\hat{b}_{\text{ev}}(t)$ given in Equation (119). Similar to Equation (B24), the in-plane traction components for the Maxwell branch are given by

$$N_{\text{visc}}^{\alpha\beta} = N_a^{\text{visc}}\ a^{\alpha\beta} + N_b^{\text{visc}}\ b^{\alpha\beta}, \tag{B34}$$

MOST WIEDZY Downloaded from mostwiedzy.pl

where

$$N_a^{\text{visc}} := \mu_1 \left(1 - \frac{1}{\lambda^2\, \hat{a}_{\text{ev}}}\right), \quad \text{and} \quad N_b^{\text{visc}} := \frac{c_1}{R}\, \hat{a}_{\text{ev}} \left(\hat{b}_{\text{ev}} - \lambda\right). \tag{B35}$$

Using Equation (B29) and replacing the elastic traction components with the viscous traction components from Equation (B35) yields the pressure $p_{\text{visc}}(t)$ as given in Equation (118).

MOST WIEDZY Downloaded from mostwiedzy.pl